

**PROCESS INTENSIFICATION TECHNIQUES FOR CONTINUOUS
SPHERICAL CRYSTALLIZATION IN AN OSCILLATORY BAFFLED
CRYSTALLIZER WITH ONLINE PROCESS MONITORING**

by

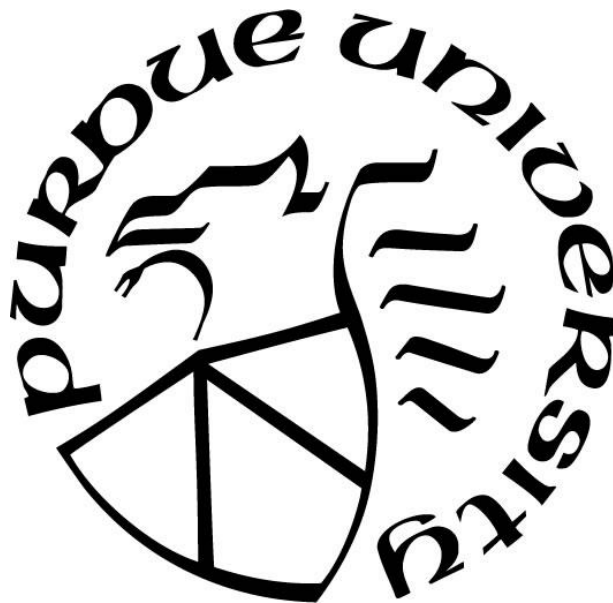
Joseph A. Oliva

A Thesis

Submitted to the Faculty of Purdue University

In Partial Fulfillment of the Requirements for the degree of

Doctor of Philosophy



Davidson School of Chemical Engineering
West Lafayette, Indiana

May 2019

THE PURDUE UNIVERSITY GRADUATE SCHOOL
STATEMENT OF COMMITTEE APPROVAL

Dr. Zoltan K. Nagy

Davidson School of Chemical Engineering

Dr. Gintaras V. Reklaitis

Davidson School of Chemical Engineering

Dr. Michael Harris

Davidson School of Chemical Engineering

Dr. David H. Thompson

Department of Chemistry

Approved by:

Dr. Sangtae Kim

Head of the Graduate Program

ACKNOWLEDGMENTS

First off, I want to thank my outstanding advisor, Zoltan K. Nagy for his role in my professional development. As my academic role model, he fostered innovative, practical research by creating a positive work environment. His passionate support for students truly inspired me to play an active role in our research group and department. Next, I want to thank my undergraduate research advisor, Jennifer Sinclair Curtis. As an undergraduate student at the University of Florida, she took a special interest in mentoring me. Even as an Associate Dean in the College of Engineering, she met with me each week, listening to each of the challenges I faced. When my tenure in Florida came to a close, she guided me to Purdue Engineering, inspiring me to pursue a career in research, always believing I would succeed.

Next, I would like to thank my friends and group members, who supported me through the most challenging times of this process. Ryan and Claire, from our first year in the basement “dungeon”, we stuck together as a tight friend group, always looking out for each other. Together, we expanded our small friend group into a large group of truly amazing people. Peter, Heather, Amy, Vinny, Steven, and Alex, you guys really became my family here at Purdue. From countless Colorado trips, to watching soccer on Saturday mornings with breakfast burritos, you guys helped me find balance and made my PhD experience enjoyable. When I first joined the Nagy research group, Ramon, David and Andy, you guys took me, Pal and Claire under your wing and helped us find our place at Purdue. I can only hope to have been as good of a role model to our newest group members (Ayşe, Jaron, and Wei-Lee), who will certainly extend the excellent work you started. Boti, Emó, and Ayşe, you guys became the core foundation of our group. From organizing BBQs to weekly visits to People’s Brewing, you hold our group together and always have a willingness to help.

Lastly, I would like to give a special thanks to my family. Mom, Dad, Larry, Linda, and Grandma Shirley, you guys have been with me from the start, always supporting my decision to pursue a higher education. From helping me move, to listening to daily problems, your support has enabled me to pursue my dreams of making a difference in pharmaceutical development. I plan to continue this pursuit in modern medicine, knowing I have your support and I cannot thank you enough.

TABLE OF CONTENTS

| | |
|--|-----------|
| LIST OF TABLES | viii |
| LIST OF FIGURES | ix |
| ABSTRACT | xiii |
| 1. INTRODUCTION | 1 |
| 1.1 Motivation for Continuous Manufacturing | 1 |
| 1.2 Motivation for Process Intensification | 2 |
| 1.3 Overview of Research Objectives | 3 |
| 1.4 References | 6 |
| 2. LITERATURE REVIEW AND CASE STUDIES | 7 |
| 2.1 Overview of Crystallization | 7 |
| 2.2 Phase Diagrams and Polymorphic Forms | 9 |
| 2.3 Crystallization Mechanisms | 13 |
| 2.3.1 Nucleation | 14 |
| 2.3.2 Growth | 16 |
| 2.3.3 Agglomeration, Breakage, and Coalescence | 16 |
| 2.4 Batch Crystallization | 17 |
| 2.4.1 Batch Crystallization Case Study | 18 |
| 2.5 Continuous Crystallization Systems | 24 |
| 2.6 Heat Transfer Coefficient Case Study | 26 |
| 2.7 Overview of Spherical Crystallization | 29 |
| 2.8 Process Analytical Technology Tools and Their Role in Spherical Agglomeration | 30 |
| 2.9 Dimensionless Operating Parameters | 32 |
| 2.10 Geometric Considerations in Oscillatory Baffled Systems | 33 |
| 2.11 References | 35 |
| 3. EXPERIMENTAL INVESTIGATION OF THE EFFECT OF SCALE-UP ON MIXING EFFICIENCY IN OSCILLATORY FLOW BAFFLED REACTORS (OFBR) USING PRINCIPAL COMPONENT-BASED IMAGE ANALYSIS AS A NOVEL NONINVASIVE RESIDENCE TIME DISTRIBUTION MEASUREMENT APPROACH | 44 |
| 3.1 Abstract | 44 |

| | | |
|-------|---|----|
| 3.2 | Introduction..... | 45 |
| 3.2.1 | Residence Time Distributions in Oscillatory Baffled Systems | 48 |
| 3.2.2 | Mean Residence Time and Dispersion Calculations | 49 |
| 3.2.3 | Principal Component Image Analysis (PCA)..... | 51 |
| 3.3 | Materials and Methods..... | 52 |
| 3.3.1 | Residence Time Distribution Studies | 52 |
| 3.3.2 | Principal Component Image Analysis | 54 |
| 3.3.3 | Limits of Detection using PCA and Methylene Blue | 55 |
| 3.4 | Results and Discussion | 56 |
| 3.4.1 | Summary of Experimental Conditions | 56 |
| 3.4.2 | Changes in Amplitude | 57 |
| 3.4.3 | Changes in Frequency..... | 59 |
| 3.5 | System Sensitivity to Flow Type | 61 |
| 3.6 | Conclusions..... | 64 |
| 3.7 | References..... | 66 |
| 4. | PROCESS INTENSIFICATION THROUGH CONTINUOUS SPHERICAL CRYSTALLIZATION USING AN OSCILLATORY BAFFLED CRYSTALLIZER (OBC).... | 69 |
| 4.1 | Abstract..... | 69 |
| 4.2 | Introduction..... | 70 |
| 4.3 | Materials and Method | 74 |
| 4.3.1 | Lab Reagents | 74 |
| 4.3.2 | Experimental Setup..... | 74 |
| 4.3.3 | UPLC Method for Benzoic Acid Quantification..... | 76 |
| 4.3.4 | Benzoic Acid Solubility Determination..... | 77 |
| 4.3.5 | Experimental Procedure..... | 78 |
| 4.4 | Results and Discussion | 80 |
| 4.4.1 | Evaluation of Mixing Conditions | 81 |
| 4.4.2 | Initial supersaturation variations via SASR..... | 83 |
| 4.4.3 | Initial supersaturation variations via benzoic acid concentration..... | 84 |
| 4.5 | Changes in BSR | 85 |
| 4.5.1 | Set point changes in BSR | 86 |

| | | |
|-------|--|-----|
| 4.6 | Evaluation of Different Agglomeration Zone Lengths | 89 |
| 4.7 | Summary of Results | 92 |
| 4.8 | Conclusions | 93 |
| 4.9 | References | 96 |
| 5. | CONTINUOUS SPHERICAL CRYSTALLIZATION OF LYSOZYME IN AN OSCILLATORY BAFFLED CRYSTALLIZER USING EMULSION SOLVENT DIFFUSION IN DROPLETS | 101 |
| 5.1 | Abstract | 101 |
| 5.2 | Introduction | 102 |
| 5.3 | Materials and Methods | 106 |
| 5.3.1 | Solvent Selection and Screening Rationale | 106 |
| 5.3.2 | Materials and Methods for COBC Operation | 107 |
| 5.3.3 | Spherical Crystallization's Impact on Protein Activity | 109 |
| 5.3.4 | Size Analysis | 110 |
| 5.3.5 | Determining the Effect of Droplet Size on Crystal Size Distribution | 115 |
| 5.3.6 | Scaleup Between the DN6 and DN15 Systems | 116 |
| 5.4 | Results and Discussion | 117 |
| 5.4.1 | Steady State Operation | 117 |
| 5.4.2 | Non-Steady State Operation | 118 |
| 5.4.3 | Blaze Microscopy vs Scanning Electron Microscopy (SEM) | 120 |
| 5.4.4 | Ethanol Concentration in the Bulk Phase | 121 |
| 5.4.5 | Concentration of Lysozyme in Droplets | 122 |
| 5.4.6 | Piston-Driven Suspension Energy | 124 |
| 5.4.7 | Lysozyme Injection Rate | 126 |
| 5.4.8 | Effect of Nozzle Tip Size on CSD | 127 |
| 5.4.9 | Scale-Up and Geometric Considerations | 129 |
| 5.5 | Conclusions | 130 |
| 5.6 | References | 132 |
| 6. | COMPARTMENTAL MODELING OF CONTINUOUS OSCILLATORY BAFFLED CRYSTALLIZER (COBC) SYSTEMS AND THE EFFECT OF SCALE UP ON HYDRODYNAMICS | 136 |

| | | |
|-------|---|-----|
| 6.1 | Abstract..... | 136 |
| 6.2 | Introduction..... | 137 |
| 6.3 | Experimental Materials and Methods..... | 140 |
| 6.3.1 | Principal Component Image Analysis (PCA)..... | 141 |
| 6.3.2 | Flowrate analysis of the DN6 and DN15 COBC system..... | 142 |
| 6.3.3 | Piston dynamics and analysis: oscillation damping effects..... | 144 |
| 6.3.4 | Pump dynamics analysis..... | 145 |
| 6.3.5 | Flow-field generated by the combined action of piston and pump..... | 146 |
| 6.3.6 | Approximation of flowrate profile in DN15 COBC system..... | 147 |
| 6.4 | CM development, calibration and results..... | 149 |
| 6.4.1 | DN6 and DN15 results with new compartment numbers with realistic pump flow rates..... | 151 |
| 6.5 | CM generalization for the DN6 and DN15 systems..... | 154 |
| 6.5.1 | Correlation estimation using different expressions..... | 155 |
| 6.5.2 | Model validation using new measurements..... | 158 |
| 6.6 | Conclusions..... | 160 |
| 6.7 | References..... | 161 |
| 6.8 | List of Appendices..... | 164 |

LIST OF TABLES

| | |
|--|-----|
| Table 3-1 Optimum operating parameters of OFBRs in literature | 48 |
| Table 3-2 DN6 (top) and DN15 (bottom) RTD experiments and dispersion calculation results . | 56 |
| Table 4-1 Summary of the experimental conditions..... | 81 |
| Table 4-2 Summary of experimental results | 93 |
| Table 5-1 Solvent candidates in which lysozyme has poor solubility | 106 |
| Table 5-2 Summary of Experimental Conditions.. | 117 |
| Table 6-1 Oscillation damping in the DN6 system..... | 145 |
| Table 6-2 Measured DN6 oscillations and approximation of the DN15 flowrate oscillation behavior..... | 148 |
| Table 6-3 The comparison of measured and simulated dispersion coefficients for the DN6 and DN15 system in the calibration runs..... | 151 |
| Table 6-4 Model validation results | 158 |
| Table 6-5 Comparison of measured piston oscillation data with the setpoint. | 165 |
| Table 6-6 Frequency analysis of the pump flowrate..... | 165 |
| Table 6-7 Frequency analysis of RTD measurement conditions in the DN6 system | 166 |

LIST OF FIGURES

| | |
|---|----|
| Figure 1.1 Hierarchical thesis diagram | 5 |
| Figure 2.1 Phase diagram for Aspirin in acetonitrile | 10 |
| Figure 2.2 Gibb’s free energy diagram showing the stability of polymorphs | 10 |
| Figure 2.3 Monotropic vs enantiotropic polymorphic systems | 12 |
| Figure 2.4 Cooling profiles for natural and slow linear cooling rates | 19 |
| Figure 2.5 Operating curves for each experiment within the phase diagram. | 20 |
| Figure 2.6 (top) Change in counts as the system temperature changes over time. (bottom) change in SWMCL as crystal counts change over time..... | 21 |
| Figure 2.7 PVM imaging from cooling crystallization case study | 23 |
| Figure 2.8 (top) Mixing mechanism in an OBC and (bottom) schematic of a typical vertical OBC. Adapted from Ni et al.28,30 | 25 |
| Figure 2.9 (top) the effect of piston amplitude on heat transfer coefficient and (bottom) the effect of piston frequency on heat transfer coefficient | 28 |
| Figure 2.10 Illustration of COBC geometry with dimensions. Adapted from McDonough | 33 |
| Figure 3.1 Illustration of OFBC geometry, adapted from McDonough | 46 |
| Figure 3.2 Illustration of asymmetry factor calculation..... | 50 |
| Figure 3.3 Pictures with main components of the DN6 (top) and DN15 (bottom) RTD experimental setup | 54 |
| Figure 3.4 (top) Measured dispersion coefficients over a range of piston amplitudes (middle) RTDs in the DN6 (bottom) RTDs in the DN15..... | 58 |
| Figure 3.5 (top) Measured dispersion coefficients over a range of piston frequencies (middle) RTDs in the DN6 (bottom) RTDs in the DN15..... | 60 |
| Figure 3.6 Measured dispersion coefficients at different pump flow rates..... | 61 |
| Figure 3.7 Measured dispersion as the fluid flows through a set number of baffles per second.. | 62 |
| Figure 3.8 Measured dispersion while operating in either piston or pump dominated flow | 63 |
| Figure 4.1 Schematic of the fluid flow pattern in an OFBR/C with net flow to the right: a) forward stroke b) backward stroke. Adapted from Ni et al. | 72 |
| Figure 4.2 OFBC configuration indicating location of anti-solvent, solution and binder addition as well as PAT port (FBRM) | 76 |
| Figure 4.3 UPLC generated solubility of benzoic acid in ethanol solution-water mixtures of different ratios..... | 78 |

| | |
|--|-----|
| Figure 4.4 Concentration of benzoic acid as a function of time measured at the outlet of the OFBC..... | 80 |
| Figure 4.5 (top) Size distributions for different oscillatory mixing intensities and (bottom) agglomerates from experiments with increasing mixing intensity from left to right (exp. 2-4).. | 82 |
| Figure 4.6 (top) Agglomerate size distributions for different SASR ratios and (bottom) agglomerates from experiments with decreasing SASR from left to right..... | 84 |
| Figure 4.7 Agglomerate size distributions for different solution concentrations of benzoic acid | 85 |
| Figure 4.8 Agglomerate size distributions for different BSR..... | 86 |
| Figure 4.9 Total counts and square weighted mean chord length (SWMCL) from FBRM probe | 87 |
| Figure 4.10 Images of the primary crystals prior to agglomeration..... | 88 |
| Figure 4.11 (top) Agglomeration size distributions for step changes in BSR and images of agglomerates at different residence times. (bottom from left to right) BSR = 0.8, BSR = 1.0, BSR = 0.85 and BSR = 0.8..... | 89 |
| Figure 4.12 (top) Agglomerate size distributions for different agglomeration zone configurations and (bottom from left to right) images of agglomerates from experiments 4, 8 and 9..... | 91 |
| Figure 5.1 Schematic of the droplet injection site, showing the primary mechanism for generating supersaturation at the droplet interface..... | 107 |
| Figure 5.2 Overview of the experimental setup..... | 108 |
| Figure 5.3 Lysozyme activity calibration and result before and after the spherical crystallization process..... | 109 |
| Figure 5.4 Transformation of a number-based CSD to a volume-based CSD and the qualitative effect of the reporting method..... | 111 |
| Figure 5.5 Comparison of statistical approaches used to determine appropriate bin widths for CSD reporting..... | 113 |
| Figure 5.6 Comparison of statistical approaches used to determine appropriate bin widths that increase logarithmically..... | 114 |
| Figure 5.7 Determining steady state product generation in the DN6 (left) and DN15 (right). The data shown corresponds to Exp 1 and 12 respectively. | 117 |
| Figure 5.8 Consequences of encrust formation on process steady state as measured by CSDs over time (top) and microscope images (bottom). Note: the bottom left image is from RT2 and the bottom right image is from RT3. The data shown corresponds to Exp 6. | 119 |
| Figure 5.9 Comparison of in-situ Blaze Microscopy (left) vs. offline SEM (right) in characterizing the spherical lysozyme product..... | 120 |
| Figure 5.10 The effect of varying ethanol concentration on crystal size. The data corresponds to Exp 2, 3, 1, and 4 respectively. | 121 |

| | |
|--|-----|
| Figure 5.11 The effect of changing the concentration of lysozyme in the droplet phase. Note: 0.5x corresponds to 15.4 mg/mL, 1x corresponds to 30.7 mg/mL, and 1.5x corresponds to 46.1 mg/mL. The data corresponds to Exp 9, 1 and 10 respectively | 122 |
| Figure 5.12 The impact of varying piston driven suspension energy on the CSD. The data corresponds to Exp 5, 6, and 1 respectively (top) while the pictures correspond to Exp 5 and 6 (bottom)..... | 124 |
| Figure 5.13 Variable lysozyme droplet injection rates and their effect on the product's CSD. The data corresponds to Exp 8, 1, and 7 respectively (top) while the pictures correspond to Exp 8 and 7 (bottom)..... | 126 |
| Figure 5.14 The effect of varying the injection nozzle tip size on the product's CSD. The data and pictures correspond to Exp 13, 11, and 14 respectively. | 127 |
| Figure 5.15 Two different approaches for scaling the production of lysozyme. The data corresponds to Exp 1, 11, and 12 respectively, while the pictures correspond to Exp 11 and 12 (bottom)..... | 129 |
| Figure 6.1 Experimental setup for pulse tracer experiments in the oscillatory baffled reactor .. | 140 |
| Figure 6.2 Sensor placements in the DN6 system. The flowrate sensor is the black box in Configuration 2. | 143 |
| Figure 6.3 (left) temporal evolution of the flowrate generated by the superposition of pump and piston operations with 15 mL/min pump flowrate, 10 mm piston amplitude and 1 Hz piston frequency as measured in Configuration 3 and (right) the corresponding frequency..... | 143 |
| Figure 6.4 Flowrate profiles generated by the combined action of piston and pump at 15 mL/min flowrate, as measured in Configuration 2. (left) effective piston and pump oscillation amplitudes and (right) effective piston oscillation amplitude. | 146 |
| Figure 6.5 Typical response functions to indicator impulses the thin lines between belongs to the cascade CSTR model. Note: the higher the number of cascade element, the better the approximation of a PFR. | 149 |
| Figure 6.6 The new results without normalization for DN6 (top) experimental and (bottom) simulated..... | 152 |
| Figure 6.7 The new results without normalization for DN15 (top) experimental and (bottom) simulated..... | 153 |
| Figure 6.8 Correlation plot for the COBC systems (left) number of cascade CSTR elements for DN6 (right) number of cascade CSTR elements for DN15 | 155 |
| Figure 6.9 Correlation plot based on theoretical amplitudes and frequencies for (top-left) DN6 (top-right) DN15 (bottom) DN6-DN15 combined | 156 |
| Figure 6.10 Correlation plot based on realistic amplitudes and frequencies for (top-left) DN6 (top-right) DN15 (bottom) DN6-DN15 combined | 157 |
| Figure 6.11 Model validation using (top) Eqn 8 (bottom) Eqn 11 | 159 |

Figure 6.12 Frequency diagram of Experiments 1-4. The pump amplitude peak is abnormally wide in the case of $A = 5$ mm, which suggests that in this case the determination of effective pump oscillation amplitude is not accurate..... 167

ABSTRACT

Author: Oliva, Joseph A. PhD

Institution: Purdue University

Degree Received: May 2019

Title: Process Intensification Techniques for Continuous Spherical Crystallization in an Oscillatory Baffled Crystallizer with Online Process Monitoring

Committee Chair: Zoltan K. Nagy

Guided by the continuous manufacturing paradigm shift in the pharmaceutical industry, the proposed thesis focuses on the implementation of an integrated continuous crystallization platform, the oscillatory baffled crystallizer (OBC), with real time process monitoring. First, by defining an appropriate operating regime with residence time distribution (RTD) measurements, a system can be defined that allows for plug flow operation while also maintaining solid suspension in a two-phase system. The aim of modern crystallization processes, narrow crystal size distributions (CSDs), is a direct result of narrow RTDs. Using a USB microscope camera and principal component analysis (PCA) in pulse tracer experiments, a novel non-contact RTD measurement method was developed using methylene blue. After defining an operating region, this work focuses on a specific process intensification technique, namely spherical crystallization.

Used mainly to tailor the size of a final dosage form, spherical crystallization removes the need for downstream size-control based unit operations (grinding, milling, and granulation), while maintaining drug efficacy by tailoring the size of the primary crystals in the agglomerate. The approach for generating spherical agglomerates is evaluated for both small and large molecules, as there are major distinctions in process kinetics and mechanisms. To monitor the spherical agglomeration process, a variety of Process Analytical Technology (PAT) tools were used and the data was implemented for scale-up applications.

Lastly, a compartmental model was designed based on the experimental RTD data with the intention of predicting OBC mixing and scale-up dynamics. Together, with validation from both the DN6 and DN15 systems, a scale independent equation was developed to predict system dispersion at different mixing conditions. Although it accurately predicts the behavior of these two OBC systems, additional OBC systems of different scale, but similar geometry should be tested for validation purposes.

1. INTRODUCTION

1.1 Motivation for Continuous Manufacturing

From upstream molecular synthesis to downstream blending applications, traditional pharmaceutical manufacturing is a series of batch processes that lack real time process monitoring and control. However, with significant improvements in continuous flow chemistry and reaction screening, the bottleneck for a fully integrated, continuous manufacturing line is crystallization. Crystallization is the industry standard for molecular purification and approximately 90% of all (small molecule) pharmaceutical processes include at least one crystallization step.

Continuous manufacturing was once ignored by pharmaceutical manufacturers because manufacturing costs were seen as a small portion of the overall costs associated with bringing a molecule to market. From a research and development point of view, only one in 10,000 potential candidates makes it from lab bench to market. Moreover, the average cost of bringing a single molecule to market was estimated to be \$1.3B in 2007. As competition from generics continues to put pressure on primary manufacturers to produce new drug products, the bottom line manufacturing costs of existing drugs is becoming ever more significant.

In addition to improving the processing efficiency of existing drug products, continuous manufacturing offers significant improvements in terms of product variation. Non-idealities in batch processes like poor micromixing and heat transfer often lead to batch-to-batch variation in product quality. Measuring product specifications is currently done by taking samples and performing offline analysis. If the product does not pass narrow windowed specifications, the entire batch must be discarded per Food and Drug Administration (FDA) regulations. The estimated cost of a batch is roughly between \$3M and \$5M, making this outcome a costly

endeavor. Unlike its batch counterpart, continuous manufacturing lines have the luxury of operating at a steady state. With real time product measurements using Process Analytical Technology (PAT) tools, off-spec product can be detected and adjusted back into the specification range prior to being sent to the next unit operation in the manufacturing line. As a result, significant reductions in discarded product are motivating the need for continuous production capabilities.

1.2 Motivation for Process Intensification

Process intensification is the utilization of new techniques that significantly improve manufacturing processes, resulting in cheaper and greener technologies^[1]. Comprised of two parts, novel equipment (such as microscale reactors^[2]) and novel processing techniques (such as model-based control approaches^{[3]-[5]}), process intensification is enabling the pharmaceutical industry to move towards continuous manufacturing^[10] by incentivizing initial financial barriers. Continuous manufacturing offers large scale production capabilities while also creating a safer working environment for operators, decreasing variations in product quality, and reducing waste.

In a pharmaceutical manufacturing line, the subsequent steps following crystallization involve size manipulation processes like milling and granulation because the size of the API directly impacts tablet uniformity. During tablet production, the blended API product typically flows over a series of gaps before being pressed into tablets, meaning the flowability of the powder directly impacts the amount of API in each tablet. The flowability of the API is largely dependent on its size distribution, as static electric forces and surface charge are proportional to a particle's effective surface area. As a result, uniform powder size is desirable for this final production step. However, if the size of the powder can be controlled in the crystallization step, rather than in downstream processing, milling and granulation can be eliminated entirely.

The proposed thesis focuses on a specific process intensification technique, namely spherical crystallization. Spherical crystallization controls the size of the powder exiting the crystallization step by incorporating the use of a bridging liquid. The bridging liquid induces agglomeration in the system, forcing primary particles to combine together in a controlled fashion. By tuning process parameters and operating conditions, one can generate uniform agglomerates of a desired size with significant flowability enhancements. With a proper understanding of these mechanisms, eliminating milling/ granulation from the pharmaceutical production line can have significant economic impact and can decrease production time to market.

1.3 Overview of Research Objectives

The proposed thesis involves three key aspects, each centered on process intensification in the OBC. The first topic (Operating Regime Map) involves identifying the system parameters that allow for adequate heat and mass transfer, while maintaining solid suspension and minimal system dispersion. More specifically, the three operating parameters that dictate this regime are net flow rate (expected mean residence time), oscillation amplitude, and oscillation frequency. The impact of these parameters was experimentally measured through the comparison of residence time distributions (RTDs) and physical differences were observed when generating turbulence from a piston instead of a pump. Application-based operating regions were determined for both single and dual phase systems. After determining the proper operating zones in the smaller DN6 model of the OBC (holdup of 300mL), these parameters were scaled to the larger DN15 (holdup of 2500mL) and this theory was validated experimentally.

The second research objective was to implement spherical crystallization in the OBC, such that it may also be used as a process intensification size control strategy. The approach for implementing this technique differed for both small and large molecules because of the fundamental challenges associated with each. Small molecules can use a surface adhesion-based mechanism in which a bridging liquid induces agglomeration up to a critical size. However, large molecules, such as proteins, cannot be held together as easily by the bridging liquid, making an emulsion solvent diffusion methodology in droplets more favorable to form agglomerates. These fundamental differences change the approach of spherical crystallization, but ultimately have many similarities in terms of how process conditions can tune the size of the overall agglomerate distributions. In both cases, the oscillation parameters proved to be vital in operational longevity as well as final product quality (agglomerate compactness and sphericity).

The last research objective, Implementation and Scale-up, is really an extension of the first two objectives, but involves a different set of operational challenges. Scaling the spherical crystallization process requires simultaneously scaling the mixing intensity of the system, as the oscillatory energy of the piston scales with the square of its diameter. Maintaining this relationship is vital for crystal suspension, as any settling drastically decreases the quality of the final product and can even lead to system clogging and failure. Lastly, there are significant differences in scaling spherical crystallization for small and large molecules. For the small molecules, the OBC can be scaled to have multiple bridging liquid injection ports, which allows for a tunable agglomerate size as a function of OBC length. However, for large molecules, the system diameter is the more critical parameter because the crystallization kinetics across the droplet is extremely fast. The ratio of the droplet diameter to the system tube diameter proved to

be much more significant in tuning the agglomerate size distribution because droplet coalescence is the primary mechanism for generating large agglomerates, an undesired effect in this process.

In monitoring the spherical crystallization system, several PAT tools were used. In the small molecule work, a focused beam reflective measurement (FBRM) and ultra-performance liquid chromatography (UPLC) system were used to monitor the size of the solid API and liquid concentration respectively. These system parameters were important to monitor the crystallization because they had the highest impact on the overall product quality. However, in the large molecule work, concentration monitoring was not as significant due to the extraordinarily fast kinetics. As a result, the large molecule work was monitored with a Blaze 900; a tool used to generate end to end chord length distributions (a superior measurement to the popular FBRM) as well as advanced online microscopy. The Blaze 900 gave significant insight into the early “life” of the droplets as they were injected into the OBC and provided critical data regarding the mechanism associated with this unique crystallization technique.

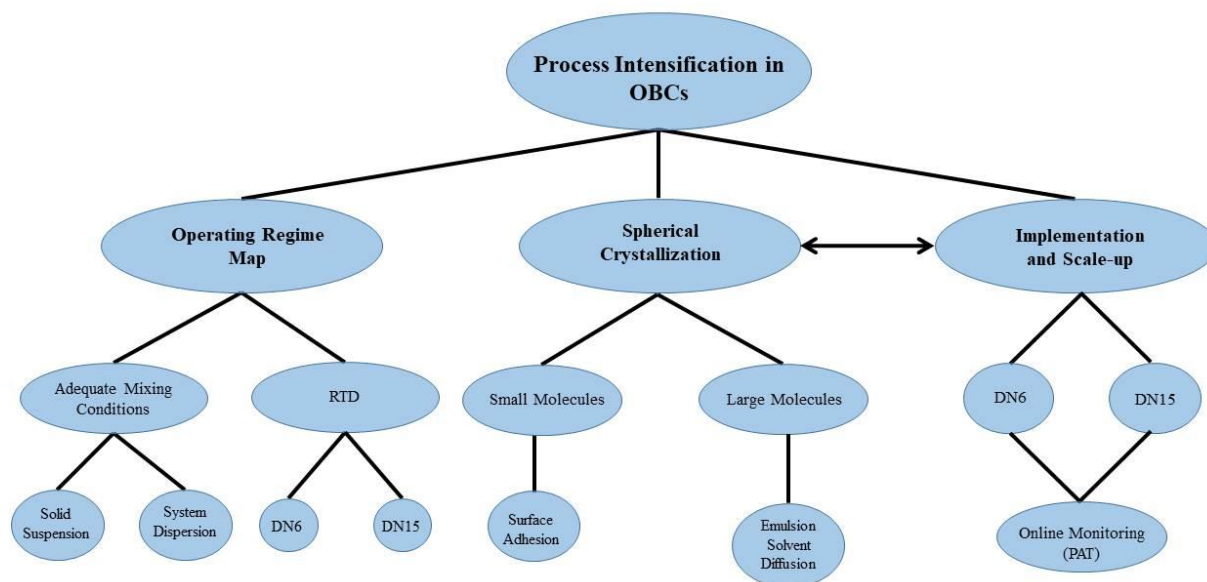


Figure 1.1 Hierarchical thesis diagram

1.4 References

- [1] Etchells, J. C. (2005). Process Intensification. *Process Safety and Environmental Protection*, 83(2), 85–89.
- [2] Roberge, D. M., Zimmermann, B., Rainone, F., Gottspomer, M., Eyholzer, M., & Kockmann, N. (2008). Microreactor technology and continuous processes in the fine chemical and pharmaceutical industry: Is the revolution underway? *Organic Process Research and Development*, 12(5), 905–910.
- [3] Acevedo, D. A., Ling, J., Chadwick, K., & Nagy, Z. K. (2016). Application of Process Analytical Technology-Based Feedback Control for the Crystallization of Pharmaceuticals in Porous Media. *Crystal Growth & Design*, 16(8), 4263–4271.
- [4] Acevedo, D. A., Peña, R., Yang, Y., Nagy, Z. K. Evaluation of Mixed Suspension Mixed Product Removal Crystallization Processes Coupled with a Continuous Filtration System. *Chemical Engineering and Processing: Process Intensification*. (2016).
- [5] Alvarez, A. J., & Myerson, A. S. (2010). Continuous Plug Flow Crystallization of Pharmaceutical Compounds. *Crystal Growth & Design*, 10(5), 2219–2228

2. LITERATURE REVIEW AND CASE STUDIES

2.1 Overview of Crystallization

Crystallization is a common purification and separation technique that causes a targeted molecule to undergo a liquid to solid phase transition under controlled conditions that allow for impurity rejection within the crystal lattice. Traditionally, for manufacturing purposes, crystallization is primarily used for high purity products; i.e. specialty chemicals^[1], active pharmaceutical ingredients^[2], agricultural additives^[3], etc. It's often considered a cheap, efficient alternative to other, more complicated purification techniques like membrane separation^[4] and chromatography^[5] and often has a process yield greater than 90%^[6].

One of the reasons crystallization is popular for a variety of applications is that the final product is given in the form of a solid. Solid products are generally more chemically stable than their liquid and gas counterparts, meaning the product has an extended shelf life^[7]. Generally speaking, manufacturers much prefer solid products (as opposed to liquids), even if the final product must be administered as a liquid, because it is much cheaper to transport solids than liquids. Agricultural products are a great example of this concept. Dense, high potency, agricultural compounds are produced as solids before being distributed to consumers. Consumers are then responsible for dissolving these compounds in water before ultimately applying it on crops for the intended purpose. Producing compounds with this strategy does, however, add a layer of complexity from a particle engineering perspective. These compounds must now be engineered for quick dissolution kinetics and high dispersion stability, as these aspects are important for the consumers using them.

In characterizing a crystal, some important terminology is useful in describing the critical quality attributes (CQAs) of different products. For example, crystal form (also called

polymorphic form) refers to the packing structure of the crystalline lattice. A given molecule can have a variety of crystal forms, while still being chemically equivalent to each other. Although this characteristic does not seem industrially relevant, active pharmaceutical ingredients of different forms can have drastically different biochemical effects on patients, dissolution profiles, aqueous solubility, and bio-toxicity^[8]. Therefore, in drug discovery and crystallization, determining each polymorphic form of a drug is important prior to clinical testing.

Another physical property worth considering in designing crystallizations is the crystal habit. Crystal habit or morphology refers to the shape of the individual crystals making up the bulk powder. However, habit and morphology are not considered synonymous. Habit refers to the crystal shape as defined by relative crystal length to width, whereas morphology refers to crystal facets having the same shape, independent of aspect ratio. The efficiency of downstream processes like filtration and drying are highly impacted by crystal habit^[1]. Crystals with high aspect ratios, like needles and plates, tend to clog filters and inhibit performance^[9]. Similarly, with drying processes, these types of particles lock in moisture and are easy to break with any form of agitation. Breakage occurring in this manner often generates a large number of small particles (often referred to as fines), which present toxicological hazards to plant operators as they are easily dispersed into the air^[10]. Crystal habit, although extremely difficult to modify in most cases, is largely affected by solvent composition, supersaturation rate, and even solution history.

Crystallization is by far the most important separation/ purification technique for the pharmaceutical industry. Developing an appropriate formulation must be reproducible and meet strict FDA regulations^[11]. Moreover, many challenges exist in trying to scale a benchtop crystallization process into commercial scale. Significant changes in physical properties often

occur when scaling a process, due to unavoidable changes in micromixing and local supersaturation which affects the preferential growth of crystal facets^{[6], [12], [13]}.

2.2 Phase Diagrams and Polymorphic Forms

The first step in designing any crystallization process is to understand the molecule's phase diagram through a series of solubility screenings^[14]. A molecule's thermodynamic solubility depends on solution temperature, composition, and pressure (albeit pressure is often omitted as the first two are much easier to manipulate in commercial production settings). A molecule's solubility, although a thermodynamic property, greatly impacts the crystallization kinetics by setting the groundwork for supersaturation^[15]. Supersaturation is defined as the concentration of API above the solubility threshold and is primarily responsible for crystal nucleation and growth (discussed in a later section). Equations for supersaturation (S) and relative supersaturation S^* are as follows.

$$S = c - c^* \quad (1)$$

$$S^* = \frac{c - c^*}{c^*} \quad (2)$$

Note: c is the concentration of API in solution at any time point and c^* is the concentration of API in solution at the solubility threshold. Controlling the level of supersaturation is the key to almost any crystallization. Operating the crystallizer near the solubility curve will result in only crystal growth^[16], while greatly increasing the S^* will result in nucleation events, as discussed in the crystallization mechanisms section of this report. The theoretical yield^[17] of a crystallization process is determined by the starting (A) and ending (B) points on a solubility curve as shown in Figure 2.1. One thing worth noting is that polymorphs each have their own solubility curves that

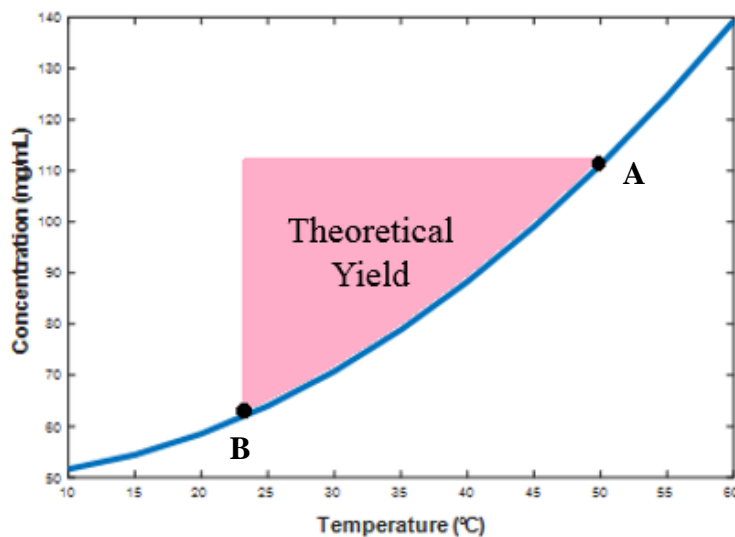


Figure 2.1 Phase diagram for Aspirin in acetonitrile

can be manipulated for isolating the desired form for a drug product^[18]. A formal discussion of polymorphic stability and its effect on solubility is discussed as follows.

Polymorphic forms of drugs often have similar solubility, making them difficult to isolate. They can present themselves as stable, metastable, or unstable and determining a form's stability can be seemingly transient depending on the experimental conditions. To truly understand the nature of polymorphic transitions, one must construct a Gibb's free energy diagram.

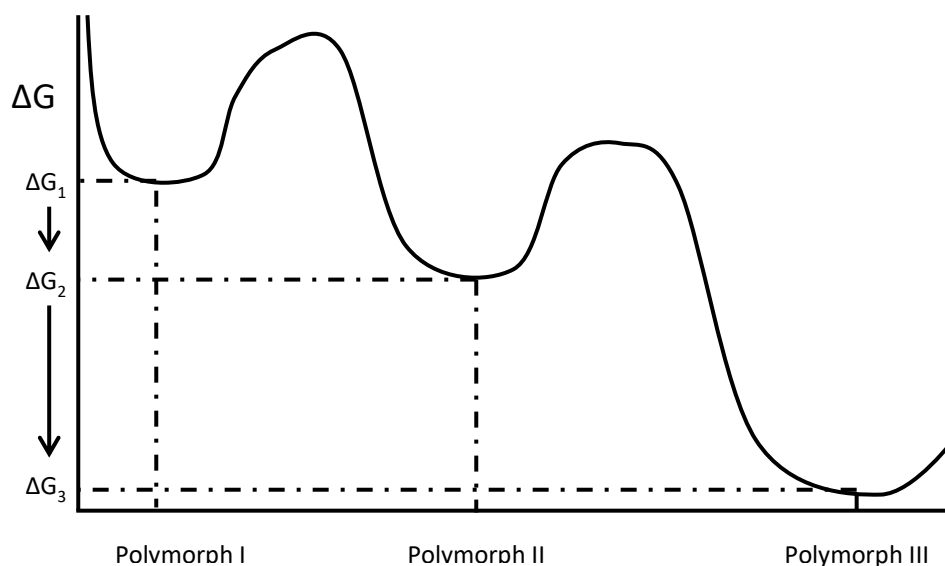


Figure 2.2 Gibb's free energy diagram showing the stability of polymorphs

From Figure 2.2, moving left to right, the existence of local minima shows how a polymorph can be seemingly stable under certain process conditions^[19]. However, with small perturbations, the polymorph can transition into a state of lower free energy, still without guaranteeing that the new minima is indeed the globally most stable form. In the aforementioned example, polymorphic forms I and II are locally stable, often referred to as metastable, while polymorph III is the stable form. In drug product formulations, transitions from metastable forms to stable forms often occur with the presence of moisture, over the course of long storage periods^[20]. To ensure form stability, extensive testing (often through the use of thermal activation methods like Differential Scanning Calorimetry^[18]) is required.

Detecting polymorphic forms is essential in drug formulation development. Typical chemical detection methods like UV-vis and IR spectroscopy are unable to distinguish between polymorphic forms because they work through the excitation of certain functional groups on the molecule (most commonly conjugated aliphatic functional groups, aromatic systems, or chromophores). UV-vis and IR methods only measure the concentration of API in solution and polymorphs only exist in the solid form, making these methods inappropriate for detection. Raman and Near-IR spectroscopy are the only online tools available for real time detection of polymorphic forms^[21]. Offline detection methods are more common and include x-ray diffraction and Raman spectroscopic microscopy.

Slight solubility differences in polymorphic systems are the most common way to isolate a desired form^[22]. The solubility of these systems can be broken up into two categories for dimorphic (2 polymorph) systems: monotropic and enantiotropic. Monotropic systems occur when the Gibbs free energy between two polymorphs is never equal over a given temperature range of interest. Enantiotropic systems occur when the Gibbs free energies between the two

polymorphs are equal and cross in a given temperature range^{[18], [21]}. This distinguishing feature is best described below in Figure 2.3.

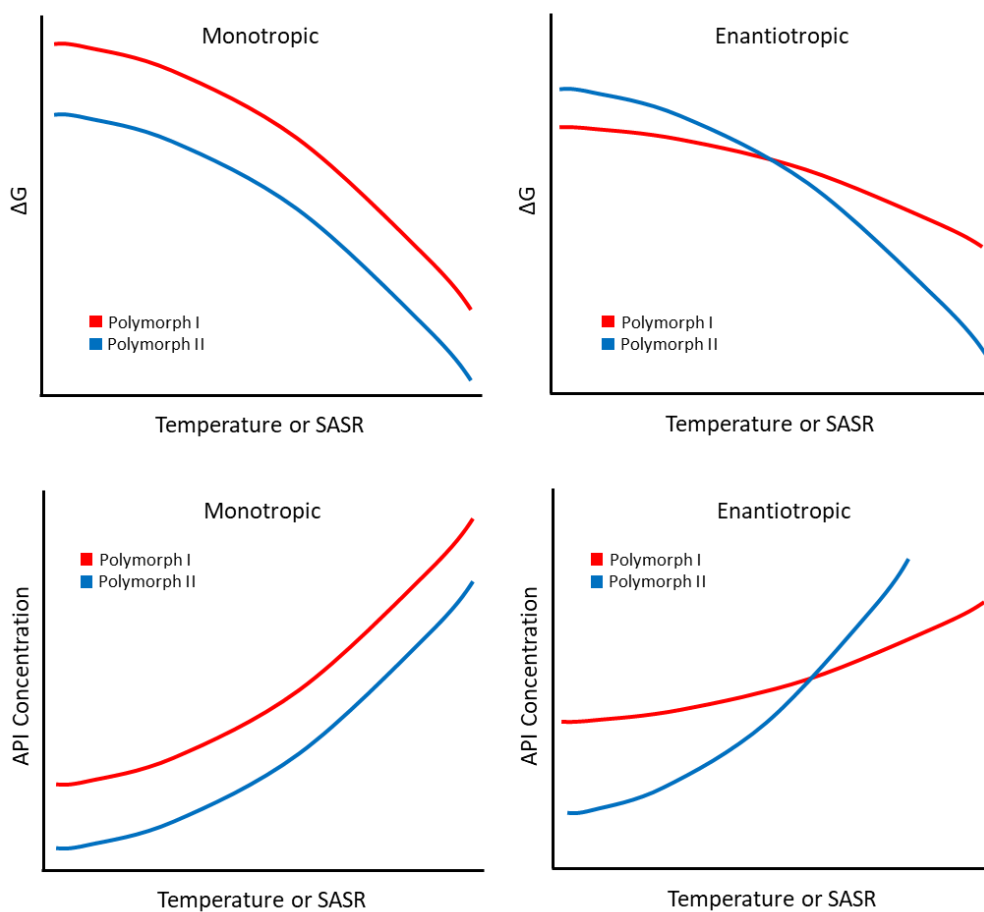


Figure 2.3 Monotropic vs enantiotropic polymorphic systems

In the above example, for monotropic polymorphs, isolating form II is much easier than form I because the crystallizer can be operated such that form II has supersaturation, while form I is unsaturated. Realistically, the crystallizer can also be operated slightly above form I's solubility profile, as long as form I is not already present, because the crystallizer will lack the supersaturation required to initial primary nucleation for form I. This technique is typical for seeded crystallizations and will be discussed in further detail in section 2.3. If form I was the desired form, instead of form II, isolation with this technique becomes impossible. If this is the

case, the most appropriate action would be to adjust the solvent system or composition such that the relative solubility of the desired form is lower than that of the undesired form.

In the event that the system is enantiotropic, similar strategies are useful for isolation, keeping in mind that the end point for the crystallization is of highest importance. If the crystallizer is in phase equilibrium, then the end point of the crystallization will determine which polymorphs are present. As a result, the starting point for the crystallization is only useful for the kinetics of the process, as transitioning from a metastable form to the stable form under certain process conditions can be a lengthy process^[23]. Unlike monotropic systems, enantiotropic systems do allow for either form to be isolated, but with the contingency that the yield of the process may not be as high. For example, starting from point A and finishing at point B would allow form I to be isolated, but the overall yield of the process may only be 30% or 40%. However, starting from point A and finishing at point C would isolate form II and the yield would be on the order of 80%. In this sense, enantiotropic systems, although more complicated kinetically, have favorable thermodynamics for isolating either form.

2.3 Crystallization Mechanisms

In crystallization, two primary mechanisms dominate the system; that is, nucleation and growth^[24]. Manipulating these two mechanisms have drastic impacts on the final product's crystal size distribution (CSD)^[25]. If the theoretical yield of the system is fixed, as shown in Figure 2.1, then the number of crystals in the system (as determined by nucleation events) in combination with preferential crystal growth, determine how the fixed available supersaturation in the system is distributed. If size independent growth is to be assumed, then the number of nuclei in the system solely determines the size of crystals in the product. For example, knowing the available supersaturation is fixed, a small number of nuclei will yield large crystals, while

increasing the number of nuclei will yield smaller crystals. As a result, controlling these two mechanisms is the key to manipulating the end point crystalline product and is often referred to as direct nucleation control (DNC)^{[26], [27]}. The details of each of these mechanisms will be described in detail in this section, in addition to several other secondary mechanisms including agglomeration, breakage, and coalescence.

2.3.1 Nucleation

Nucleation is defined as the birth of ordered crystalline clusters and is the first step in traditional crystallization processes^[24]. Separated into two types, primary and secondary, nucleation requires higher supersaturation relative to growth^[28]. Primary nucleation is defined as the birth of new ordered crystalline clusters from a purely liquid solution. Secondary nucleation requires less supersaturation than primary and is defined as the birth of ordered crystalline clusters in the presence of existing crystals^[29].

Primary nucleation is also broken up into two subcategories. Homogeneous primary nucleation is the formation of ordered crystalline clusters without help from external factors such as the walls of the crystallizer, immersed probes, or the impeller. Heterogeneous primary nucleation is the formation of ordered crystalline clusters with the help of these external factors^[30]. The presence of these external factors act as activation sites for nucleation to occur and can be seen as catalyzing the start of nucleation. As a result, heterogeneous primary nucleation is by far the most common type of primary nucleation in practical settings^[31].

Secondary nucleation is the most commonly targeted mechanism in modern pharmaceutical crystallization because it can occur at low supersaturation^[27]. Energy generated from crystals coming into contact with an agitator or high shear stresses in the boundary layer of moving fluids are the most common sources of secondary nucleation. Most industrial

crystallizers are “seeded” with small crystals at the starting point of the process to avoid primary nucleation. Primary nucleation is a stochastic process and is extremely unpredictable due to an unprecedented dependence on a number of external factors like solution history, agitation rate, and local supersaturation^{[32], [33]}. By seeding the crystallizer at the start, the crystallizer can be operated at a low supersaturation, avoiding unpredictable primary nucleation altogether.

Modeling nucleation kinetics, while not the primary focus of this thesis, is briefly mentioned for completeness. Generally speaking, nucleation kinetics is poorly understood^[22] and most models fail to accurately describe a system, even with a large number of fitting parameters. The stochastic nature of nucleation makes translating fitting parameters between systems, especially in regards to scale-up, rather poor^[24]. Nevertheless, the two most common primary nucleation models are as follows.

Classical nucleation theory

$$J = A \exp\left(\frac{-16\pi\gamma^3 V_m^2}{3k^3 T^3 (\ln S)^2}\right) \quad (3)$$

Empirically Fitted Expression

$$J = k_b S^b \quad (4)$$

Note: J is the nucleation rate, A is a pre-exponential factor, γ is the solid-liquid interfacial tension at the cluster surface, V_m is the molar volume of the solute, k is the Boltzmann constant, T is temperature, S is supersaturation, k_b is the kinetic rate constant, and b is the exponential nucleation constant. In practice, Eqn 3 is difficult to use, since γ is unmeasurable and is often fitted to data along with A. Eqn 4 is more common and a simpler approach for fitting data to practical crystallizations. However, both equations do not scale effectively since local supersaturation is a strong function of micromixing.

2.3.2 Growth

Crystal growth can occur at any level of supersaturation and is best described as a surface deposit of API onto an existing crystal facet^[34]. The process for crystal growth occurs over the course of two steps. The first step is the diffusion of solute in the bulk solution to the surface of an existing crystal. From there, the local supersaturation creates a gradient in which a liquid to solid phase transition occurs, depositing API solute onto a crystal facet, integrating the new material into the crystal lattice^[35]. Crystal growth is the primary targeted mechanism for industrial crystallization, as it is the major contributor to controlling the CSD of the final product^[9]. Like primary nucleation kinetics, crystal growth rate can be modelled using an empirical fitting expression.

$$G = k_g S^a \quad (5)$$

Note: G is the growth rate, S is the supersaturation, k_g is the kinetic rate constant and a is the exponential growth constant.

In a seeded crystallization, the goal of the process is to have growth dominated depletion of supersaturation. By avoiding as much nucleation as possible, reproducible crystallization processes can be achieved, as growth mechanisms are much more predictable and consistent than nucleation. Seeded crystallizations are also useful for obtaining product of a desired polymorphic form. By seeding with the desired form, often times, supersaturation can be kept low enough to avoid nucleation of the undesired form, making this technique invaluable for high purity products^[36].

2.3.3 Agglomeration, Breakage, and Coalescence

Other factors that alter final product CSD primarily include agglomeration and breakage, but coalescence also plays a role in droplet phase systems^[37] like the lysozyme work discussed in

Chapter 5. Each of these mechanisms is independent of nucleation/growth and act as secondary effects in the crystallizer. Agglomeration is defined as the coming together of two daughter crystals to form a larger mother particle^[38]. Typically, agglomeration is undesired in industrial crystallizations and should be avoided because it adds an additional mechanism that must be manipulated to generate the desired CSD^[39]. If left uncontrolled, agglomeration can generate bimodal CSDs^{[33], [40]} with the first node being comprised of unagglomerated daughter particles and the second node consisting of the agglomerated mother particles.

Crystal breakage is mechanically the opposite of agglomeration in that a mother particle fractures into two daughter particles. Litster categorizes breakage into three different mechanisms based on their fragment distributions^[24]. Cleavage occurs when a particle undergoes tensile stress resulting in major fracture. The resulting daughter particles are relatively the same size. Impact fracture occurs from particle interactions with the impeller or vessel wall at high velocities. The resulting daughter particles are generally smaller than those from the cleavage mechanism. The last mode of breakage is attrition, relatively weak surface breakage. Attrition occurs when surface forces are not strong enough to crack the mother particle. Surface attrition results in a mother particle of roughly the same size and many fine daughter particles. In this spherical agglomeration work, attrition is by far the most common mode of observed breakage^[12].

2.4 Batch Crystallization

Batch crystallization is the preferred mode of operation in the pharmaceutical industry due to small lot sizes, straight forward scalability, and it is much easier to grow large crystals by controlling cycle time, since continuous processes encounter residence time distribution issues, as discussed in a later section^{[26], [31], [41], [42]}. Most batch crystallizations control supersaturation

by cooling the crystallizers over time, but semi-batch processes which control supersaturation with the addition of an antisolvent is also fairly common^[43]. The rate at which supersaturation is generated by either (or by combining both) of these methods drastically impacts the size and quality of the final crystals formed^[44]. The following case study, although brief, illustrates the impact of cooling rate on crystal quality for Aspirin.

2.4.1 Batch Crystallization Case Study

Introduction

Cooling crystallization is an important industrial process for the generation of high purity pharmaceutical products. In this experiment, the critical quality attribute (CQA) is crystal size because size is directly correlated to better downstream processing (filtering, drying, milling, tableting), solids handling^[40], and bioavailability^[45]. Smaller particles are typically undesirable and are often generated by nucleation dominated systems (choice of active pharmaceutical ingredient (API) and operating conditions). Similarly, quick cooling rates significantly increase the number of fine particles and therefore discourage growth mechanisms (less supersaturation is available for growth to occur)^[46]. Furthermore, this experiment aims to distinguish the advantages of slow linear cooling (SLC) over natural cooling (NC) in the batch crystallization of aspirin^{[45],[47]}.

Experimental Method

The crystallization of aspirin occurred through two experiments in series (NC immediately followed by SLC). Approximately 82g of Aspirin was dissolved in 237g (300mL) of ethanol in a stirred¹ (350rpm) 500mL jacketed crystallizer. In both experiments, when the

¹ Three blade retreat curve overhead impeller

temperature of the vessel reached 32°C, 5% (g seed/g solute) seeds were added. As seen by the cooling profiles in Figure 2.4, both experiments began at 40°C and were cooled to 25°C. Each system was seeded to accelerate crystallization kinetics and to avoid primary nucleation events. To monitor the system, a focus beam reflectance measurement (FBRM) probe collected real time measurements of crystal chord length distribution and the number of particles in the system² (counts).

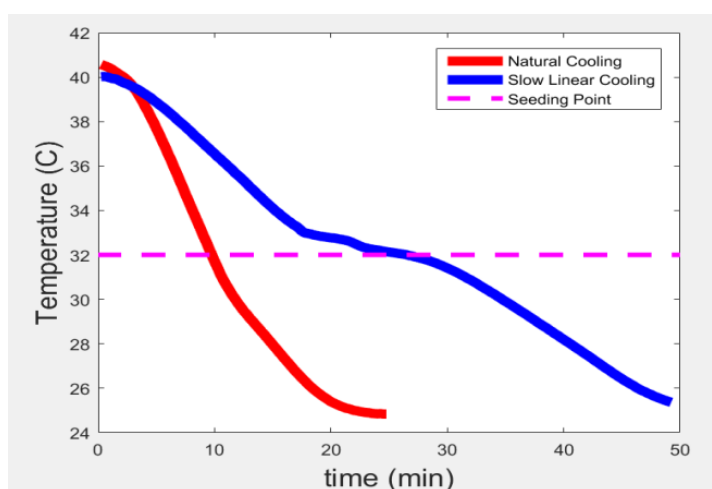


Figure 2.4 Cooling profiles for natural and slow linear cooling rates

² Note that the counts measured are not the actual number of crystals in the system, but an estimate of the number of crystals passing through the probe's signal

A particle vision monitor (PVM) probe was also introduced to the system in order to gain a qualitative measure of crystal quality and size. In order to monitor the concentration of dissolved Aspirin, attenuated total reflectance ultraviolet visible (ATR UV-Vis) measurements were used and processed through a calibration curve³. The final process analytical technology (PAT) tool used is a thermocouple, which monitors the cooling profile within the system. Together, these PAT tools allow for in situ monitoring of the system's operating point in the phase diagram, as seen in Figure 2.5.

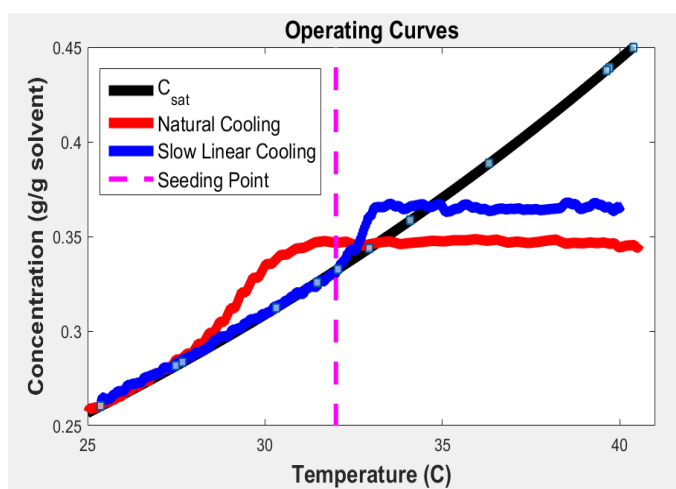


Figure 2.5 Operating curves for each experiment within the phase diagram.

The initial concentration in the SLC experiment is greater than that in the NC experiment because the seeds added to the NC experiment dissolved and contributed to the initial concentration in the SLC experiment.

³ $C = a_0 + a_1A + a_2T + a_3AT$ is the equation used in the calibration model. Note: C is concentration, A is absorbance, T is temperature and a_0 , a_1 , a_2 are constants determined by calimetrics

Results and Discussion

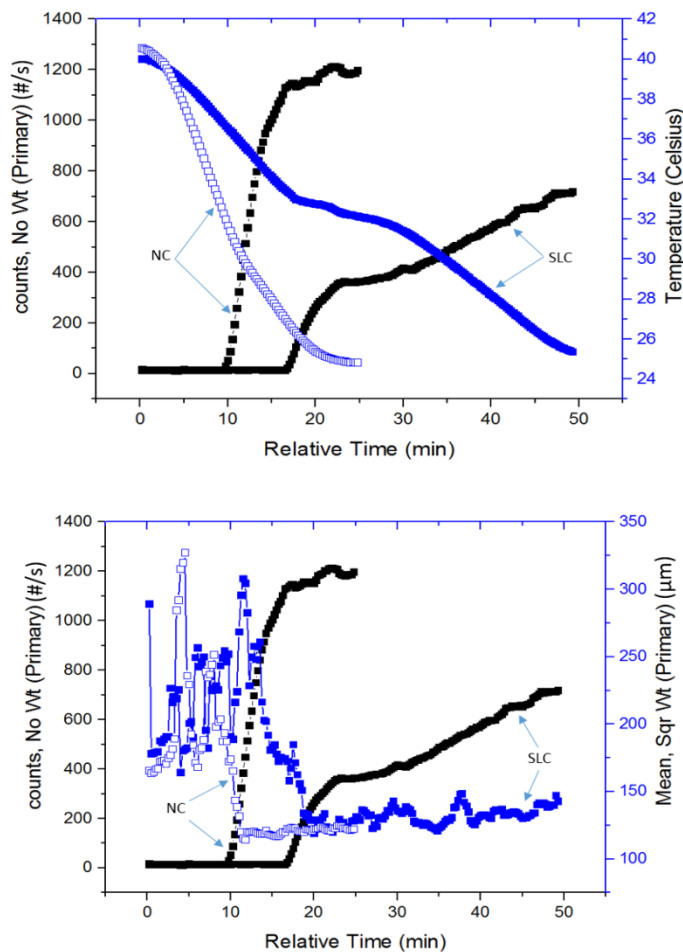


Figure 2.6 (top) Change in counts as the system temperature changes over time. (bottom) change in SWMCL as crystal counts change over time.

For NC, seeding occurs around 10 minutes into the experiment. The number of counts per second then begins to increase as further cooling continues. This increase in the number of counts is likely due to nucleation (both primary⁴ and secondary). A similar trend is seen in the SLC experiment, but this event occurs around 17 minutes into the experiment. From Figure 2.6 (top), the final number of counts for NC is significantly higher than for SLC. However, as seen by the square weighted mean chord length measurements (SWMCL) in Figure 2.6 (bottom), after

⁴ Primary because the presence of particles (seeds) can lower the energy barrier for new particles to nucleate out of solution

seeding in the NC experiment, the particles seem to remain the same size⁵. This difference results from nucleation events occurring faster than growth while following this operating curve. In contrast, the SWMCL measurements in the SLC experiment slightly increase, indicating the presence of some growth within the system. This explanation is further supported by the PVM images contained in the appendix. The crystals resulting from SLC have a more regular shape and are slightly larger in general. Note that the SWMCL measurements in the beginning of each experiment (15-20 min) are noise because there are very few crystals within the system. The number of accounts level off as agglomeration occurs and supersaturation decreases (stopping nucleation and growth events). The dissolution data between experiments was removed for clarity. However, this data did show a spike in the FBRM counts even though heating started. This spike is likely because loosely agglomerated particles (from the end of the cooling stage) broke up therefore increasing the number of counts within the system. The spike later decreases as smaller particles dissolve.

Conclusion

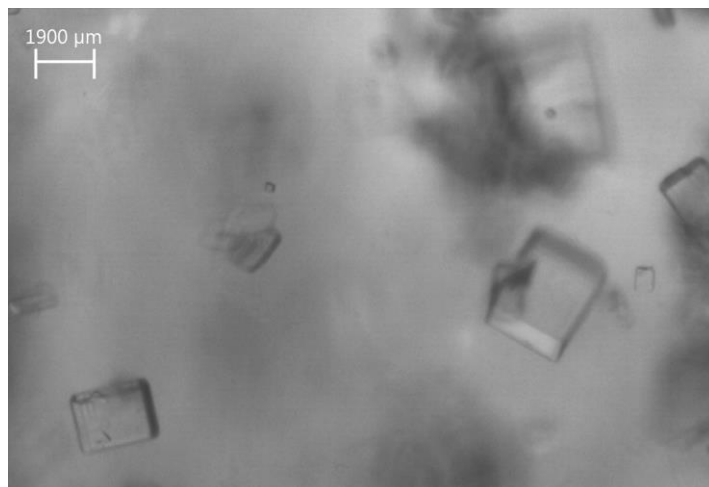
These results support the literature that links slower cooling rates with larger, more agglomerated particles. In this comparison, SLC is better than NC. However, SLC is not the optimal cooling profile (Worlitschek 891). Future work should include computer-based simulations with nucleation and growth kinetics in order to determine the optimal cooling profile. Because nucleation kinetics varies significantly between experiments, this model will only be an estimation of the optimal cooling profile. However, this simulated profile will likely lead to larger particle size and possibly a narrower crystal size distribution. Future work could also

⁵ SQMCL is not the crystal size distribution in the system, but an increase in SQMCL would correlate in an increase in crystal size

include varying mixing conditions, when to seed the system, and increasing the batch time in order to promote growth instead of nucleation.

Particle Vision Microscopy

Natural Cooling



Slow Linear Cooling

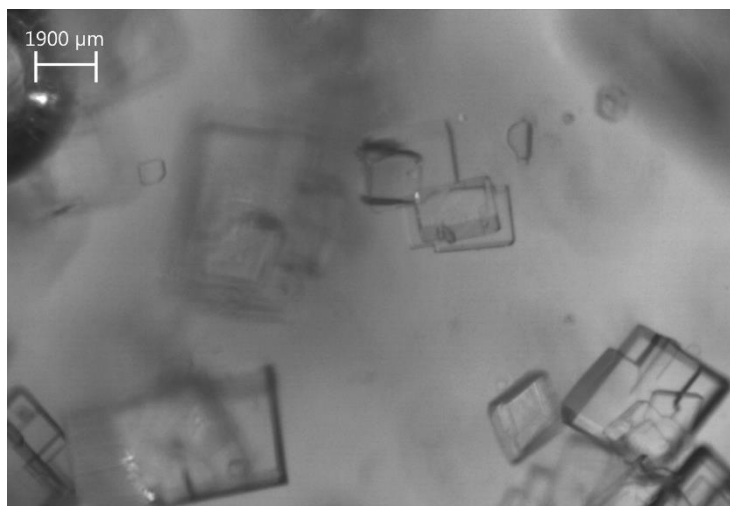


Figure 2.7 PVM imaging from cooling crystallization case study

2.5 Continuous Crystallization Systems

Coupled with rising energy costs^[48] and competition from generic drug manufacturers^[6], inefficient processes are compelling the pharmaceutical industry to move towards continuous operation. Continuous systems offer large scale production with less deviation in product quality after startup (i.e. once the process reaches a stable steady state), reduce material waste by minimizing off spec product with real time control, and require less maintenance and cleaning^[12]. Federal regulatory committees now recognize the potential environmental/ safety benefits of continuous operation, as it limits operator exposure to hazardous powders during solids handling^[49].

There are three common types of continuous crystallizers: mixed-suspension, mixed-product removal (MSMPR) crystallizers (most analogous to stirred tank reactors), plug flow reactors (PFR), and oscillatory baffled crystallizers (OBCs). MSMPR crystallizers have characteristically broad crystal size distributions (CSD) which stem from their equally broad residence time distributions (RTD)^[25]. PFRs are generally better (in regards to the RTD issue), but clog easily and require physically unrealistic lengths to maintain solid suspension through high flow rates. A COBC utilizes sharp or smooth changes in tube diameter (baffles) to create pairs of eddies as the net flow direction changes from forwards to backwards through the oscillation of a piston^[50] (shown in Figure 2.8). COBCs offer linear scale up capabilities, superb heat transfer through high surface area to volume ratios, and narrower CSDs with (near) plug flow operation^[13]. Unlike PFRs, COBCs are able to achieve longer residence times without running into tube length issues because piston oscillations generate turbulence without the use of large flow rates^[51]. Moreover, flow visualization studies have shown that downstream eddy generation is independent of upstream flow^[52]. This independence improves the case for linear scalability, as the mixing mechanism is independent of tube length and the number of baffles

present. Such scalability makes COBCs attractive in the chemical and pharmaceutical industries.

Figure 2.8 describes the internal fluid dynamics of a COBC system.

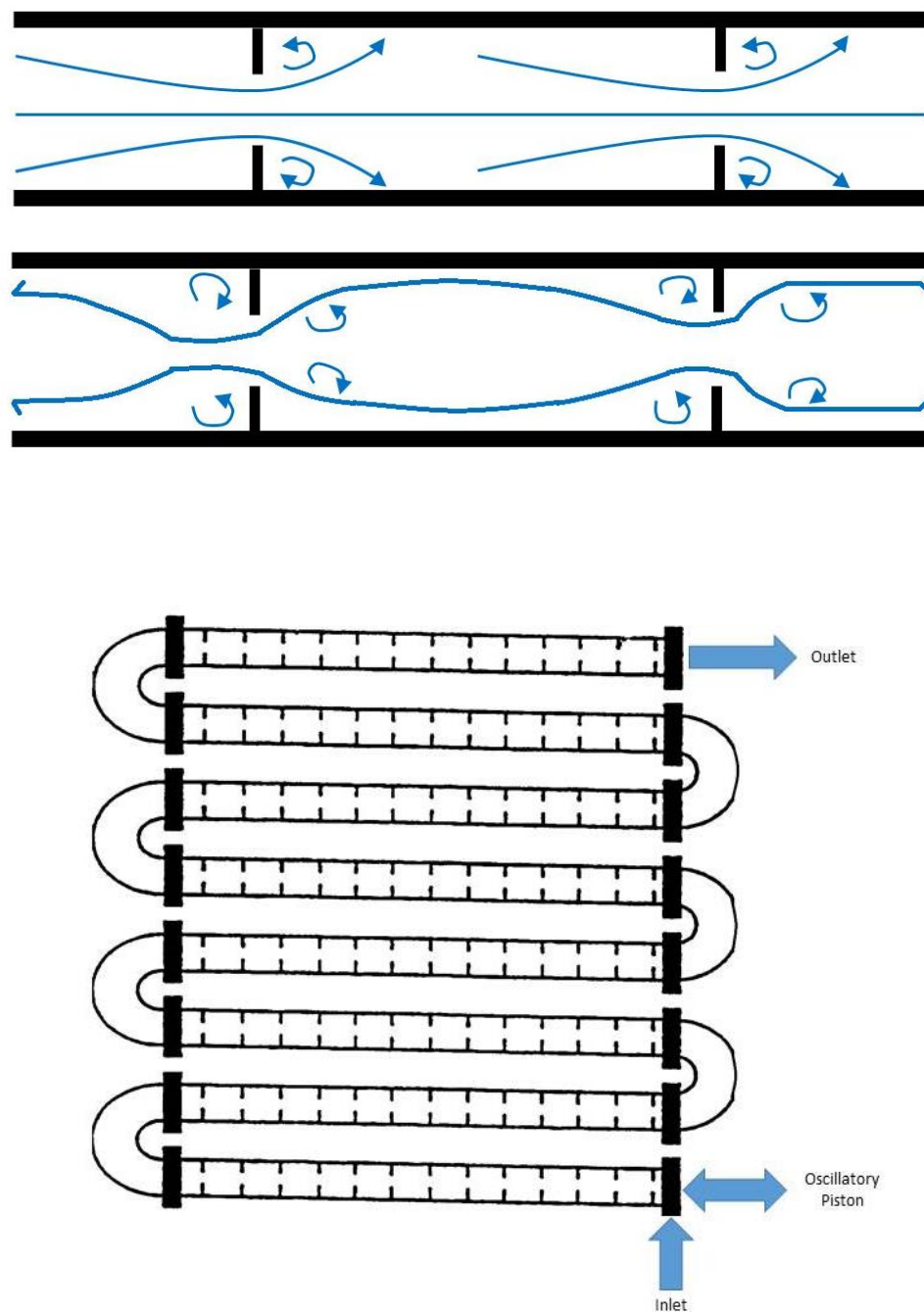


Figure 2.8 (top) Mixing mechanism in an OBC and (bottom) schematic of a typical vertical OBC. Adapted with permission from Ni et al.^{[50],[51]}

2.6 Heat Transfer Coefficient Case Study

Crystallization kinetics are often limited kinetically due to the conformational nature by which molecules must come together to undergo an ordered liquid to solid phase transition^[53]. As previously mentioned, tank based systems have poor micromixing, often creating a heat/concentration gradient across the reactor^{[54], [55]}. These mixing deadzones are primary contributors to variation between product batches. The OBC has been shown to minimize mixing dead zones through the use of baffles and oscillatory piston motion^[56]. To best characterize this mixing efficiency, in addition to the RTD studies presented in Chapter 4, the heat transfer coefficient of the system should also be characterized under a variety of flow conditions.

In an oscillatory plug flow tubular system, several operating parameters dictate the heat transfer coefficient; namely, the axial net flow rate, the amplitude and frequency of the piston, and the jacket temperature profile of the tube segments^{[41], [57]}. Synonymous to how a batch tank system will cool the API solution over time to generate supersaturation, the OBC creates a temperature gradient as a function of tube length to generate a supersaturation profile. By manipulating this supersaturation profile, growth dominated process kinetics can be controlled and changed in real time to affect final product CQAs. However, due to vigorous backmixing in the system, the temperature setpoint of each tube segment can be far different than the process fluid temperature, especially at heat exchanger switchover points (the exit for one heat exchanger, coupled with the inlet for the next heat exchanger in series)^{[33], [58]}. As a result, understanding how the heat transfer coefficient changes with operating conditions is important for predicting the temperature profile of the process fluid inside of the OBC, since having thermocouples at every point is impractical. The heat transfer coefficient calculation, as described by Andy Koswara from Purdue University is as follows.

Determining heat transfer coefficient in a plug flow

Andy Koswara

May 31, 2016

Starting from energy balance in a plug flow and assuming radial symmetry (i.e. no temperature gradient from the surface to the center of the tube):

$$\frac{\partial T}{\partial t} = \frac{k}{\rho C_p} \frac{\partial^2 T}{\partial z^2} - u \frac{\partial T}{\partial z} + \frac{2h}{R\rho C_p} (T_s - T), \quad (1)$$

Assuming steady state and dividing by superficial velocity u :

$$0 = \frac{k}{u\rho C_p} \frac{\partial^2 T}{\partial z^2} - \frac{\partial T}{\partial z} + \frac{2h}{uR\rho C_p} (T_s - T), \quad (2)$$

Since we only have two temperature probe at the beginning and end of each segment, we dont have enough information to account for the second order term. Thus, we need to operate at a sufficiently high flow-rate such that the conduction term is negligible. In turn, (2) becomes:

$$\frac{dT}{dz} = \frac{2h}{uR\rho C_p} (T_s - T). \quad (3)$$

Substituting the following newly defined variables into (3):

$$\begin{aligned} \alpha &= \frac{2h}{uR\rho C_p} \\ T' &= T - T_s \\ \rightarrow \frac{dT'}{dz} &= \frac{dT}{dz} \end{aligned}$$

we get:

$$\begin{aligned} \frac{dT'}{dz} &= -\alpha T' \\ \rightarrow \int_{T'_i}^{T'_o} \frac{1}{T'} dT' &= \int_{z_i}^{z_o} -\alpha dz \\ \rightarrow \ln \frac{T'_o}{T'_i} &= -\alpha(z_o - z_i) \\ \rightarrow \ln \frac{T_i - T_s}{T_o - T_s} &= \alpha \Delta z \end{aligned} \quad (4)$$

Note: T_i and T_o are the inlet/outlet temperatures of the process fluid respectively, T_s is the surface or jacket temperature, ρ is the density of the process fluid, C_p is the heat capacity of the process fluid, k is the thermal conductivity of the reactor glass, z is the axial distance between the inlet and outlet, R is the ideal gas constant, u is the superficial velocity, and h is the heat transfer coefficient. From eqn (4) of the document, the natural log term can be plotted against Δz and the slope of the line formed is defined as the lumped heat transfer coefficient, α .

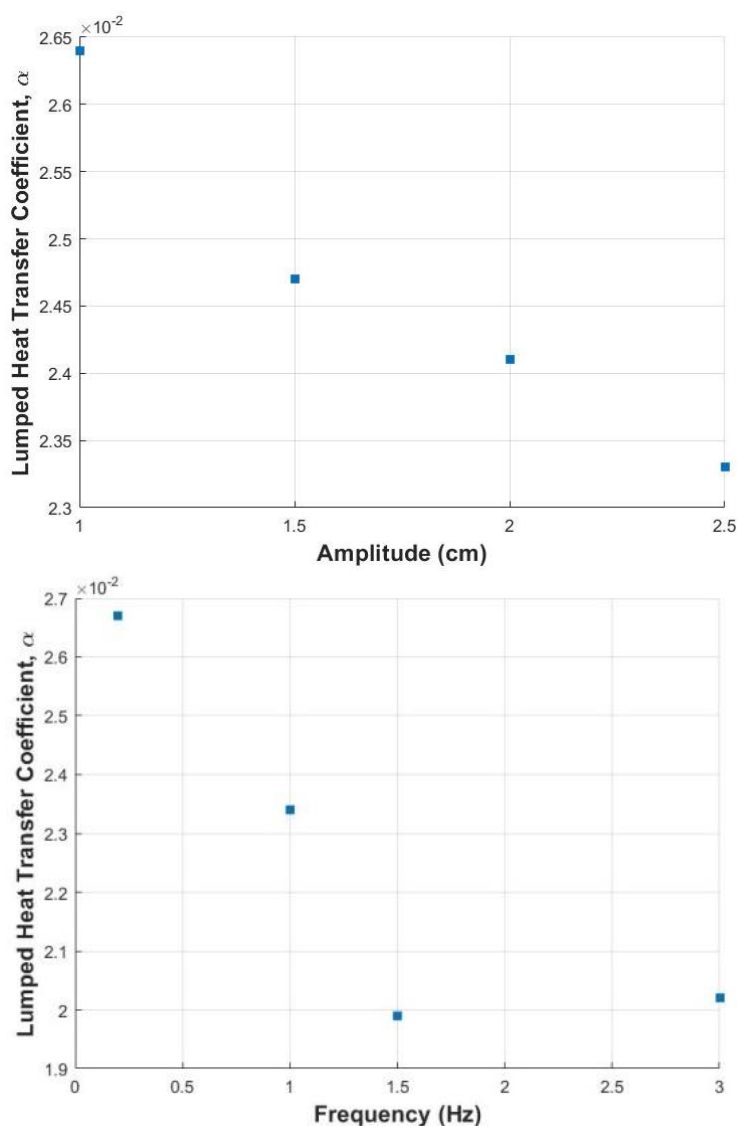


Figure 2.9 (top) the effect of piston amplitude on heat transfer coefficient and (bottom) the effect of piston frequency on heat transfer coefficient

Using this methodology, heat transfer coefficients were calculated to be on the order of 10^{-2} with little variation. Of the three key variables of interest, axial net flow rate did not show a significant correlation, most likely because the flow rates tested (30mL/min – 200mL/min) were dominant compared to the axial oscillations of the piston. However, the heat transfer coefficient showed a negative correlation with both the piston amplitude and frequency. This result is most likely due to the fact that axial backmixing reduces the temperature gradient across tube sections near the switchover points. Strong axial backmixing creates uniformity rather than distinct temperature operating zones.

2.7 Overview of Spherical Crystallization

Batch crystallization, a prevalent purification step in pharmaceutical processes, traditionally lacks CQA control, leading to variation between batches^[21]. Consequently, several additional unit operations must adjust crystal size and morphology to desired ranges for proper dissolution kinetics and bioavailability. Although Nagy and several others successfully implement control approaches to resolve these issues in batch systems^[15], nonideal mixing often leads to complex nonlinear partial differential equations^[31]. When crystal growth naturally forms long plates or needles, several downstream issues arise in regards to filtering, drying, and solids handling^[1]. These issues lead to an additional need for size adjustment (e.g. grinding, milling, and granulation), dramatically increasing the costs associated with achieving the desired micromeritic properties^[59].

Spherical crystallization is an alternative method that utilizes a bridging liquid to simultaneously combine high aspect ratio crystals into spheres, while nucleation and growth occur^[60]. Although the spherical agglomeration mechanism is system specific and currently unknown in the COBC, Kawashima, Peña, and others predict two mechanisms of agglomerate

formation. The first is emulsion based in which the counter diffusion of immiscible good and poor solvents drive supersaturation and initiate crystallization inside the emulsion. The second proposed mechanism dictates that a bridging liquid preferentially wets the surface of crystals, while numerous inter-crystal collisions result in adhesion.^{[40], [61]} To truly understand the mechanism in the COBC, advanced in situ imaging devices such as Particle Vision and Measurement (PVM) probes must be implemented.

Nevertheless, spherical crystallization considerably reduces the number of processes required to manufacture the final dosage form, even allowing for the addition of excipients before direct compression into tablets^[48]. Other benefits of spherical agglomerates include free flowability, more uniform dissolution patterns, and narrower size distributions²¹. The bridging liquid droplet size^[62] and addition rate^[63] allow one to tailor the size of the spherical agglomerates to specified ranges, adding an additional degree of control and further promoting process intensification.

2.8 Process Analytical Technology Tools and Their Role in Spherical Agglomeration

When scaling up self-nucleating continuous systems, an added degree of product variability comes into play as nucleation kinetics are highly stochastic^[21]. However, online process analytical technology (PAT) tools can monitor the system, allowing one to adopt process parameters that minimize off spec product formation in real time^[52]. Of utmost importance in spherical agglomeration is the size of the primary crystals incorporated in the structural lattice. These primary particles dissociate from the original agglomerate and then further dissolve within the body. Therefore, the size of these primary particles plays a vital role in bioavailability and targeted drug delivery^[22]. A focused beam reflectance measurement (FBRM) probe uses laser backscattering to measure a chord length distribution of suspended crystals without invasively

altering crystal size or morphology^[64]. This in situ measurement relates to the actual size of each passing particle, allowing for real time process parameter adjustments, e.g. changes in antisolvent flow rates, cooling rates, etc. Additionally, FBRMs in continuous processes are useful for determining if the system is operating in steady state^[65]. When chord length distributions no longer fluctuate or the oscillations become predictably repetitive, then the system dynamics (crystal nucleation and growth) are approximately independent of time.

Ultra-performance liquid chromatography (UPLC) is another useful PAT tool for monitoring not only component concentrations, but also steady state. UPLC techniques differ from high performance liquid chromatography (HPLC) techniques in that they utilize columns with smaller diameters, smaller particles^[66], and therefore higher pressures^[67] to increase peak capacity (defined as the ‘number of peaks resolved per unit time’) and decrease retention time^[68]. Specific to the COBC, the UPLC offers an offline method to construct a concentration profile as function of length. This functionality will prove useful when dividing the COBC into three specific operating zones for the small molecule spherical agglomeration: nucleation, growth, and agglomeration.

For the large molecule spherical agglomeration work, an additional PAT was used. The Blaze900 (Blaze Metrics, LLC) uses high resolution microscopy and particle system analytics to estimate end to end chord length distributions. Because the large molecule spherical crystallization system is occurring in droplets (see Chapter 5 for details), the advanced analytics of the Blaze900 was required to representatively monitor the system. Multiphase (L/L) systems prove difficult for the FBRM measurement because the laser backscatter is highly dependent on the optics of the laser, while the oscillatory motion of the OBC adds an added degree of difficulty. However, because the Blaze uses advanced microscopy at 532nm illumination, end to

end chord length distributions can be drawn across high resolution images, ensuring the measurement of the solid phase. Additionally, the Blaze900 system was used to predict the process dynamics and mechanisms, while still actively monitoring steady state.

2.9 Dimensionless Operating Parameters

In operating the OBC system, mixing intensity is highly important. Four dimensionless parameters define the fluid flow patterns in an OBC, that is, the oscillatory Reynolds number (Re_o), the net flow Reynolds number (Re_n), the Strouhal number (St), and ψ , the ratio of oscillatory and net flows.

$$Re_o = \frac{2\pi f x_0 \rho D}{\mu} \quad (7)$$

$$Re_n = \frac{\rho u D}{\mu} \quad (8)$$

$$St = \frac{D}{4\pi x_0} \quad (9)$$

$$\psi = \frac{Re_o}{Re_n} \quad (10)$$

Note: x_0 is the piston amplitude, ρ is the solution density, D is the diameter of the tube segment, u is the mean superficial velocity and μ is the solution viscosity. The St measures effective eddy propagation by simply taking the ratio of the column diameter to piston stroke length^{[12], [50]}. The Re_o measures the intensity of the oscillations generated by the piston and therefore, the mixing imposed on the fluid. Similar to traditional fluid dynamics, the Re_n is a ratio of inertial to viscous forces. The ratio of both Re results in the dimensionless mixing parameter ψ , a measure of oscillatory versus net flows. Large ψ values result in “well-mixed” baffles^{[12], [69]}. Reis et al.

showed that flow separation occurs at $Re_o > 50$, leading to asymmetric vortex formation^{[65], [67]}. In other words, radial mixing at large Re_o is no longer uniform, largely due to ‘fluid slipping’ at the wall’s surface. One last consideration in the determination of operating parameters for a given system is the over-creation of eddies. For relatively low St numbers ($St < 0.13$), vortex generation extends into adjacent baffles, leading to irregularities in mixing and large dispersion/back-mixing^[68]. In contrast, relatively high St numbers ($St > 0.2$) lead to ineffective eddy generation within each cavity, which could impact particle suspension in two phase systems^[68].

2.10 Geometric Considerations in Oscillatory Baffled Systems

| COBC Model | D (mm) | d _o (mm) | l _b (mm) | Glass Thickness (mm) |
|------------|--------|---------------------|---------------------|----------------------|
| DN15 | 16 | 7.5 | 21.4 | 2 |
| DN6 | 6.85 | 3.5 | 11 | 3 |

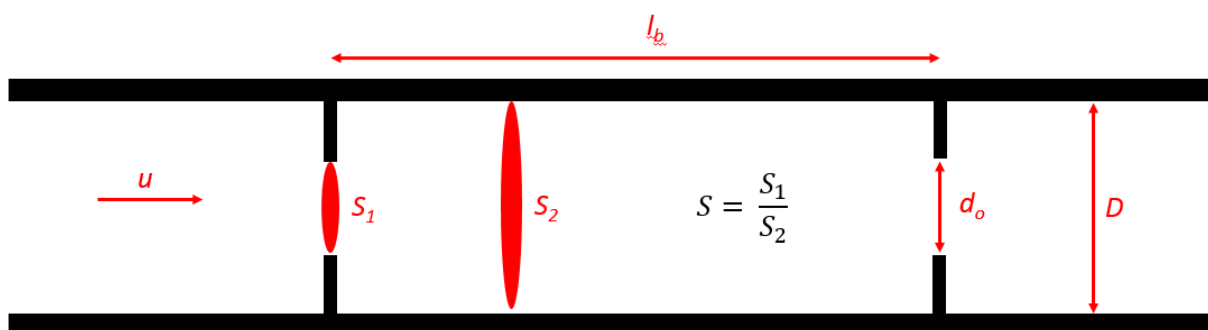


Figure 2.10 Illustration of COBC geometry with dimensions. Adapted from McDonough^[67]

Conventional oscillatory baffled reactors vary in geometry and have diameters greater than 15mm^[67], while the newer (more recent) mesoscale reactors have diameters in the range of 4-5mm^[51]. Regardless of scale, the commercial application of oscillatory systems are generally limited to purely liquid systems, as plug flow operation in a two phase (solid/liquid) system is

still a topic of interest amongst academics, especially for shear-sensitive systems^[70]. In the commercialization of an oscillatory flow system, two common approaches are used: design the baffle geometry such that mixing is maximized or design such that frictional losses are minimized^[41].

Flow characteristics in oscillatory systems are largely governed by both operating and geometric parameters^[71]. As described in Figure 2.10, S controls the size and shape of eddies formed, while adequate distance between baffles (l_b) ensures fully developed vortices and the minimization of mixing dead zones^[72]. This balance provides the foundation for solid suspension during crystallization, which is absolutely necessary to avoid settling and clogging. A major concern in designing crystallization systems is minimizing shear stress, as it can lead to crystal breakage and bimodal size distributions. Therefore, a smooth constriction or “integral baffle” was chosen for this application. Integral baffles provide a low shear environment, while also generating pairs of vortices^[57]. These baffles differ from helical or central axial baffles (not shown), which are primarily used for immiscible liquid-liquid systems, where inter-phase homogeneity is desirable^[73].

2.11 References

- [1] M. A. Lovette, A. R. Browning, D. W. Griffin, J. P. Sizemore, R. C. Snyder, and M. F. Doherty, "Crystal shape engineering," *Ind. Eng. Chem. Res.*, vol. 47, no. 24, pp. 9812–9833, 2008.
- [2] D. S. Palmer *et al.*, "articles Thermodynamic Cycle," *Mol. Pharm.*, vol. xxx, no. xx, pp. 545–556, 2007.
- [3] A. Bahrami, H. Mahjub, M. Sadeghian, and F. Golbabaeei, "Determination of Benzene , Toluene and Xylene (BTX) Concentrations in Air Using HPLC Developed Method Compared to Gas Chromatography," *Int. J. Occup. Hyg.*, vol. 3, no. July 2016, pp. 12–17, 2011.
- [4] T. Higashiyama, "Novel functions and applications of trehalose," *Pure Appl. Chem.*, vol. 74, no. 7, pp. 1263–1269, 2002.
- [5] M. Etzel, "Alternatives to Chromatographic Separations," pp. 42–45, 2007.
- [6] S. D. Schaber, D. I. Gerogiorgis, R. Ramachandran, J. M. B. Evans, P. I. Barton, and B. L. Trout, "Economic analysis of integrated continuous and batch pharmaceutical manufacturing: A case study," *Ind. Eng. Chem. Res.*, vol. 50, no. 17, pp. 10083–10092, 2011.
- [7] P. Z. Andrea Adamo, Rachel L. Beingessner, Mohsen Behnam, Jie Chen, Timothy F. Jamison, Klavs F. Jensen, Jean-Christophe M. Monbaliu, Allan S. Myerson, Eve M. Revalor, David R. Snead, Torsten Stelzer, Nopphon Weeranoppanant, Shin Yee Wong, "On-demand continous-flow production of pharmaceuticals in a compact reconfigurable system," *J. Chem. Inf. Model.*, vol. 53, no. 9, pp. 1689–1699, 2013.
- [8] K. Raza, "Polymorphism: The Phenomenon Affecting the Performance of Drugs," *SOJ Pharm. Pharm. Sci.*, vol. 1, no. 2, 2014.

- [9] B. Wood, K. P. Girard, C. S. Polster, and D. M. Croker, "Progress to Date in the Design and Operation of Continuous Crystallization Processes for Pharmaceutical Applications," *Org. Process Res. Dev.*, vol. 23, pp. 122–144, 2019.
- [10] G. D. Wang, F. P. Mallet, F. Ricard, and J. Y. Y. Heng, "Pharmaceutical nanocrystals," *Curr. Opin. Chem. Eng.*, vol. 1, no. 2, pp. 102–107, 2012.
- [11] P. Sheehan *et al.*, "Kilogram-scale prexasertib monolactate monohydrate synthesis under continuous-flow CGMP conditions," *Science (80-.)*, vol. 356, no. 6343, pp. 1144–1150, 2017.
- [12] S. Lawton, G. Steele, P. Shering, L. Zhao, I. Laird, and X. W. Ni, "Continuous crystallization of pharmaceuticals using a continuous oscillatory baffled crystallizer," *Org. Process Res. Dev.*, vol. 13, no. 6, pp. 1357–1363, 2009.
- [13] X. Ni and A. Liao, "Effects of mixing, seeding, material of baffles and final temperature on solution crystallization of l-glutamic acid in an oscillatory baffled crystallizer," *Chem. Eng. J.*, vol. 156, no. 1, pp. 226–233, 2010.
- [14] J. Huuskonen, M. Salo, and J. Taskinen, "Aqueous solubility prediction of drugs based on molecular topology and neural network modeling.," *J. Chem. Inf. Comput. Sci.*, vol. 38, no. 3, pp. 450–6, 1998.
- [15] Z. K. Nagy, "Model based robust control approach for batch crystallization product design," *Comput. Chem. Eng.*, vol. 33, no. 10, pp. 1685–1691, 2009.
- [16] N. E. B. Briggs, U. Schacht, V. Raval, T. McGlone, J. Sefcik, and A. J. Florence, "Seeded Crystallization of β - L -Glutamic Acid in a Continuous Oscillatory Baffled Crystallizer," *Org. Process Res. Dev.*, vol. 19, no. 12, pp. 1903–1911, 2015.

- [17] A. Koswara and Z. K. Nagy, "Spatio-Temporal Anti-Fouling Control of Plug-Flow Crystallization - Part I of II : Case Studies and Open-Loop Control."
- [18] E. H. Lee, "A practical guide to pharmaceutical polymorph screening & selection," *Asian J. Pharm. Sci.*, vol. 9, no. 4, pp. 163–175, 2014.
- [19] N. Choudhury and S. L. Chaplot, "Free energy and relative stability of the enstatite Mg₂Si₂O₆ polymorphs," *Solid State Commun.*, vol. 114, no. 3, pp. 127–132, 2000.
- [20] M. J. Hageman, "The role of moisture in protein stability," *Drug Dev. Ind. Pharm.*, vol. 14, no. 14, pp. 2047–2070, 1988.
- [21] J. Chen, B. Sarma, J. M. B. Evans, and A. S. Myerson, "Pharmaceutical crystallization," *Cryst. Growth Des.*, vol. 11, no. 4, pp. 887–895, 2011.
- [22] M. Birch, S. J. Fussell, P. D. Higginson, N. McDowall, and I. Marziano, "Towards a PAT-based strategy for crystallization development," *Org. Process Res. Dev.*, vol. 9, no. 3, pp. 360–364, 2005.
- [23] J. Star Research, "API crystallization and formulation for today's drug development needs," *c&en WHITEPAPERS*, 2019.
- [24] J. Litster, *Design and Processing of Particulate Products*. 2016.
- [25] A. D. Randolph and E. T. White, "Modeling size dispersion in the prediction of crystal-size distribution," *Chem. Eng. Sci.*, vol. 32, no. 9, pp. 1067–1076, 1977.
- [26] M. R. A. Bakar *et al.*, "The Impact of Direct Nucleation Control on Crystal Size Distribution in Pharmaceutical Crystallization Processes The Impact of Direct Nucleation Control on Crystal Size Distribution in Pharmaceutical Crystallization Processes XXXX," pp. 3–9, 2008.

- [27] A. N. Saleemi, C. D. Rielly, and Z. K. Nagy, “Comparative investigation of supersaturation and automated direct nucleation control of crystal size distributions using ATR-UV/vis spectroscopy and FBRM,” *Cryst. Growth Des.*, vol. 12, no. 4, pp. 1792–1807, 2012.
- [28] S. S. Kadam, H. J. M. Kramer, and J. H. Ter Horst, “Combination of a single primary nucleation event and secondary nucleation in crystallization processes,” *Cryst. Growth Des.*, vol. 11, no. 4, pp. 1271–1277, 2011.
- [29] C. J. Callahan and X.-W. Ni, “An investigation into the effect of mixing on the secondary nucleation of sodium chlorate in a stirred tank and an oscillatory baffled crystallizer,” *CrystEngComm*, vol. 16, no. 4, p. 690, 2014.
- [30] L. Goh *et al.*, “A stochastic model for nucleation kinetics determination in droplet-based microfluidic systems,” *Cryst. Growth Des.*, vol. 10, no. 6, pp. 2515–2521, 2010.
- [31] R. D. Braatz, “Advanced control of crystallization processes,” *Annu. Rev. Control*, vol. 26 I, pp. 87–99, 2002.
- [32] A. J. Florence, “Development of Continuous Crystallizations in an Oscillatory Baffled Reactor,” no. June. EPSRC: Centre for Innovative Manufacturing in Continuous Manufacturing and Crystallisation, 2013.
- [33] R. Peña, J. A. Oliva, C. L. Burcham, D. J. Jarmer, and Z. K. Nagy, “Process Intensification through Continuous Spherical Crystallization Using an Oscillatory Flow Baffled Crystallizer,” 2017.
- [34] C. J. Brown and X. Ni, “Online evaluation of paracetamol antisolvent crystallization growth rate with video imaging in an oscillatory baffled crystallizer,” *Cryst. Growth Des.*, vol. 11, no. 3, pp. 719–725, 2011.

- [35] P. Bennema, "The importance of surface diffusion for crystal growth from solution," *J. Cryst. Growth*, vol. 5, pp. 29–43, 1969.
- [36] A. Llinàs and J. M. Goodman, "Polymorph control: past, present and future," *Drug Discov. Today*, vol. 13, no. 5–6, pp. 198–210, 2008.
- [37] N. E. Pereira and X. Ni, "Droplet size distribution in a continuous oscillatory batch reactor," vol. 56, pp. 735–739, 2001.
- [38] A. H. L. Chow and M. W. M. Leung, "A study of the Mechanisms of Wet Spherical Agglomeration of Pharmaceutical Powders," *Drug Dev. Ind. Pharm.*, vol. 22, no. 4, pp. 357–371, 1996.
- [39] A. F. Blandin, D. Mangin, A. Rivoire, J. P. Klein, and J. M. Bossoutrot, "Agglomeration in suspension of salicylic acid fine particles: Influence of some process parameters on kinetics and agglomerate final size," *Powder Technol.*, vol. 130, no. 1–3, pp. 316–323, 2003.
- [40] R. Peña and Z. K. Nagy, "Process Intensification through Continuous Spherical Crystallization Using a Two-Stage Mixed Suspension Mixed Product Removal (MSMPR) System," *Cryst. Growth Des.*, vol. 15, no. 9, pp. 4225–4236, 2015.
- [41] K. B. Smith, "The Scale-Up of Oscillatory Flow Mixing," *PhD Thesis, Univ. Cambridge*, no. September, 1999.
- [42] J. A. Gavira, "Current trends in protein crystallization," *Arch. Biochem. Biophys.*, vol. 602, pp. 3–11, 2016.
- [43] N. Sanzida and Z. K. Nagy, "Iterative learning control for the systematic design of supersaturation controlled batch cooling crystallisation processes," *Comput. Chem. Eng.*, vol. 59, pp. 111–121, 2013.

- [44] Z. K. Nagy and R. D. Braatz, "Advances and New Directions in Crystallization Control," *Annu. Rev. Chem. Biomol. Eng.*, vol. 3, no. 1, pp. 55–75, 2012.
- [45] J. Worlitschek and M. Mazzotti, "Model-based optimization of particle size distribution in batch-cooling crystallization of paracetamol," *Cryst. Growth Des.*, vol. 4, no. 5, pp. 891–903, 2004.
- [46] N. Kubota, N. Doki, M. Yokota, and A. Sato, "Seeding policy in batch cooling crystallization," *Powder Technol.*, vol. 121, no. 1, pp. 31–38, 2001.
- [47] N. Doki, N. Kubota, A. Sato, and M. Yokota, "Effect of cooling mode on product crystal size in seeded batch crystallization of potassium alum," *Chem. Eng. J.*, vol. 81, no. 1–3, pp. 313–316, 2001.
- [48] S. Mahanty, J. Sruti, C. N. Patra, and M. E. B. Rao, "Particle Design of Drugs by Spherical Crystallization Techniques," *Int. J. Pharm. Sci. Nanotechnol.*, vol. 3, no. 2, pp. 912–918, 2010.
- [49] K. Plumb, "Continuous Processing in the Pharmaceutical Industry," *Chem. Eng. Res. Des.*, vol. 83, no. June, pp. 730–738, 2005.
- [50] X. Ni, H. Jian, and a. . Fitch, "Computational fluid dynamic modelling of flow patterns in an oscillatory baffled column," *Chem. Eng. Sci.*, vol. 57, pp. 2849–2862, 2002.
- [51] X. Ni, M. R. Mackley, A. P. Harvey, P. Stonestreet, M. H. I. Baird, and N. V. Rama Rao, "Mixing Through Oscillations and Pulsations—A Guide to Achieving Process Enhancements in the Chemical and Process Industries," *Chem. Eng. Res. Des.*, vol. 81, no. 3, pp. 373–383, 2003.
- [52] C. R. Brunold, J. C. B. Hunns, M. R. MACKLEY, and J. W. THOMPSON, "Losses for Oscillatory," *Chem. Eng. Sci.*, vol. 44, no. 5, pp. 1227–1244, 1989.

- [53] C. N. Nanev, "On the slow kinetics of protein crystallization," *Cryst. Growth Des.*, vol. 7, no. 8, pp. 1533–1540, 2007.
- [54] M. R. Mackley and P. Stonestreet, "Heat transfer and associated energy dissipation for oscillatory flow in baffled tubes," *Chem. Eng. Sci.*, vol. 50, no. 14, pp. 2211–2224, 1995.
- [55] P. Stonestreet and A. P. Harvey, "A Mixing-Based Design Methodology for Continuous Oscillatory Flow Reactors," *Chem. Eng. Res. Des.*, vol. 80, no. January, pp. 31–44, 2002.
- [56] I. I. Onyemelukwe, B. Benyahia, N. M. Reis, Z. K. Nagy, and D. Chris, "The heat transfer characteristics of a mesoscale continuous oscillatory flow crystalliser with smooth periodic constrictions," pp. 1–33.
- [57] A. P. Harvey, M. R. Mackley, N. Reis, J. A. Teixeira, and A. A. Vicente, "The Fluid Mechanics Relating to a Novel Oscillatory Flow Micro Reactor," *4th Eur. Congr. Chem. Eng.*, pp. 0-6.4-004, 2003.
- [58] R. Kacker, S. I. Regensburg, and H. J. M. Kramer, "Residence time distribution of dispersed liquid and solid phase in a continuous oscillatory flow baffled crystallizer," *Chem. Eng. J.*, vol. 317, pp. 413–423, 2017.
- [59] K. Tahara, M. O'Mahony, and A. S. Myerson, "Continuous spherical crystallization of albuterol sulfate with solvent recycle system," *Cryst. Growth Des.*, vol. 15, no. 10, pp. 5155–5156, 2015.
- [60] a R. Paradkar, a P. Pawar, J. K. Chordiya, V. B. Patil, and a R. Ketkar, "Spherical crystallization of celecoxib.," *Drug Dev. Ind. Pharm.*, vol. 28, no. 10, pp. 1213–20, 2002.

- [61] Y. Kawashima, F. Cui, H. Takeuchi, T. Niwa, T. Hino, and K. Kiuchi, "Parameters determining the agglomeration behaviour and the micromeritic properties of spherically agglomerated crystals prepared by the spherical crystallization technique with miscible solvent systems," *Int. J. Pharm.*, vol. 119, no. 2, pp. 139–147, 1995.
- [62] A. I. Toldy *et al.*, "Spherical crystallization of glycine from monodisperse microfluidic emulsions," *Cryst. Growth Des.*, vol. 12, no. 8, pp. 3977–3982, 2012.
- [63] Y. Kawashima, Y. Kurachi, and H. Takenaka, "Preparation of spherical wax matrices of sulfamethoxazole by wet spherical agglomeration technique using a CMSMPR agglomerator," *Powder Technol.*, vol. 32, no. 2, pp. 155–161, 1982.
- [64] A. Sano, T. Kuriki, Y. Kawashima, H. Takeuchi, T. Hino, and T. Niwa, "Particle Design of Tolbutamide by the Spherical Crystallization Technique," *Chem. Pharm. Bull.*, vol. 40, no. 11, pp. 3030–3035, 1992.
- [65] N. Reis, A. A. Vicente, J. A. Teixeira, and M. R. Mackley, "Residence times and mixing of a novel continuous oscillatory flow screening reactor," *Chem. Eng. Sci.*, vol. 59, no. 22–23, pp. 4967–4974, 2004.
- [66] J. A. Moulijn and A. Stankiewicz, "Process Intensification," *Encycl. Sustain. Technol.*, pp. 509–518, 2017.
- [67] J. R. McDonough, A. N. Phan, and A. P. Harvey, "Rapid process development using oscillatory baffled mesoreactors - A state-of-the-art review," *Chem. Eng. J.*, vol. 265, no. 1, pp. 110–121, 2015.
- [68] A. N. Phan and A. P. Harvey, "Characterisation of mesoscale oscillatory helical baffled reactor-Experimental approach," *Chem. Eng. J.*, vol. 180, pp. 229–236, 2012.

- [69] X. W. Ni, A. Valentine, A. Liao, S. B. C. Sermage, G. B. Thomson, and K. J. Roberts, "On the crystal polymorphic forms of L-glutamic acid following temperature programmed crystallization in a batch oscillatory baffled crystallizer," *Cryst. Growth Des.*, vol. 4, no. 6, pp. 1129–1135, 2004.
- [70] M. S. R. Abbott, A. P. Harvey, G. V. Perez, and M. K. Theodorou, "Biological processing in oscillatory baffled reactors: operation, advantages and potential.," *Interface Focus*, vol. 3, no. 1, p. 20120036, 2013.
- [71] X. Ni, G. Brogan, A. Struthers, D. C. Bennett, and S. F. Wilson, "A systematic study of the effect of geometrical parameters on mixing time in oscillatory baffled columns," *Chem. Eng. Res. Des.*, vol. 76, no. A5, pp. 635–642, 1998.
- [72] P. Gough, X. Ni, and K. C. Symes, "Experimental flow visualisation in a modified pulsed baffled reactor," *J. Chem. Technol. Biotechnol.*, vol. 69, no. 3, pp. 321–328, 1997.
- [73] A. N. Phan, A. P. Harvey, and M. Rawcliffe, "Continuous screening of base-catalysed biodiesel production using New designs of mesoscale oscillatory baffled reactors," *Fuel Process. Technol.*, vol. 92, no. 8, pp. 1560–1567, 2011.

3. EXPERIMENTAL INVESTIGATION OF THE EFFECT OF SCALE-UP ON MIXING EFFICIENCY IN OSCILLATORY FLOW BAFFLED REACTORS (OFBR) USING PRINCIPAL COMPONENT-BASED IMAGE ANALYSIS AS A NOVEL NONINVASIVE RESIDENCE TIME DISTRIBUTION MEASUREMENT APPROACH

Reproduced with permission from Joseph A. Oliva*, Kanjakha Pal*, Alastair Barton**, Paul Firth**, and Zoltan K. Nagy*. *Chemical Engineering Journal*, 351, 498-505. Copyright 2018 Elsevier.

*School of Chemical Engineering, Purdue University, West Lafayette, IN 47907, US

**Alconbury Weston Ltd, Stoke-on-Trent, ST4 3PE, United Kingdom

3.1 Abstract

Oscillatory flow strategies through baffled tubular reactors provide an efficient approach in improving process kinetics through enhanced micromixing and heat transfer. Known to have high surface area to volume ratios, oscillatory flow baffled reactors (OFBR) generate turbulence by superimposing piston driven oscillatory flow onto the net flow generated by a pump. By tuning the oscillating parameters (amplitude and frequency), one can tailor the residence time distribution of the system for a variety of multiphase applications. Using a microscope camera, principal component image analysis, and pulse tracer injections, a novel noncontact approach has been developed to experimentally estimate dispersion coefficients in two geometrically different systems (DN6 and DN15, Alconbury Weston Ltd.). The paper also introduces for the first time a novel scaled-down version of the commercially available DN15 OFBR, the DN6 (about 10 times smaller scale), and provides a comprehensive experimental investigation of the effect of oscillation parameters on the residence time distributions (RTD) in both systems. The oscillation

amplitude was found to have a significant positive correlation with the dispersion coefficient with 1 mm providing the least amount of dispersion in either system. Oscillation frequency had a less significant impact on the dispersion coefficient, but optimal operation was found to occur at 1.5 Hz for the DN6 and 1.0Hz for the DN15. Until now, OFBR literature has not distinguished between piston and pump driven flow. Pump driven flow was found to be ideal for both systems as it minimizes the measured dispersion coefficient. However, piston driven turbulence is essential for avoiding particle settling in two phase (solid-liquid) systems and should be considered in applications like crystallization.

Keywords: residence time distribution, oscillatory flow, continuous reactions

3.2 Introduction

Increasingly popular for both synthesis and purification applications, continuous oscillatory flow strategies improve process kinetics through enhanced micromixing and heat transfer characteristics.^[1] Specifically useful for dual phase systems (liquid- liquid/ solid- liquid), oscillatory flow baffled reactors (OFBR) offer process flexibility with adaptable configurations. OFBRs are often divided into several zones which allow for the implementation of temperature profiles and the spatial distribution of reagents across multiple injection points^[1]. These added degrees of freedom provide numerous design advantages when compared to their continuous stirred tank counterparts.

Compared to traditional plug flow reactors (PFRs), OFBRs generate turbulence by superimposing an oscillatory flow onto the net flow through the use of a piston. By imposing this oscillatory turbulence, OFBRs do not need to operate at high throughput flow rates like PFRs, meaning smaller tube lengths and holdup volumes. However, several authors have indicated that these oscillations have a significant impact on the RTD of the system,^{[2],[4],[5],[6]} but do not

consider system geometry or scale up. Herein, two commercial systems of different geometry and scale will be evaluated under a variety of operating conditions.

| OFBR Model | D (mm) | d_o (mm) | l_b (mm) | Glass Thickness (mm) | Volume (mL) |
|------------|--------|------------|------------|----------------------|-------------|
| DN6 | 6.85 | 3.5 | 11 | 3 | 37.5 |
| DN15 | 15 | 7.5 | 21.4 | 2 | 312.5 |

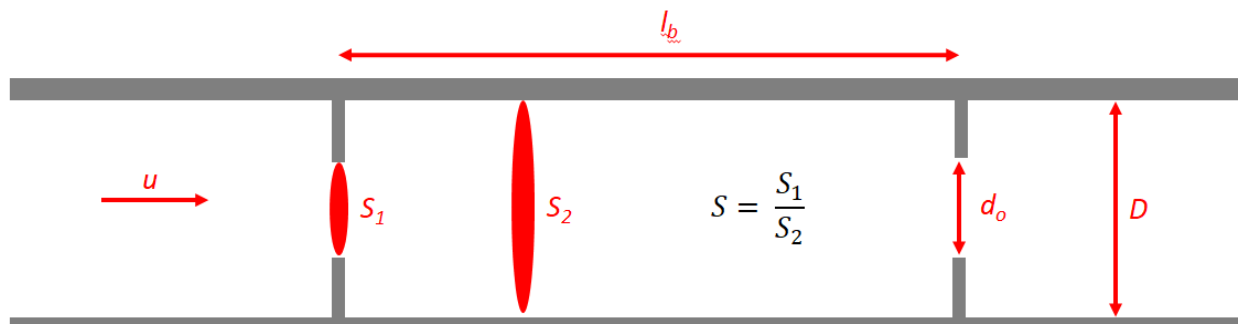


Figure 3.1 Illustration of OFBR geometry, adapted from McDonough⁷

Conventional oscillatory baffled reactors vary in geometry and have diameters of 15 mm or greater,^[7] while the newer (more recent) mesoscale reactors have diameters in the range of 4-5 mm. Regardless of scale, the commercial application of oscillatory systems are generally limited to purely liquid systems, as plug flow operation in a two phase (solid/liquid) system is still mainly a topic of interest amongst academics, especially for shear-sensitive applications.^[8]

The flow characteristics in oscillatory systems are largely governed by both operating and geometric parameters.^[9] As described in Figure 3.1, S controls the size and shape of eddies formed, while adequate distance between baffles (l_b) ensures fully developed vortices and the minimization of mixing dead zones.^{[10],[11]} Baffle type also plays a major role and should be chosen appropriately for a given application. For example, a major concern in designing crystallization systems is minimizing shear stress, as it can lead to crystal breakage and broad size distributions.^[12] Integral baffles (like those in the DN6 and DN15) provide a low shear

environment^{[13],[14]} by smoothly constricting the inner diameter of the tube periodically, making them ideal for these applications.

Four dimensionless parameters define the fluid flow patterns in an OBC, that is, the oscillatory Reynolds number (Re_o), the net flow Reynolds number (Re_n), the Strouhal number (St), and ψ , the ratio of oscillatory and net flows.

$$Re_o = \frac{2\pi f x_0 \rho D}{\mu} \quad (1)$$

$$Re_n = \frac{\rho u D}{\mu} \quad (2)$$

$$St = \frac{D}{4\pi x_0} \quad (3)$$

$$\psi = \frac{Re_o}{Re_n} \quad (4)$$

Note: x_0 is the piston amplitude, ρ is the solution density, D is the diameter of the tube segment, u is the mean superficial velocity and μ is the solution viscosity. The St measures effective eddy propagation by simply taking the ratio of the column diameter to piston stroke length^[6]. The Re_o represents the turbulence generated by the oscillating piston. Similar to traditional fluid dynamics, the Re_n is a ratio of inertial to viscous forces. The ratio of oscillatory and net flow Re result in the overall mixing parameter ψ , a commonly used turbulence parameter.

3.2.1 Residence Time Distributions in Oscillatory Baffled Systems

Table 3-1 Optimum operating parameters of OFBRs in literature

| System | DN15 | Custom | Custom | Amicon-Wright |
|--------------------------------|---|---|---|--|
| Length (m) | ~5 | 5 | 20.5 | 0.67 |
| Inner Diameter (mm) | 15 | 25 | 40 | 23 |
| Vertical (V) or Horizontal (H) | V | V | V | H |
| Re_o | 94-3,000 | 435 | 2008 | Not reported |
| Optimal Frequency (Hz) | Both high (5) and low (1) | Not reported | 2 | No effect |
| Optimal Amplitude (mm) | 1 | Not reported | 4 | 1 |
| Conclusions | Ψ is not sufficient in characterizing a system | Scale up can be achieved using a multi-tube configuration | Increasing x_0 led to increasing dispersion | Frequency had an insignificant effect on dispersion measurements |
| Author | Kacker ^[4] | Ni ^[15] | Pereira ^[6] | Dickens ^[16] |

A major advantage in oscillatory tubular systems is the ability to operate near plug flow for narrow residence time distributions^[17]. As seen in Table 3-1, several authors have worked to develop the operating framework for continuous oscillatory baffled systems. Each had a geometrically different system, but the trends for optimal operation are similar. Kacker's work used the commercially available DN15 manufactured by Alconbury Weston Ltd. He found that Ψ is not a sufficient parameter in characterizing the fluid dynamics of their system and that optimal operation occurred at both high and low frequencies as long as the amplitude remained small (1 mm). Similarly, Dickens reported the same optimal amplitude of oscillation and that frequency had little to no effect on dispersion measurements. Moreover, both Kacker's and Dickens' results agree with those conducted by Pereira, who showed that increasing the amplitude of oscillation resulted in increased dispersion and a larger mean residence time. Ni

used flow visualization studies to evaluate the benefits of both baffles and oscillations in achieving plug flow behavior at minimal flow rates (Re_N). Plug flow operation is vital for crystallization, as narrow CSDs are directly proportional to narrow RTDs. Moreover, the majority of RTDs in OFBR literature are conducted for single phase liquid systems, which do not accurately represent solid-liquid systems. Kacker, however, performed both liquid and solid-liquid RTD studies and showed that plug flow operation is achievable under a variety of conditions.

3.2.2 Mean Residence Time and Dispersion Calculations

To evaluate the residence time distributions at different flow conditions, both mean residence time and dispersion calculations are often used:^{[4],[5]}

$$t_{mean} = \frac{\int_0^{\infty} t \cdot c \, dt}{\int_0^{\infty} c \, dt} \quad (5)$$

$$\sigma^2 = \frac{\int_0^{\infty} (t - t_{mean})^2 \cdot c \, dt}{\int_0^{\infty} c \, dt} \quad (6)$$

$$\frac{\sigma^2}{t_{mean}^2} = 2 \left(\frac{\mathcal{D}}{uL} \right) + 8 \left(\frac{\mathcal{D}}{uL} \right)^2 \quad (7)$$

where t is time (s), c is the concentration (mg/mL), σ is the variance, \mathcal{D} (m^2/s) is the dispersion coefficient, u (m/s) is the net flow superficial velocity, and L (m) is the distance between the tracer's injection point and the point at which the concentration measurement is taken. While equations (5) and (6) are standard in the RTD literature, Levenspiel^[18] solved the dispersion model subject to the open-open boundary condition to obtain the analytical solution found in equation (7). Using this method, Kacker experimentally determined $\mathcal{D}/(uL)$ values for the

commercially available DN15 to be on the order of 10^{-2} . These results should be independent of scale, as equations (5) – (7) are independent of geometrical considerations.

One limitation of the proposed approach in determining the dispersion coefficient is that equations (5) and (6) only consider the area under the concentration versus time curve, while information regarding the shape of the curve is lost. To better consider this lumped information, an asymmetry factor was introduced.

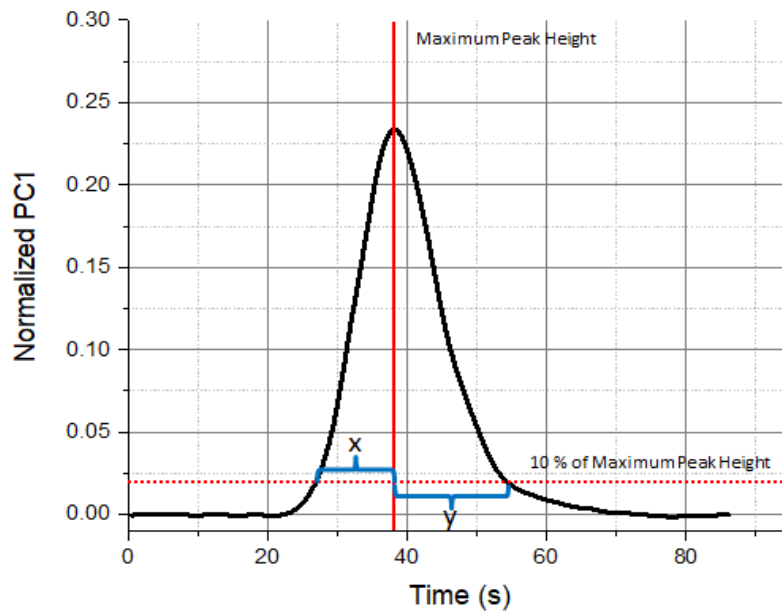


Figure 3.2 Illustration of asymmetry factor calculation

$$\text{Asymmetry Factor} = \frac{y}{x} \quad (8)$$

Typically used to describe qualitative information in chromatographs,^[19] the asymmetry factor provides an additional means of comparing RTDs under different process conditions. Peak “tailing” is not adequately described by dispersion calculations because the area under the peak tail is rather small. Asymmetry factors close to 1 indicate minimal peak tailing, while factors much larger than 1 give insight regarding the amount of back mixing (tracer spreading in the

reverse direction) caused by piston drawback. All in all, the asymmetry factor is a supplementary tool that should be used in combination with the dispersion coefficient to evaluate overall system performance.

3.2.3 Principal Component Image Analysis (PCA)

Principal component transformations are an advanced technique that reduces the dimensionality of a dataset, such that correlations found within the data are measured as a maximization of uncorrelated variations.^{[20],[21]} Specific to image analysis applications, PCA is a linear orthogonal transformation that converts traditional RGB measurement space to PC1-PC3 space. PC1 is a maximization of the statistical variance (σ) in the RGB data set. Each subsequent PC also maximizes the statistical variance, subject to the constraint that it is orthogonal to the previous principal components. In this way, the signal is largely captured in PC1 and is weaker with each additional principal component. The utility of this approach is that a single measurement can be tracked with time (PC1) and is directly proportional to the concentration of tracer in the system. This technique is often used to define a new basis set of vectors (viz. the first three principal components) and has many commercial applications.

In regards to the following residence time distribution studies, PCA is used to identify the presence of methylene blue as a pulse tracer. Although nontraditional for this application, this technique has novel capabilities compared to traditional concentration measurements with UV probes. In this oscillatory system, probe-based measurement ports can only be located at the elbow/tube junctions in order to avoid interference with the baffles. However, the dispersion term in the elbow is likely different than that found in the tube segment, creating a parameter mismatch at the point of measurement.^[22] In using a microscope camera measurement, with PCA

image analysis, a novel approach was developed that measures RTDs and dispersion coefficients at different geometrical locations without direct contact in the system.

Simply using RGB camera measurements without the processing of PCA is ineffective at determining RTDs, since the proportionality of G/B changes nonlinearly with the concentration seen by the camera. In other words, a difficult calibration is required to correlate RGB intensity measurements with methylene blue concentrations. Grayscale video processing is a potential RGB alternative for RTD measurements. Although appropriate for OFBR RTD studies, grayscale video processing is sensitive to process lighting conditions and camera positioning. PCA, however, measures uncorrelated variations in the dataset, which is independent of the absolute intensity measured by the camera. That is, if the unprocessed measurements from an experiment fall in the upper range of the 256 bit scale on one day but fall in a lower range on a different day, the two experiments can still be compared because the first principal component measurements are with respect to changes in the statistical variance and not the absolute measurement! Therefore, by tracking changes in variance instead of changes in the true measurement, PCA is a more robust and appropriate processing method.

3.3 Materials and Methods

3.3.1 Residence Time Distribution Studies

The first set of experiments implemented the newly designed Nitech DN6 (Alconbury Weston Ltd) OFBR with a total holdup volume of 37.5 mL distributed across 2 equal tube segments and a single elbow connection, while the second set utilized a Nitech DN15 (Alconbury Weston Ltd) with a holdup of 312.5 mL (roughly one order of magnitude difference in scale). Methylene blue (Lab grade $\geq 99.5\%$ purity, Fisher Scientific) was injected as a pulse tracer (380 $\mu\text{g}/\text{mL}$) using a syringe pump (kd Scientific, Infusion). Water was pumped at the

inlet using a peristaltic pump (MasterFlex L/S, Cole-Palmer) at varying flow rates. The entire system was jacketed and held at 25 °C for the duration of the experiment. A Firefly Pro microscope camera (RW180) was used to record video images at 720×480 resolution at 15 fps.

In order to relate the DN6 system parameters with the DN15, several decisions were made regarding the injection volume of methylene blue and the flow rate of the bulk fluid (water). Using the cross sectional area of the DN6 and a set water flow rate of 15 mL/min, an estimated axial velocity was determined. This estimated axial velocity was kept constant and was directly translated to the DN15 and the equivalent water flow rate was determined to be 154.7 mL/min. In regards to the pulse tracer injection, the original intention was to scale the methylene blue volume with the total holdup of each system. However, due to limitations on the injection speed of the syringe pump (max 52 mL/min), it was determined that the larger volume required for the DN15 could not be injected at a quick enough rate to be considered instantaneous. As a result, the injection speed between the systems was kept constant and the maximum injection volume for that speed was used in the DN15 experiments. The final injection parameters are as follows: 0.2 mL at 40 mL/min for the DN6 and 0.25 mL at 50 mL/min for the DN15.

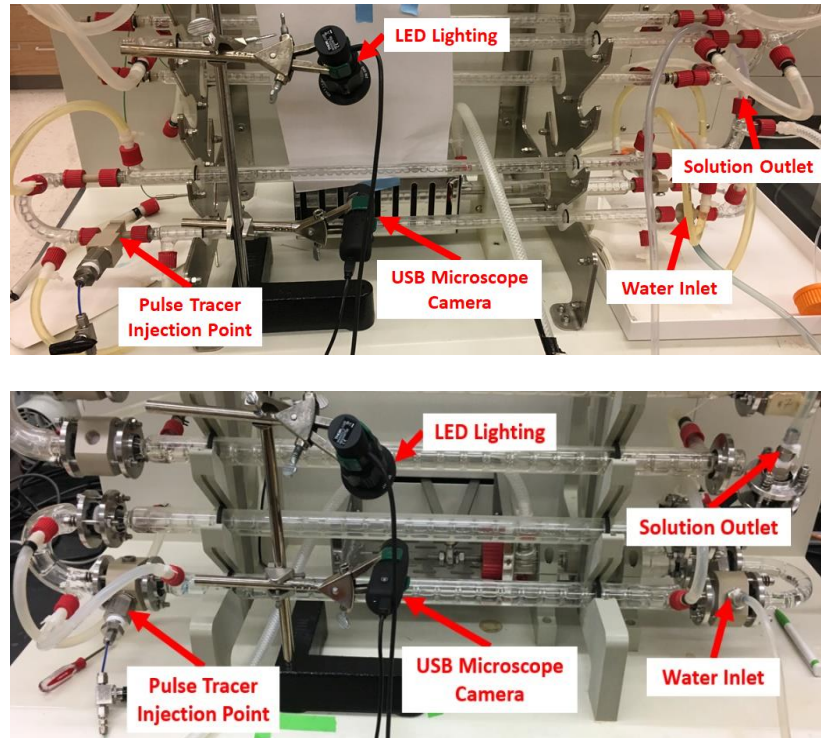


Figure 3.3 Pictures with main components of the DN6 (top) and DN15 (bottom) RTD experimental setup

3.3.2 Principal Component Image Analysis

Prior to the application of PCA, the dataset is averaged to 1 fps in order to reduce noise in the RGB intensity measurements. Moreover, this technique helps to maximize the variations found in PC1 by avoiding large noise spikes that result from air travelling through the system. The goal of this approach is to completely capture the variations of the system in PC1 instead of a combination of all three PCs. The developed Matlab software identifies the initial pulse tracer by taking the derivative of the first principal component. When the derivative of the first component exceeds a sufficiently large value, the software checks subsequent local points to ensure pulse tracer detection. This approach limits noisy data and ensures proper pulse tracer detection limits. The end detection limit utilizes a baseline averaging technique. A baseline is defined as an average of the final 25% of data points. When the principal component measurement crosses this baseline, an endpoint limit is defined. Herein, the width of the RTD is

defined as the difference in time between the initial tracer pulse detection limit and the endpoint tracer limit. To normalize the distribution, a min-max difference is used.

$$PC1_{max} = \max^{90} \left\{ \begin{pmatrix} PC1_{1,1} & \cdots & PC1_{1,m} \\ \vdots & \ddots & \vdots \\ PC1_{n,1} & \cdots & PC1_{n,m} \end{pmatrix} \right\} \quad (9)$$

$$PC1_{min} = \min^{10} \left\{ \begin{pmatrix} PC1_{1,1} & \cdots & PC1_{1,m} \\ \vdots & \ddots & \vdots \\ PC1_{n,1} & \cdots & PC1_{n,m} \end{pmatrix} \right\} \quad (10)$$

$$Normalized\ PC1 = \frac{PC1_{max} - PC1_{min}}{PC1_{max}} \quad (11)$$

That is, the 90th percentile (90% of the data falls below this point) is used as the max while the 10th percentile is used as the min. The difference between the max and min is taken and divided by the max for each frame. Note that this is the approach used to reduce the two-dimensional data matrix measured for each frame to a single scalar value. Herein, these are the scalar values tracked with time and reported in the RTD results section.

3.3.3 Limits of Detection using PCA and Methylene Blue

In using a non-contact microscope camera instead of a UV-vis probe for concentration measurements, the limit of detection may come into question as it relates to the accuracy of the dispersion coefficient calculations. To measure the limit of detection, a series of step changes were implemented before reaching a controlled state of operation. In other words, several known concentrations of methylene blue were pumped through the inlet and held for several minutes before the subsequent step change was implemented. Firstly, water was introduced to the system, followed by dilute methylene blue at 0.95 μM , 0.71 μM , 0.48 μM , 0.24 μM , and 0.12 μM , respectively. When the measure of principal component 2 dips below that measured for water,

the limit of detection is reached. Note that PC2 is used here instead of PC1 because at this dilution, the variations measured in PC1 for each concentration are very similar to that of water. However, the subtle variations in the dataset are completely captured by PC2. Using the aforementioned method, the limit of detection was determined to be 0.24 μM , thus validating the use of a microscope camera and PCA as an RTD measurement approach.

3.4 Results and Discussion

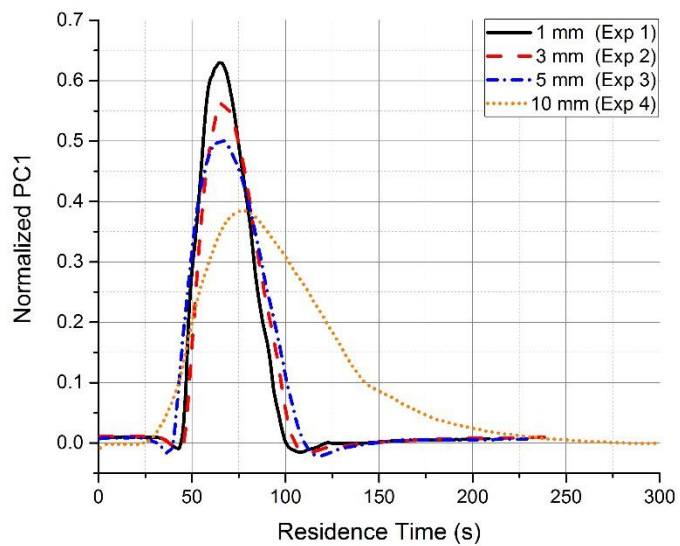
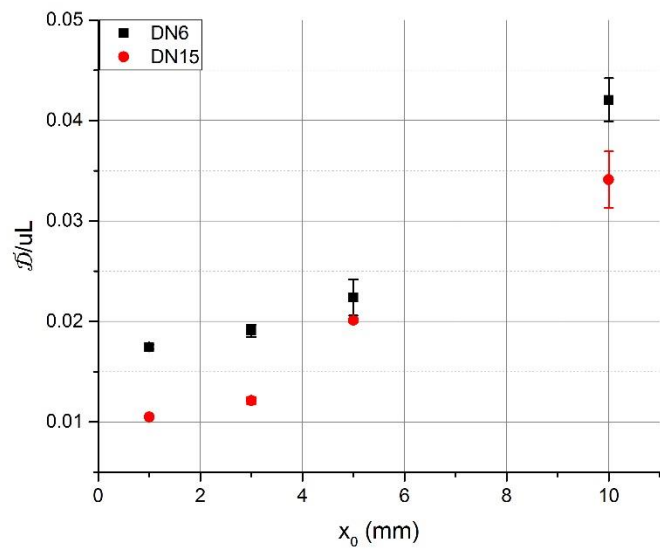
3.4.1 Summary of Experimental Conditions

Table 3-2 DN6 (top) and DN15 (bottom) RTD experiments and dispersion calculation results

| Exp. | Flow Rate (mL/min) | x_0 (mm) | f (Hz) | Re_o | Ψ | Asymmetry Factor | $\frac{\delta}{uL}$ |
|------|-----------------------|---------------|----------|--------|--------|---------------------|---------------------|
| 1 | 15 | 1 | 1 | 48.2 | 0.9 | 1.6 | 0.017 |
| 2 | 15 | 3 | 1 | 144.6 | 2.8 | 1.7 | 0.019 |
| 3 | 15 | 5 | 1 | 241.1 | 4.6 | 1.6 | 0.022 |
| 4 | 15 | 10 | 1 | 482.2 | 9.3 | 2.0 | 0.042 |
| 5 | 15 | 1 | 0.2 | 9.6 | 0.2 | 1.9 | 0.027 |
| 6 | 15 | 1 | 1.5 | 72.3 | 1.4 | 1.4 | 0.015 |
| 7 | 15 | 1 | 3 | 144.6 | 2.8 | 1.8 | 0.034 |
| 8 | 10 | 1 | 1 | 48.2 | 1.4 | 2.2 | 0.023 |
| 9 | 30 | 1 | 1 | 48.2 | 0.5 | 2.5 | 0.014 |

| Exp. | Flow Rate (mL/min) | x_0 (mm) | f (Hz) | Re_o | Ψ | Asymmetry Factor | $\frac{\delta}{uL}$ |
|------|-----------------------|------------|----------|--------|--------|---------------------|---------------------|
| 1 | 154.7 | 1 | 1 | 112.6 | 0.5 | 1.5 | 0.010 |
| 2 | 154.7 | 3 | 1 | 337.9 | 1.5 | 1.4 | 0.012 |
| 3 | 154.7 | 5 | 1 | 563.1 | 2.4 | 1.5 | 0.020 |
| 4 | 154.7 | 10 | 1 | 1126.2 | 4.9 | 2.0 | 0.034 |
| 5 | 154.7 | 1 | 0.2 | 168.9 | 0.7 | 1.4 | 0.015 |
| 6 | 154.7 | 1 | 1.5 | 337.9 | 1.5 | 2.2 | 0.023 |
| 7 | 154.7 | 1 | 3 | 22.5 | 0.1 | 1.6 | 0.014 |
| 8 | 15 | 1 | 1 | 112.6 | 5.1 | 1.7 | 0.018 |
| 9 | 38.7 | 1 | 1 | 112.6 | 2.0 | 1.5 | 0.017 |
| 10 | 77.4 | 1 | 1 | 112.6 | 1.0 | 1.7 | 0.015 |

3.4.2 Changes in Amplitude



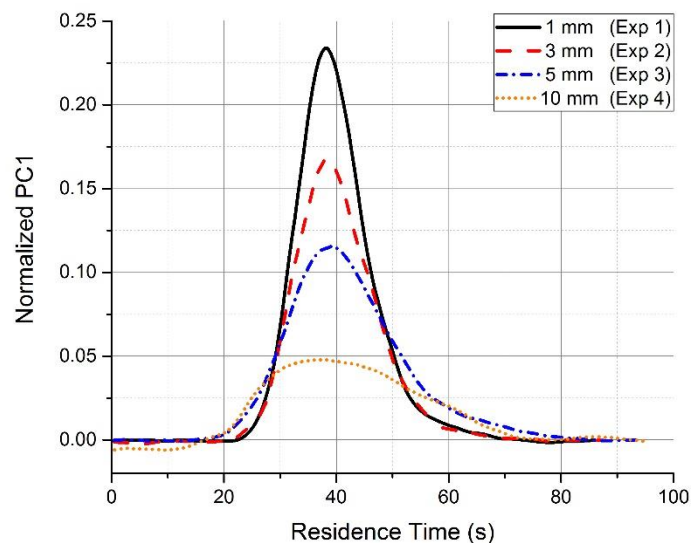
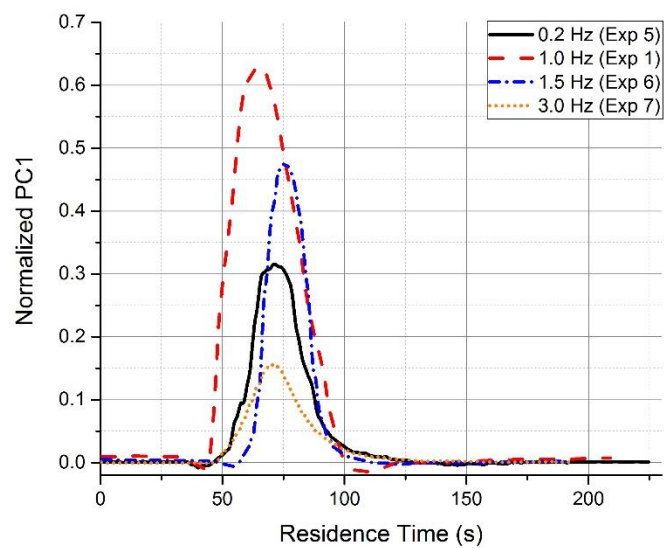
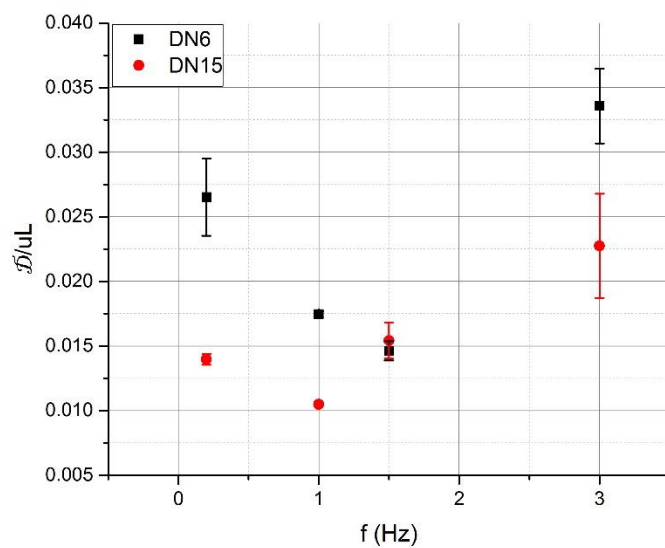


Figure 3.4 (top) Measured dispersion coefficients over a range of piston amplitudes (middle) RTDs in the DN6 (bottom) RTDs in the DN15

As the amplitude of the piston increases, the width of the RTD broadens and the dispersion coefficient increases. The stroke length of the piston directly influences the RTD because a longer drawback leads to more back mixing and inherent deviation from plug flow operation. Similarly, large amplitudes can lead to the fluid passing through multiple baffles, leading to additional non-idealities in flow behavior. Note that these results are in line with those found by Kacker and Mackley in that operating at minimal amplitude leads to the lowest dispersion coefficient. Although minimal dispersion leads to “plug flow” behavior, one must also consider the minimal energy required to maintain solid suspension in two phase applications like crystallization. Solid suspension is essential to prevent system clogging and particle settling. With respect to process design, one must choose appropriate piston conditions keeping in mind the direct proportionality of the solid’s settling velocity to both the size and true density of the crystal.^[23]

3.4.3 Changes in Frequency



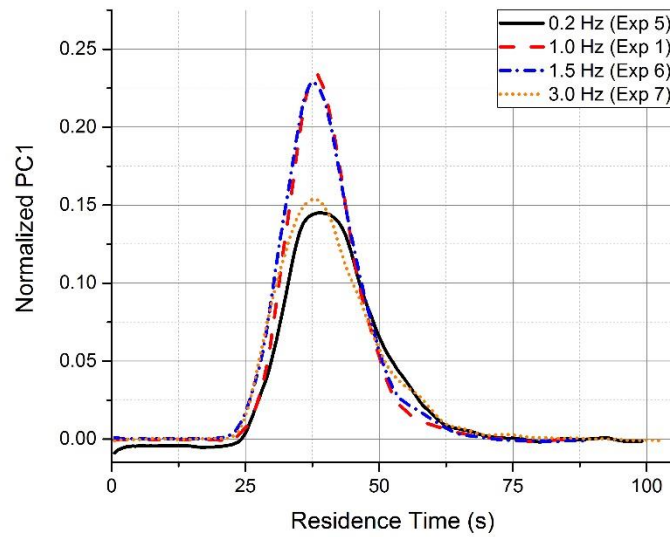


Figure 3.5 (top) Measured dispersion coefficients over a range of piston frequencies (middle) RTDs in the DN6 (bottom) RTDs in the DN15

Similar to the results shown by Dickens, varying the frequency of the piston had an uncorrelated effect on the dispersion experienced by the system. Optimal operation was found to be at 1.5 Hz for the DN6 and 1.0 Hz for the DN15 when the amplitude was constant at 1 mm. Both high and low frequency operation saw more of a ‘tailing effect’ on the residence time distribution and this may be insightful in describing vortex propagation for the given baffle geometries. Because frequency seems to have an effect on the shape of the RTD, changing the frequency of the forward vs backwards plunges may be of interest. This operating strategy gives rise to the idea that asymmetrical oscillations could minimize dispersion such that plug flow operation is achievable at a variety of operating conditions and may be important for solid suspension applications.

3.5 System Sensitivity to Flow Type

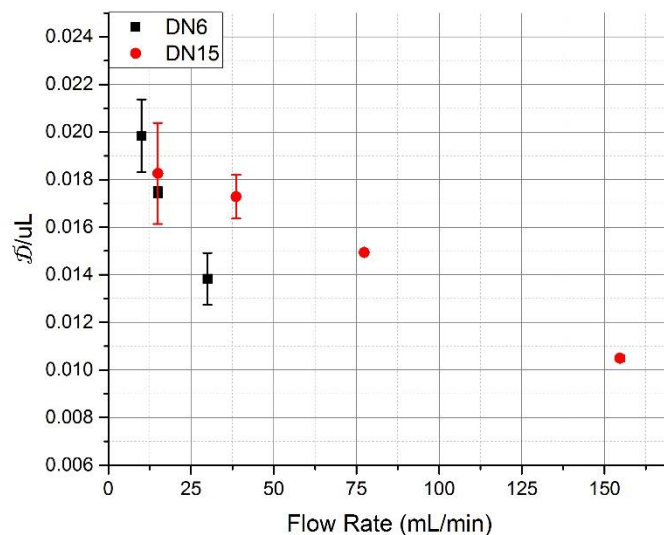


Figure 3.6 Measured dispersion coefficients at different pump flow rates

Over the range of flow rates in this study, the dispersion coefficient decreases as the pump induced flow rate increases under constant piston conditions. Higher flow rates clear the pulse tracer faster and are less affected by the oscillations of the piston. That is, piston oscillations generate substantial back mixing as previously described in the amplitude analysis section of the results. Again, there exists a trade-off between minimizing dispersion and generating turbulence. One of the advantages of an oscillatory flow strategy is decreased system length as compared to the traditional PFR. Unrealistically long lengths are often required in PFR systems to generate the turbulence required for solid suspension. By superimposing oscillations onto the net flow, OFBRs generate similar turbulent conditions, but at lower flow rates with the tradeoff being increased dispersion in the system.

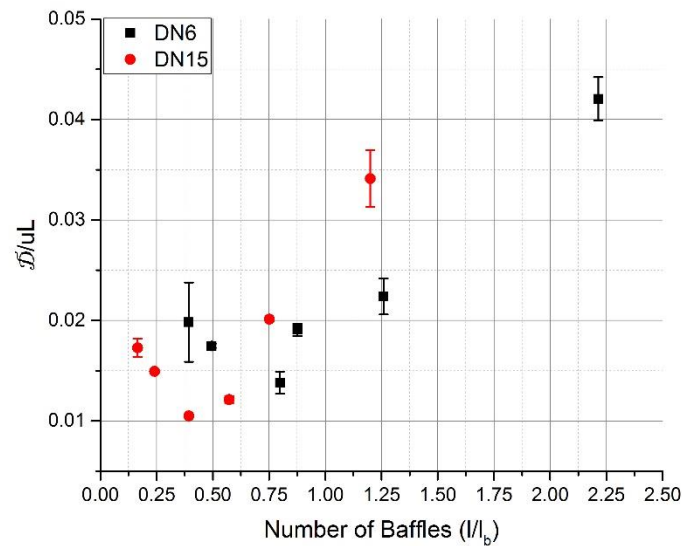


Figure 3.7 Measured dispersion as the fluid flows through a set number of baffles per second

In order to properly address optimal operating strategies for both OFBC systems, one must consider how far the fluid is travelling with each stroke of the piston. Initial intuition would lead one to consider how dispersion changes as a result of how much volume is pushed through a baffle with a single forward piston stroke. While adequate for describing a single system, this reasoning does not address the different diameters of each OFBR. In other words, because both S and l_b vary between the two systems, comparing volume equivalents is insufficient in describing the “spreading” of the pulse tracer. A more appropriate means of evaluation is to compare the axial distances travelled by the pulse tracer with l_b .

Figure 3.7 describes how dispersion changes as the axial net flow of the fluid traverses multiple baffles. Oddly enough, both OFBR systems exhibit a minimum dispersion coefficient at some pivot point (roughly 0.8 for the DN6 and 0.4 for the DN15). As the fluid gets pushed past multiple baffles, the dispersion coefficient drastically increases. However, when the fluid does not travel a far enough axial distance, the dispersion also increases, which seems perplexing.

This phenomenon gives rise to distinguishing between two types of flow regimes: pump dominated and piston dominated flow.

The mechanism by which fluid flows through the OFBR can be broken down into two parts: axial flow generated by the forward stroke of the piston and axial flow generated by the peristaltic pump. Piston generated flow can be approximated by dividing the volume of fluid displaced by the piston each second by the cross-sectional area of the tube. Pump generated flow is approximated by dividing the volumetric flow rate of the pump by the cross-sectional area of the tube. Using these approximations along with equation (12), piston and pump dominated flow regions are defined in Figure 3.8.

$$\text{Piston to Total Ratio} = \frac{\text{Axial Piston Flow}}{\text{Axial Pump Flow}} \quad (12)$$

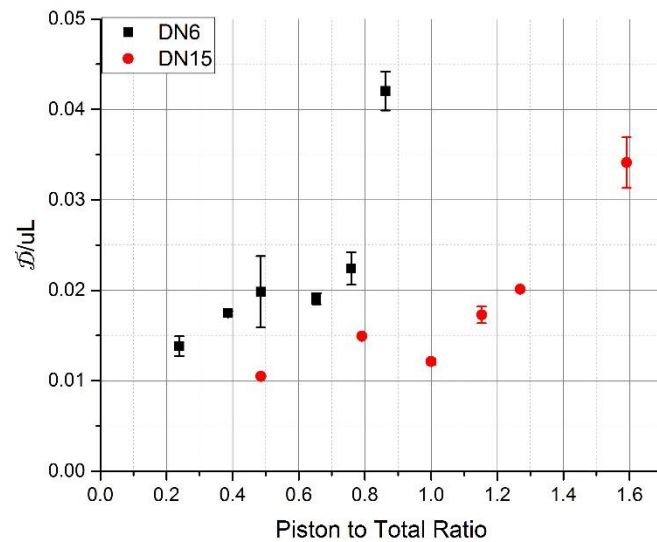


Figure 3.8 Measured dispersion while operating in either piston or pump dominated flow

Figure 3.8 transforms the data from Figure 3.7 into a more appropriate treatment of system parameters. By distinguishing the mechanisms by which fluid is being axially transferred, the relationship between dispersion and flow becomes quite apparent. In piston dominated flow (Ratios $> \sim 0.75$ in the DN6 and Ratios $> \sim 1.0$ in the DN15), the dispersion coefficient grows rapidly because the superimposed oscillations largely affect the net flow generated by the pump. In pump dominated flow, system dispersion is lower and therefore ideal for operation. In operating a two-phase system, one would want to design process parameters such that the system is operating in pump dominated flow while tailoring the oscillations to ensure proper solid suspension. Together, pump driven flow and controlled oscillations allow for narrow residence time distributions which directly correlate to narrow crystal size distributions (CSDs) for a variety of pharmaceutical applications.

3.6 Conclusions

In this study, the effects of oscillation parameters on system dispersion were evaluated across two commercially available reactors of different scale. Oscillation amplitude was found to have a positive correlation with the dispersion coefficient, with the minimum dispersion coefficient occurring at 1 mm for both systems. This result agrees with those previously presented in the literature. Piston frequency was also evaluated and it was found that optimal operation occurred at 1.5 Hz for the DN6 and 1 Hz for the DN15. However, varying the piston frequency did not have as significant of an impact as the piston amplitude on the dispersion coefficient. Moreover, this result supports Kacker's claim that the mixing parameter Ψ is insufficient in characterizing the oscillatory system.

Prior to this study, distinguishing between pump driven and piston driven flow was omitted in the literature. Piston driven flow leads to an increase in measured dispersion due to

the significant back mixing effects that counteract the net flow. While minimal dispersion is desired, one must also keep in mind the inherent benefits of piston oscillations. In liquid reaction systems, vigorous oscillatory mixing improves process kinetics by increasing the propensity of intermolecular interactions. In solid-liquid crystallization systems, the piston oscillations are essential for solid suspension to prevent particle settling and clogging. Therefore, proper OFBC operation is in a pump dominated region which minimizes dispersion, while keeping in mind the oscillatory demands of the system.

Acknowledgements

The authors thank the Department of Education for the funding support through the Graduate Assistance in Areas of National Need (GAANN) program.

Notes

The authors declare no competing financial interest.

3.7 References

- [1] Stonestreet, P., & Harvey, A. P. (2002). A Mixing-Based Design Methodology for Continuous Oscillatory Flow Reactors. *Chemical Engineering Research and Design*, 80(January), 31–44.
- [2] Peña, R., & Nagy, Z. K. (2015). Process Intensification through Continuous Spherical Crystallization Using a Two-Stage Mixed Suspension Mixed Product Removal (MSMPR) System. *Crystal Growth and Design*, 15(9), 4225–4236.
- [3] Stonestreet, P., & Veeken, P. M. J. V. A. N. D. E. R. (1999). The effects of oscillatory flow and bulk flow components on residence time distribution in baffled tube reactors, 77.
- [4] Kacker, R., Regensburg, S. I., & Kramer, H. J. M. (2017). Residence time distribution of dispersed liquid and solid phase in a continuous oscillatory flow baffled crystallizer. *Chemical Engineering Journal*, 317, 413–423.
- [5] Dickens, A. W., Mackley, M. R., & Williams, H. R. (1989). Experimental residence time distribution measurements for unsteady flow in baffled tubes. *Chemical Engineering Science*, 44(7), 1471–1479.
- [6] Ni, X., & Pereira, N. E. (2000). Parameters Affecting Fluid Dispersion in a Continuous Oscillatory Baffled Tube. *AIChE Journal*, 46(1), 37–45.
- [7] McDonough, J. R., Phan, A. N., & Harvey, A. P. (2015). Rapid process development using oscillatory baffled mesoreactors - A state-of-the-art review. *Chemical Engineering Journal*, 265(1), 110–121.
- [8] Abbott, M. S. R., Harvey, A. P., Perez, G. V., & Theodorou, M. K. (2013). Biological processing in oscillatory baffled reactors: operation, advantages and potential. *Interface Focus*, 3(1), 20120036.

- [9] Ni, X., Jian, H., & Fitch, a. . (2002). Computational fluid dynamic modelling of flow patterns in an oscillatory baffled column. *Chemical Engineering Science*, 57, 2849–2862.
- [10] P.N.X. Gough, K. Symes, Experimental flow visualisation in a modified pulsed baffled reactor, *J. Chem. Tech. Biotechnol.* 69 (1997) 321–328.
- [11] Ni, X., Brogan, G., Struthers, A., Bennett, D. C., & Wilson, S. F. (1998). A systematic study of the effect of geometrical parameters on mixing time in oscillatory baffled columns. *Chemical Engineering Research and Design*, 76(A5), 635–642.
- [12] McGlone, T., Briggs, N. E. B., Clark, C. A., Brown, C. J., Sefcik, J., & Florence, A. J. (2015). Oscillatory Flow Reactors (OFRs) for Continuous Manufacturing and Crystallization. *Organic Process Research and Development*, 19(9), 1186–1202.
- [13] Phan, A. N., & Harvey, A. P. (2012). Characterisation of mesoscale oscillatory helical baffled reactor-Experimental approach. *Chemical Engineering Journal*, 180, 229–236.
- [14] Ni, X., Mackley, M. R., Harvey, A. P., Stonestreet, P., Baird, M. H. I., & Rama Rao, N. V. (2003). Mixing Through Oscillations and Pulsations—A Guide to Achieving Process Enhancements in the Chemical and Process Industries. *Chemical Engineering Research and Design*, 81(3), 373–383.
- [15] Ni, X. W. (1994). Residence Time Distribution Measurements in a Pulsed Baffled Tube Bundle. *Journal of Chemical Technology and Biotechnology*, 59(3), 213–221.
- [16] Dickens, A. W., Mackley, M. R., & Williams, H. R. (1989). Experimental residence time distribution measurements for unsteady flow in baffled tubes. *Chemical Engineering Science*, 44(7), 1471–1479.
- [17] Smith, K. B. (1999). The Scale-Up of Oscillatory Flow Mixing. *PhD Thesis, University of Cambridge*, (September).

- [18] Levenspiel, O., & Smith, W. K. (1995). Notes on the diffusion-type model for the longitudinal mixing of fluids in flow. *Chemical Engineering Science*, 50(24), 3891–3896.
- [19] Pápai, Z., & Pap, T. L. (2002). Analysis of peak asymmetry in chromatography. *Journal of Chromatography A*, 953(1–2), 31–38.
- [20] Wold, S., (2004). Principal Component Analysis. *Chemometrics and Intelligent Laboratory Systems*, 2, 1–31.
- [21] Bro, R., & Smilde, A. K. (2014). Principal component analysis. *Analytical Methods*, 6(9), 2812–2831.
- [22] Ramkrishna, D. (1974). Stirred pots, tubular reactors, and self-adjoint operators, 29(6), 1353–1361.
- [23] Jacobs, C. N., Merchant, W., Jendrassak, M., Limpasuvan, V., Gurka, R., & Hackett, E. E. (2016). Flow scales of influence on the settling velocities of particles with varying characteristics. *PLoS ONE*, 11(8), 1–20.

4. PROCESS INTENSIFICATION THROUGH CONTINUOUS SPHERICAL CRYSTALLIZATION USING AN OSCILLATORY BAFFLED CRYSTALLIZER (OBC)

Reproduced with minor modifications and permission from Ramon Peña*, Joseph A. Oliva*, Christopher L. Burcham**, Daniel J. Jarmer**, Zoltan K. Nagy*. *Crystal Growth and Design*, 17,4776-4784. Copyright 2017 American Chemical Society.

*School of Chemical Engineering, Purdue University, West Lafayette, IN 47907, US

**Eli Lilly and Company, Indianapolis, IN 46285, US

4.1 Abstract

Drug substance purification by crystallization is a key interface in going from drug substance synthesis to final formulation and can often be a bottleneck in process efficiency. There has been increased importance in the development of continuous crystallization systems of active pharmaceutical ingredients to produce crystals with targeted physical and biopharmaceutical properties. Continuous spherical crystallization (CSC) is a process intensification technique that can address many of the present flaws (*e.g.* size distribution, downstream processing efficiency) of traditional crystallization systems. In this study, a novel concept and method in the field of process intensification through continuous spherical crystallization is proposed. This study is based on performing crystallization/spherical agglomeration in an oscillatory flow baffled crystallizer (OFBC). OFBCs are comparable to plug flow crystallizers (PFCs) in that they are both tubular crystallizers, however, the OFBC has periodically spaced orifice baffles with oscillatory motion overlapped on the net flow. Independent crystallization mechanisms can theoretically be achieved through spatially distributed solution, solvent, anti-solvent, and bridging liquid addition; offering more control of each mechanism. However, this study shows

that the OFBC allows for spatially distributed addition of solvents but achieving control of each mechanism individually proved difficult due to the back mixing of the system.

Keywords: process intensification, spherical crystallization, oscillatory flow baffled crystallizer, OBC

4.2 Introduction

As the pharmaceutical industry continues to adopt different aspects of continuous processing, process intensification will be a key driver towards more integrated unit operations. Process intensification is defined as the integration of innovative techniques and technologies to create sustainable solutions to current industrial production difficulties. It is comprised of two parts: novelty in equipment^{[1],[2]} and novelty in processing techniques.^{[3]-[10]} Continuous process intensification techniques lead to improved product quality, process safety and efficiency, and a reduction in waste/maintenance. These techniques allow for development and manufacturing at laboratory scale, ultimately reducing time to market and improving patent life utilization.^{[2],[3],[10]-[12]}

Spherical crystallization is inherently a process intensification technique due to its ability to eliminate further downstream unit operations and improve particulate flow properties while promoting higher processing efficiency. Continuous spherical crystallization provides the ability to directly connect upstream reaction synthesis to separation and purification unit operations. Peña & Nagy^[2] and Tahara et al.^[14] implemented continuous spherical crystallization using a mixed suspension mixed product removal (MSMPR) system. Tahara et al. used a single-stage MSMPR to carry out a quasi-emulsion solvent diffusion (QESD)^{[15],[16]} spherical crystallization technique with a solvent recycle stream. The recycling of solvent from the mother liquor resolves two major issues common to spherical crystallization: low yield and maintaining the low ratio of

solvent (API carrier) to anti-solvent. Peña & Nagy used a spherical agglomeration (SA)^{[17],[18],[19]} technique in a two-stage MSMPR system where the first stage was the nucleation/growth dominated stage and the second stage was the agglomeration dominant stage through the use of a bridging liquid (binder). Their work focused on the ability to alter both the properties of the internal (primary) crystals and the agglomerates by independently changing operating conditions in each stage. Independent control of internal and external properties provides the ability to achieve a target primary crystal size for bioavailability and a target agglomerate size for drug product manufacturability. The ease of ‘knowledge transfer’ from batch to continuous operation using the design concept of a MSMPR was evident when comparing the feasibility of spherical crystallization in Peña & Nagy and Tahara et al. to those of batch operations.^{[15],[18]}

The MSMPR framework provides a straightforward technology transfer from batch operations since the mixing dynamics for both systems can be similar (independent of the net flow). The MSMPR system can be expanded in capacity and degrees of freedom through the addition of a cascade of multiple stages.^{[20],[21]} These characteristics make the MSMPR one of the more flexible continuous systems. However, broad crystal size distributions (CSD) are typically obtained as a result of the broad residence time distributions (RTD) experienced by crystals.^{[22],[23]} Another concern when using multistage MSMPR systems is appropriately transferring crystal slurry through each stage while maintaining the crystallizer operating conditions.^{[2],[24],[25]} Plug flow reactors (PFRs) are an alternative continuous system that are known to deliver narrower CSDs. However, PFRs usually require high flow rates to create the desired mixing quality via turbulence. This requirement can lead to physically unrealistic lengths to achieve appropriate residence times.^{[2],[14]} As a design alternative to PFRs, the oscillatory flow baffled reactor (OFBR) is a plug flow reactor where an oscillatory motion is superimposed on

the net fluid flow through the use of a piston near the reactor inlet. Periodically spaced baffles along the reactor length create changes in the reactor internal diameter, leading to paired eddy propagation as the net flow oscillates back and forth.^[2] The zone between each pair of baffles is assumed to be uniformly mixed and acts as a continuous stir tank reactor. Figure 4.1 is a schematic that illustrates the fluid flow pattern of the oscillatory system. In some cases, the mixing capabilities of an OFBR are enhanced relative to a PFR, leading to improved heat transfer, longer residence times, turbulent mixing with laminar net flow Reynolds (Re_n), smaller reactor volume, and narrower CSDs.^{[2],[26],[27],[28]}

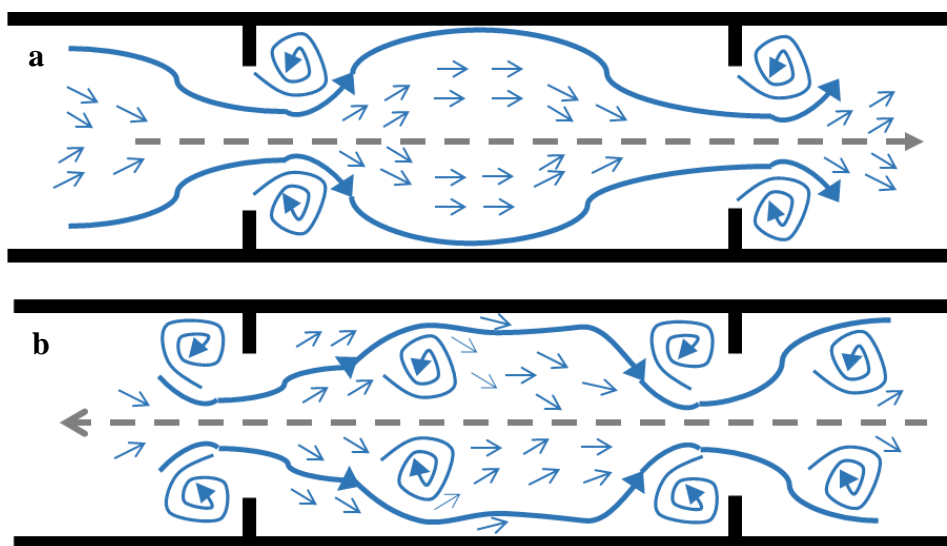


Figure 4.1 Schematic of the fluid flow pattern in an OFBR/C with net flow to the right: a) forward stroke b) backward stroke. Adapted from Ni et al.^{26,27}

There are four key dimensionless parameters often used to define the fluid flow patterns in an OFBR, which include the oscillatory Reynolds number (Re_o), the net flow Reynolds number (Re_n), the Strouhal number (St), and Ψ , the ratio of oscillatory and net flows.

$$Re_o = \frac{2\pi x_0 f \rho D}{\mu} \quad (1)$$

$$Re_n = \frac{\rho u D}{\mu} \quad (2)$$

$$St = \frac{D}{4\pi x_0} \quad (3)$$

$$\Psi = \frac{Re_o}{Re_n} \quad (4)$$

The variables in equations 1-4 are as follows: x_0 is the piston amplitude, f is the oscillation frequency, ρ is the fluid density, D is the internal diameter of the tube segment, u is the mean superficial fluid velocity, and μ is the fluid viscosity. The Strouhal number (St) represents the effective eddy propagation through the ratio of the tube diameter to piston stroke length.^{[27],[28]} The Re_o measures the intensity of the oscillations generated by the piston and therefore, the turbulence level imposed on the fluid. The Reynolds number (Re_n) is the ratio of inertial to viscous forces. The volumetric flow rate limits the Re_n in the system, despite the impeding oscillatory flow imposed by the piston. The ratio of the Reynolds numbers (Re_o/Re_n) results in a dimensionless mixing parameter, ψ , a measure of oscillatory versus net flows. Large ψ values result in “well-mixed” sections between the baffles^{[27],[29]}.

The objective of this study was to conduct continuous spherical crystallization in an oscillatory flow baffled crystallizer (OFBC) system. Conceptually, the system enables the application of various types of spherical crystallization techniques; allowing for both simultaneous and independent nucleation, growth, and agglomeration mechanisms. The ability to have spatially independent zones within a crystallizer where only one crystallization mechanism is dominant offers additional degrees of freedom for the control of final product properties. This technique allows for products to be tailored for biopharmaceutical benefit and efficacy (*e.g.*

bioavailability, dissolution rate, particle morphology) and processing efficiency (*e.g.* filtration and drying times). The feasibility of spherical crystallization within a OFBC was studied via a series of experiments in which the control crystallization mechanisms and final product properties were investigated.

4.3 Materials and Method

4.3.1 Lab Reagents

Benzoic acid (C_6H_5COOH) ($\geq 99.5\%$ purity, Sigma Aldrich) was used as the model compound in this study. Benzoic acid spherical agglomeration has been studied in the literature^{[2],[17],[18]} making it an ideal candidate for this study. The solvent system consisted of ethanol (pure, 200 pf, USP grd, Decon Labs), deionized water, and toluene ($\geq 99.5\%$ assay, Fisher Scientific). Ethanol served as the solvent in which to prepare benzoic acid solutions, water as the anti-solvent, and toluene as the bridging liquid. Acetic acid ($\geq 99.5\%$ assay, Fisher Chemical), water (Optima LC/MS grade, Fisher Chemical) and methanol (Optima LC/MS grade, Fisher Chemical) were used for ultra-performance liquid chromatography (UPLC) quantification of benzoic acid. The spherical agglomerates created were filtered and dried at $60\text{ }^\circ\text{C}$ for 24 hours. A Nikon microscope was used to take images of the spherical agglomerates. Image analysis software (ImageJ) was used to determine the agglomerate size distribution (Ferret diameter) and assess final agglomerate morphology.

4.3.2 Experimental Setup

The OFBC was evaluated for a continuous spherical crystallization system using a spatially distributed solvent/anti-solvent/binder addition strategy. In this system, nucleation and growth occur in the first four segments due to supersaturation created by mixing solution and anti-

solvent, while bridging liquid is added at the end of the fourth segment, leaving a four-segment agglomeration zone. Figure 4.2 is a picture of the experimental setup and illustrates the nucleation, growth, and agglomeration zones. Changing the binder addition location makes the agglomeration zone flexible in that adjusting this residence time allows one to tailor agglomerate size to a desired size target.

The OFBC used in this work (Figure 4.2) was a Nitech DN15 (Alconbury Weston Ltd) consisting of eight segments and a total volume of 1250 mL. All segments and elbows of the DN15 were jacketed for temperature control. The temperature was controlled by using four thermo-regulators (Huber Ministat 125/Julabo F25-ME) effectively dividing the OFBC into four temperature zones. The first zone (consisting of one segment) was kept at 40 °C to dissolve particles and prevent particles from reaching the piston which can lead to damage/leaking. The rest of the zones (consisting of seven segments) were kept at 22 °C. There is a temperature gradient from 40 °C to 22 °C at the interface between the first and second segments, however the temperature converges to 22 °C by the exit of the second segment and is uniform through the remaining segments of the OFBC. The solution was added at the end of the first zone to ensure an antisolvent process. Peristaltic pumps (MasterFlex L/S by Cole-Palmer) and platinum cured silicon tubing (MasterFlex L/S by Cole-Palmer) were used for both solution and anti-solvent feed into the OFBC (100-150 mL/min). A Waters 515 HPLC pump was used to feed toluene at the bridging liquid injection point through an injector (1.32-1.65 mL/min). A control unit allows for setting the oscillation amplitude (mm) and frequency (Hz). A Lasentec focused beam reflectance measurement (FBRM) S400 was used for on-line monitoring of the particle chord length distribution within the system.

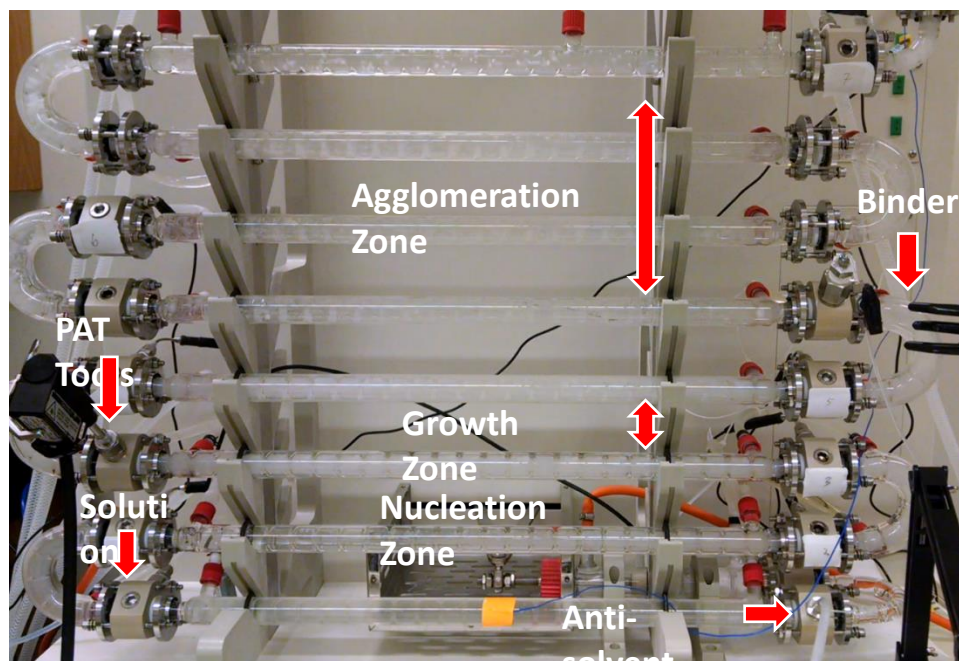


Figure 4.2 OFBC configuration indicating location of anti-solvent, solution and binder addition as well as PAT port (FBRM)

4.3.3 UPLC Method for Benzoic Acid Quantification

UPLC techniques differ from high performance liquid chromatography (HPLC) techniques in that they utilize columns with smaller diameters and particles (larger surface area to volume ratio), and therefore higher pressures to increase peak capacity (number of peaks resolved per unit time) and decrease retention time.^[30] Benzoic acid quantification for both the determination of steady state and solubility data used an Acquity UPLC system (Waters Corporation). The system utilizes column, sample, and binary solvent managers coupled with Tunable Ultraviolet (TUV) detection in an offline setup to create an output signal that is later processed using the Empower 3.1 software (Waters Corporation). The stationary phase was an Acquity UPLC BEH C18 column 2.1 mm x 100 mm, 1.7 μ m, while the mobile phase was a combination of 1.5 % (v/v) acetic acid (in water) solution and HPLC grade methanol in an 85:15 ratio by volume. The diluent contains the same two solutions as the mobile phase, but in a 55:45 ratio by volume. Each

sample injection was 10 μL and the flow rate of the mobile phase was 0.5 mL/min. The temperature of the column was 40°C and the UV detection wavelength was 243 nm.

4.3.4 Benzoic Acid Solubility Determination

Benzoic acid was dissolved in ethanol/water solutions of varying proportions (0.1-0.4 ethanol/water (v/v)) and were held at ambient conditions for 24 hours with intermittent mixing to reach equilibrium. The supernatant fluid was assumed to be at saturation. The samples were centrifuged for five minutes and the supernatant fluid was nano-filtered (200 nm pore size). Using this filtered saturated solution in a 10x dilution with ethanol and a manually prepared benzoic acid standard, the UPLC method generated a solubility curve as a function of solution to anti-solvent ratio (SASR). To validate the equilibrium measurement, a second approach was also implemented. Benzoic acid was dissolved in pure ethanol (the solvent) before water (the anti-solvent) was added in a dropwise manner. This anti-solvent addition induced crystallization and the slurry was held at ambient conditions for 24 hours with constant mixing to reach equilibrium. With this additional step, both nucleation and dissolution rates are removed from the uncertainty as the measured concentration of benzoic acid in solution should be the same using either method. Figure 4.3 shows experimentally determined solubility data that was used for choosing operating conditions in the OFBC.

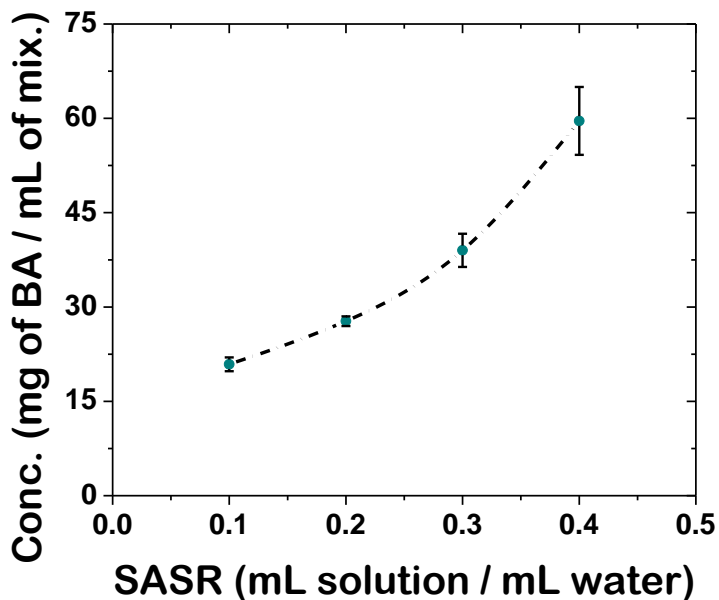


Figure 4.3 UPLC generated solubility of benzoic acid in ethanol solution-water mixtures of different ratios

4.3.5 Experimental Procedure

4.3.5.1 Degassing Feed Solution

An in-house degassing system was built to remove the risk of generating air bubbles during the operation of the OFBC. To remove the dissolved gas prior to injection, the solution was heated to 40°C with constant stirring (150 rpm) in a 5L jacketed vessel with a retreat curve stirrer (dia. 140 mm). In addition to the temperature shift, the vessel pressure was decreased using a vacuum pump (ultimate vacuum pressure of 110 torr, Welch by Gardner Denver). The decrease in pressure also decreases the solubility of air in solution. The entire system was held under these conditions for one hour before injection into the OFBC. The degassing process was limited to an hour because there is a tradeoff in removing trapped air and evaporating ethanol from the vessel. However, the concentration of benzoic acid was determined offline prior to injection, ensuring comparable starting conditions between experiments. The degassing process was a batch operation which impacted the length of each experimental run time.

4.3.5.2 OFBC Concentration Sampling

After reaching steady state based on stabilized particle counts measured by the FBRM, a sample was taken from the bridging liquid injection port before connecting the toluene feed line (refer to Figure 4.2). Once bridging liquid addition was initiated, samples (3 mL) were taken at the outlet to determine if steady state was also maintained in the liquid phase throughout the process. This approach serves to cross-validate the solid phase (particle counts) and liquid phase (concentration) based steady state assumption since crystallization processes depend on both phases. The samples taken at the outlet were filtered through (200 nm) pores before being diluted 10x with ethanol and inserted into the UPLC. Figure 4.4 shows an example of the concentration data used to monitor the process for 12 residence times (refer to experiment 3 from Table 4-1). The figure shows the benzoic acid concentration as a function of time for the duration of the experiment with the slight oscillation in the measurement due to the RTD in the liquid phase.^[32] The measured concentration data corresponds to a steady state supersaturation of $\Delta C = 23$ mg/mL (absolute supersaturation) or expressed as a ratio $S = 1.6$ ($S = C/C_{\text{sat}}$). S is the supersaturation ratio, C is the concentration, and C_{sat} is the saturation concentration.

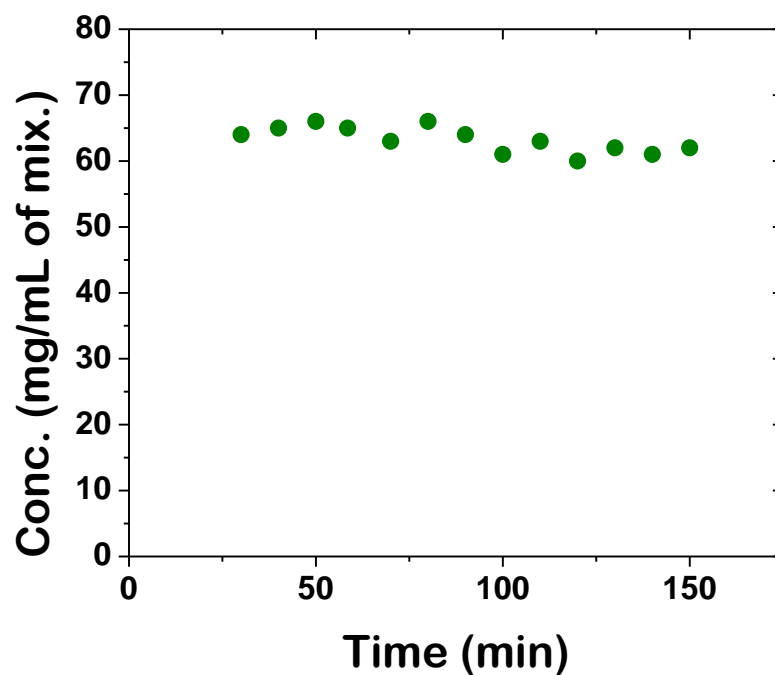


Figure 4.4 Concentration of benzoic acid as a function of time measured at the outlet of the OFBC.

4.4 Results and Discussion

Several process parameters were varied between each experiment (refer to Table 4-1). As previously mentioned, the lumped parameter (ψ) determines the intensity of mixing within the OFBC. Five distinct values of ($\psi = 12, 33, 56, 58, \text{ and } 82$) were chosen to determine the sensitivity of agglomerate formation to the mixing conditions. The lower and upper values were chosen based on the manufacturer's recommendations for mixing and safe operation of the equipment; with two intermediate values to assess the operating range. Supersaturation, and hence slurry density, in the initial OFBC tube segments are varied by changing the SASR (0.18-0.30) and the benzoic acid (BA) concentration of the feed (0.08-0.125 g/mL). The bridging liquid to solute ratio (BSR) impacts both the extent of agglomeration and the agglomeration mechanism. The BSR was varied (0.6-1.2) to alter agglomeration size and decrease the number of un-agglomerated particles. The SASR, concentration, and BSR ranges were chosen based on

previously successful spherical agglomeration experiments.^[32] The remaining variables in Table 4-1 include the amplitude, frequency, residence time, oscillatory Reynolds (Re_o) and mean particle size (D_m).

Table 4-1 Summary of the experimental conditions

| Exp. | Conc. of BA (g/mL) | SASR | BSR | RT (min) | f (Hz) | x_0 (mm) | Re_o | Ψ | D_m (mm) |
|------|--------------------|------|------|----------|----------|------------|--------|--------|------------|
| 1 | 0.08 | 0.30 | 0.80 | 10.0 | 1.5 | 15 | 1974 | 12 | 3.0 |
| 2 | 0.08 | 0.30 | 0.80 | 8.33 | 3.0 | 25 | 6581 | 33 | 1.8 |
| 3 | 0.08 | 0.30 | 1.00 | 10.0 | 3.5 | 30 | 9213 | 56 | 2.3 |
| 4 | 0.08 | 0.30 | 0.80 | 12.5 | 3.5 | 35 | 10748 | 82 | 1.4 |
| 5 | 0.08 | 0.18 | 0.80 | 12.5 | 3.5 | 35 | 11015 | 82 | 1.6 |
| 6 | 0.08 | 0.25 | 0.80 | 12.5 | 3.5 | 35 | 10853 | 82 | 1.6 |
| 7 | 0.125 | 0.30 | 0.80 | 12.5 | 3.5 | 35 | 10748 | 82 | 1.5 |
| 8* | 0.08 | 0.30 | 0.85 | 12.5 | 3.5 | 35 | 10748 | 82 | 1.7 |
| 9* | 0.08 | 0.25 | 0.85 | 12.5 | 2.5 | 35 | 7752 | 58 | 1.3 |

*Exp.8: agglomeration zone consisted of three segments, Exp. 9: agglomeration zone consisted of two segments

4.4.1 Evaluation of Mixing Conditions

Experiment 1 had the least turbulent mixing conditions ($\psi = 12$) and resulted in a broad agglomerate size distribution (ASD) as shown in Figure 4.5. In spherical agglomeration systems, the bridging liquid preferentially wets the crystals in suspension. Agglomerate formation then depends on particle collisions. Poor oscillatory mixing prevented uniform bridging liquid distribution, caused particle settling, and reduced collision events, resulting in a tri-modal ASD. This tri-modality is a result of particles left un-agglomerated due to reduced collisions, larger particles created due to particle settling, and very large particles created from over-agglomeration due to poor bridging liquid distribution. As mixing intensity increased ($\psi = 33$ to 82), the ASD improved significantly, average agglomerate size decreased, and the system could run at a controlled state. The ASDs and images of agglomerates at the different mixing intensities are shown in Figure 4.5. Note that images were not presented for experiment 1 due to the large particles that were out of the viewing field of the microscope and the broad size distribution that could not be represented in a single image. At a constant total flowrate, there

was significant improvement in the ASD by increasing the amplitude and frequency of oscillations (experiment 1 vs. 3). Increasing residence time combined with increasing oscillatory mixing, allowed for improved agglomeration due to more sustained collisions and consolidation of agglomerates (experiment 1, 2 and 4). Overall, increased oscillatory mixing led to a narrower ASD, smaller average agglomerate sizes, and reduced particle settling/fouling. For these reasons, the mixing intensity remained high in each of the latter studies. Note that experiment 3 ($\psi = 56$) does not follow the trend of decreasing mean size and narrower ASD as mixing intensity increases due to the difference BSR value when compared to experiments 2 and 4.

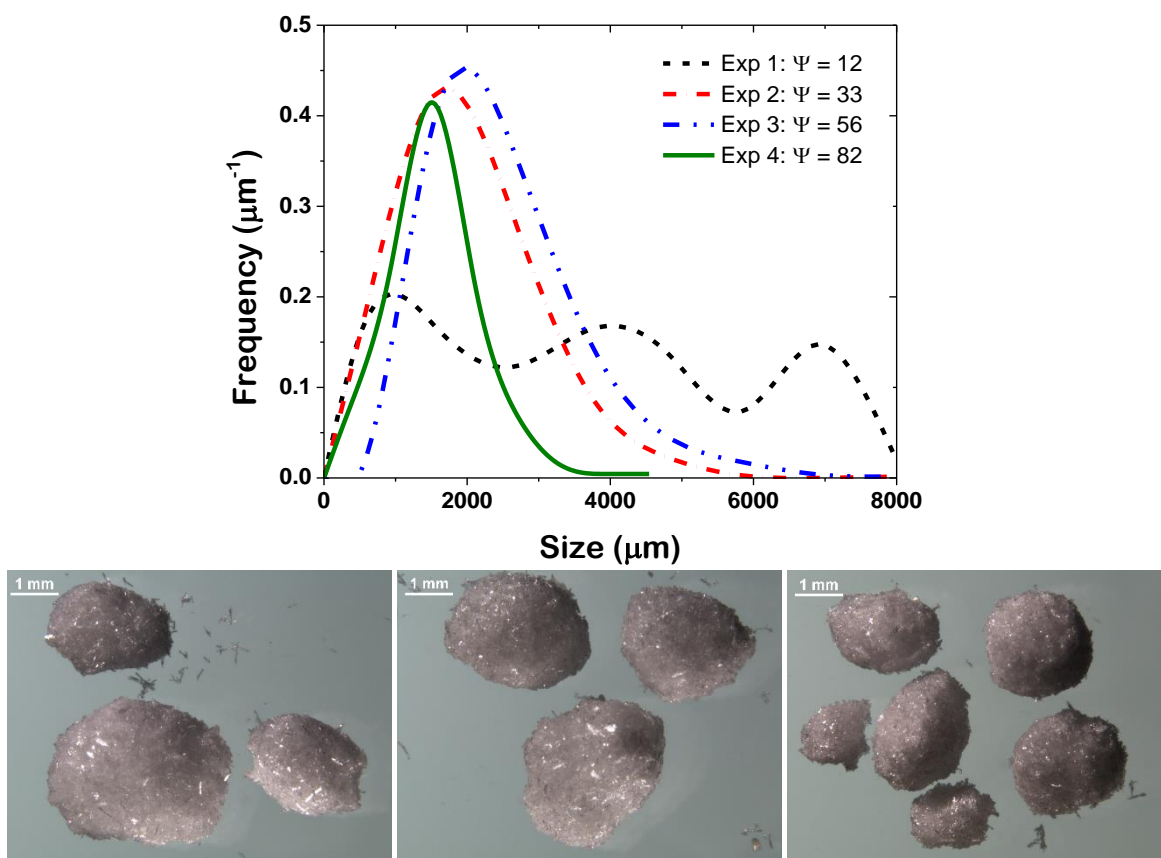


Figure 4.5 (top) Size distributions for different oscillatory mixing intensities and (bottom) agglomerates from experiments with increasing mixing intensity from left to right (exp. 2-4)

4.4.2 Initial supersaturation variations via SASR

Benzoic acid solution and anti-solvent are mixed in the first segment of the OFBC. Assuming the system is perfectly mixed, the SASR dictates the initial operating point in the phase diagram (initial supersaturation). In experiment 5, the SASR is low at 0.18, resulting in a higher initial supersaturation compared to experiments 4 and 6. Operating at such a low SASR (high supersaturation) increases slurry density due to higher nucleation. This supersaturation, and subsequent nucleation, is maintained throughout the agglomeration zone (refer to Figure 4.2), resulting in many un-agglomerated crystals and a bimodal ASD (Figure 4.6). As the SASR increases from 0.18 to 0.25 to 0.30, the ASD narrows, the average agglomerate size decreases, and the maximum agglomerate size decreases. It is important to note the maximum agglomerate size, or the breadth of the ASD, as it is related to the RTD of the system.^[31]

For each set of operating conditions, the maximum agglomerate size of each experiment captures a portion of the system dynamics. From Figure 4.6 it is apparent that increasing the slurry density (at constant net flow) broadens the ASD due to increased dispersion, suggesting that the RTD of the system is related to slurry density.^[31] From a phase diagram perspective, a decrease in SASR can have the same effect on the RTD of the system as increases in concentration. At constant concentration, increasing the SASR past 0.30 results in an increase in the solubility of the system impeding sufficient supersaturation to crystallize. It is important to note that changes in the SASR (at a constant BSR) will also affect the operating point within the ternary phase diagram (ethanol-water-toluene).^[32] Changes in the operating point in the ternary phase diagram affect the immiscibility of the bridging liquid which can cause changes in the agglomeration mechanism. Very low SASR increases the immiscibility of the bridging liquid moving it above the critical maximum BSR limit. Very high SASR will have the opposite affect;

moving the bridging liquid below the critical minimum. At the SASR conditions studied, no significant differences in the agglomeration mechanisms were observed.

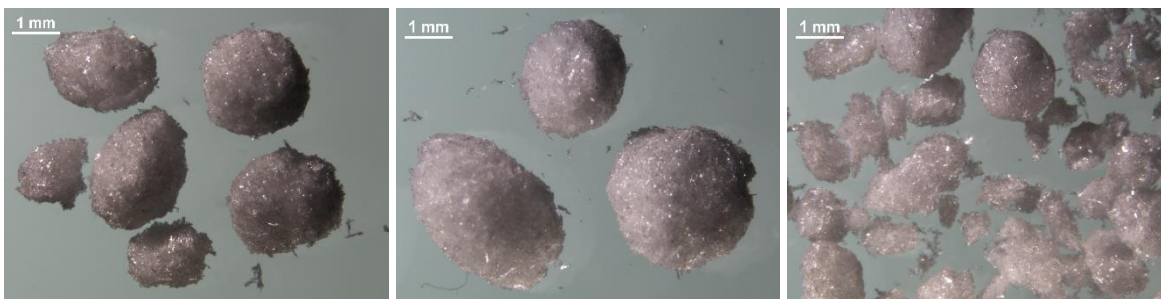
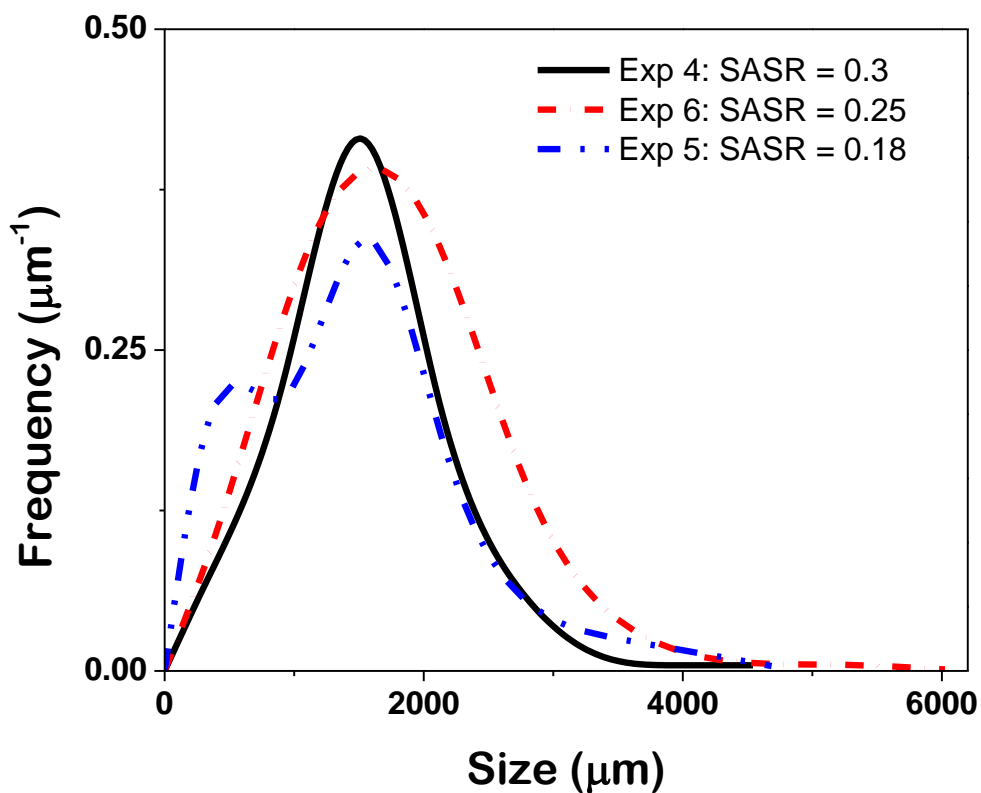


Figure 4.6 (top) Agglomerate size distributions for different SASR ratios and (bottom) agglomerates from experiments with decreasing SASR from left to right.

4.4.3 Initial supersaturation variations via benzoic acid concentration

At a constant SASR, the initial concentration of benzoic acid in solution dictates the crystallization starting point in the phase diagram (initial supersaturation). Increasing the concentration from 0.08 g/mL to 0.125 g/mL, induced more clogging/fouling in the system,

broadened the ASD and the maximum agglomerate size dramatically increased (Figure 4.7). Increasing the initial supersaturation increases both primary and secondary nucleation. As with changes in the SASR, an increase in slurry density via increases in concentration can result in inconsistent agglomerate sizes and clogging/fouling. As concentration increases, the effects of RTD contribute significantly to the broadening of the ASD and the increase of the maximum agglomerate size. Concentrations above the values reported here were attempted but were unsuccessful due to clogging/fouling. Based on the observed trends, there is an optimal slurry density that minimizes the effects of RTD and avoids clogging/fouling.

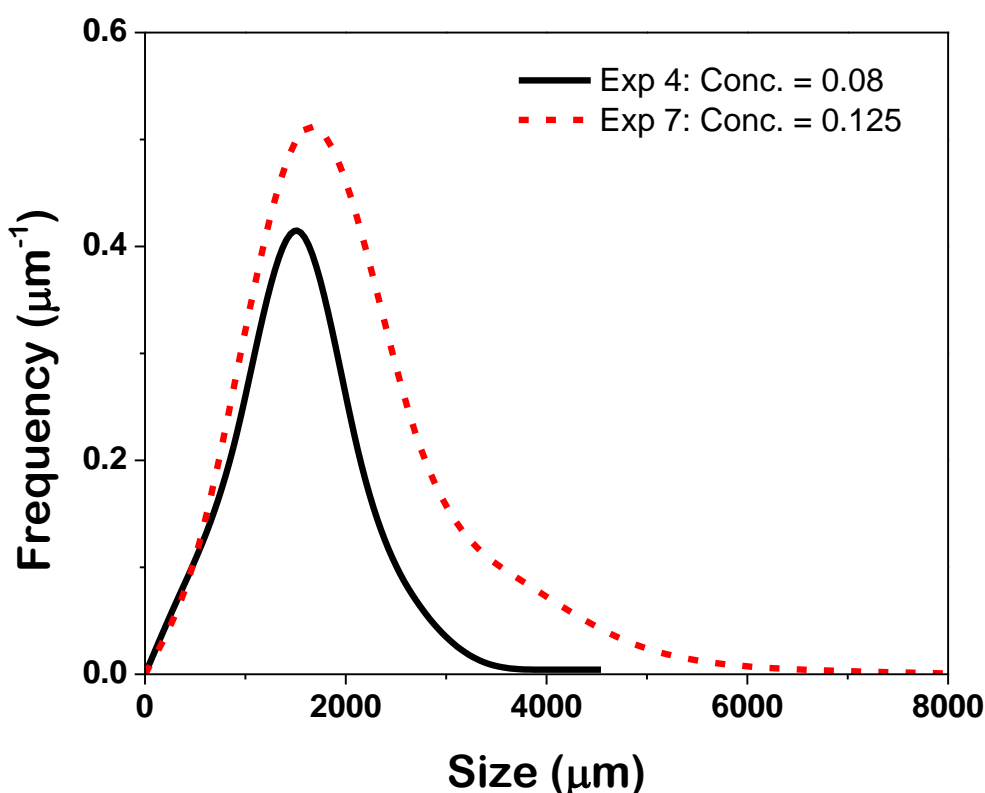


Figure 4.7 Agglomerate size distributions for different solution concentrations of benzoic acid

4.5 Changes in BSR

Spherical agglomeration techniques generally have narrow BSR operating ranges which induce spherical agglomerate formation.^{[2],[17],[18]} Changing this ratio drastically changes the final

ASD and can change the agglomeration mechanism.^[32] After increasing the BSR from 0.8 to 1.0, the average agglomerate size increased from 1.4 to 2.3 mm. The ASD broadened and the maximum agglomerate size dramatically increased as shown in Figure 4.8. As the bridging liquid is increased to the critical range, the agglomeration mechanism becomes increasingly adhesive as the particles have a greater bridging liquid film. The increased adhesiveness of the particles results in a greater propensity for successful collisions (collisions that result in agglomerate formation), particularly in agglomerate-agglomerate collisions. When two agglomerates adhere, the system generates large particles and results in the broad distributions shown in Figure 4.8.

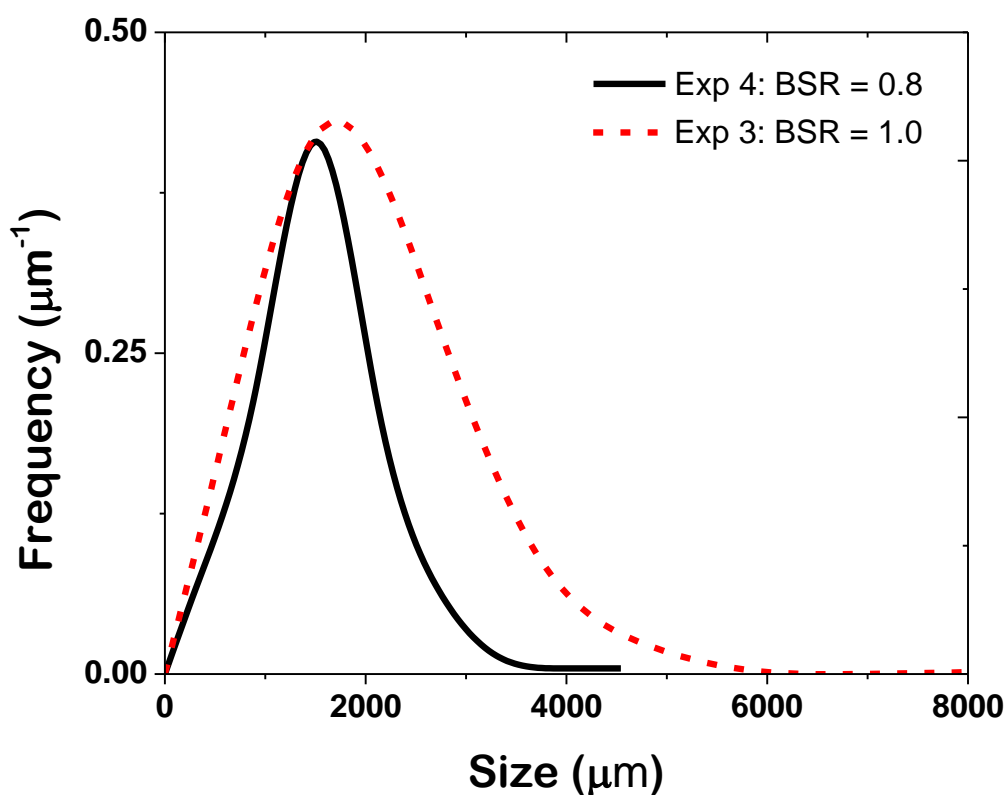


Figure 4.8 Agglomerate size distributions for different BSR

4.5.1 Set point changes in BSR

One of the proposed advantages of continuous processes is the ability to make set point changes to operating conditions to adjust final product properties. For this study, set point

changes in BSR were investigated to assess the feasibility of adjusting the final agglomerate properties while maintaining constant primary crystal properties. Set point changes in BSR were carried out at intermediate time steps during experiment 6 (refer to Table 4-1) before setting the system to its original operating conditions afterwards. Figure 4.9 shows the FBRM total counts and square weighted mean chord length (SWMCL) data over time as well as images of primary crystals from the experiment. The data shows that a controlled state of operation (CSO) was attained after four residence times (50 min). The primary crystals in the images were collected at the end of the third residence time at the outlet of OFBC after which binder addition was initiated. The images of the primary crystals show the needle/rod-like morphology of the benzoic acid crystals and their relatively large size.

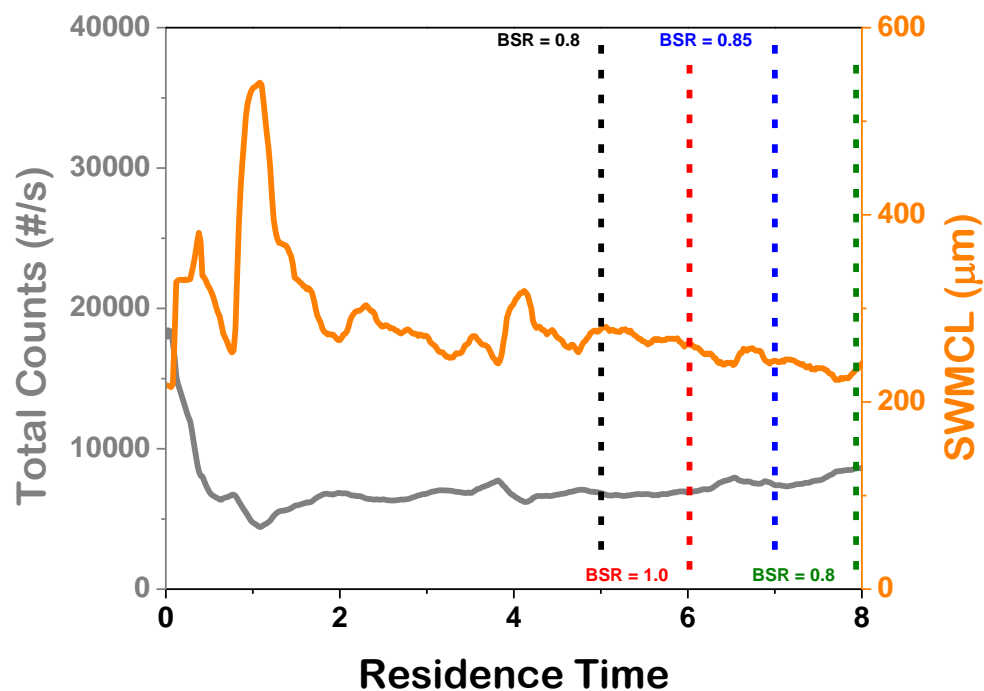


Figure 4.9 Total counts and square weighted mean chord length (SWMCL) from FBRM probe

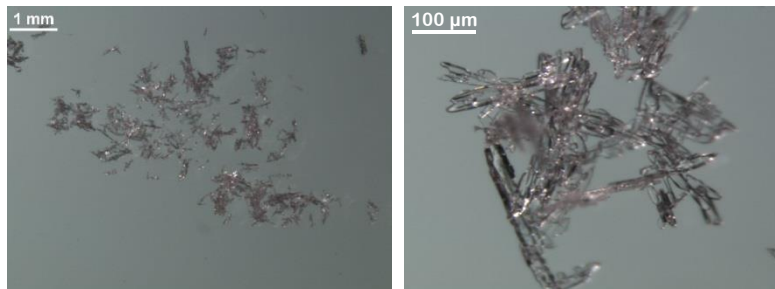


Figure 4.10 Images of the primary crystals prior to agglomeration

Once under a CSO, the BSR was changed at the end of each residence time. The following set point changes in BSR took place: the system began operation with a BSR of 0.80, increased to a BSR of 1.0, decreased to 0.85 and then brought back to its original value of 0.80. Figure 4.11 shows the ASDs and images of agglomerates after the various set point changes. The fifth residence time corresponds to the first residence time after a CSO is reached per the FBRM data. However, given the breadth and maximum frequency of the ASD at the fifth residence, it is apparent that the agglomeration portion of the OFBC was not yet in a CSO. This observation suggests that there is a delay in the CSO of the primary crystals versus that of the agglomerates. However, the observation is not unexpected given that the binder addition was not initiated until the third residence time. When the BSR is increased to 1.0 (RT 6) the ASD has a significant shift to the right as expected. Due the fact that only one RT was allowed for the step change response there is still a portion of the distribution corresponding to the original ASD prior to the change (RT 5). This observation suggests that one RT is not enough to achieve a CSO after a set point change. After the BSR is decreased to 0.85 and then to 0.80, the ASD shifts to the left returning to the uniform, normal distributions observed in previous sections. From the ASDs and images, it is evident that agglomerate properties can be adjusted throughout operation by set point changes in the operating conditions.

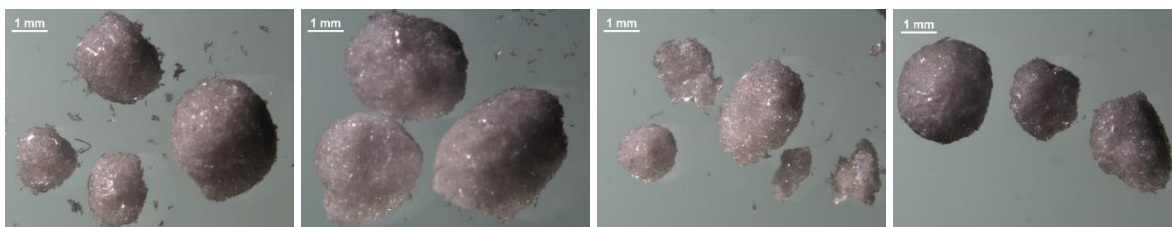
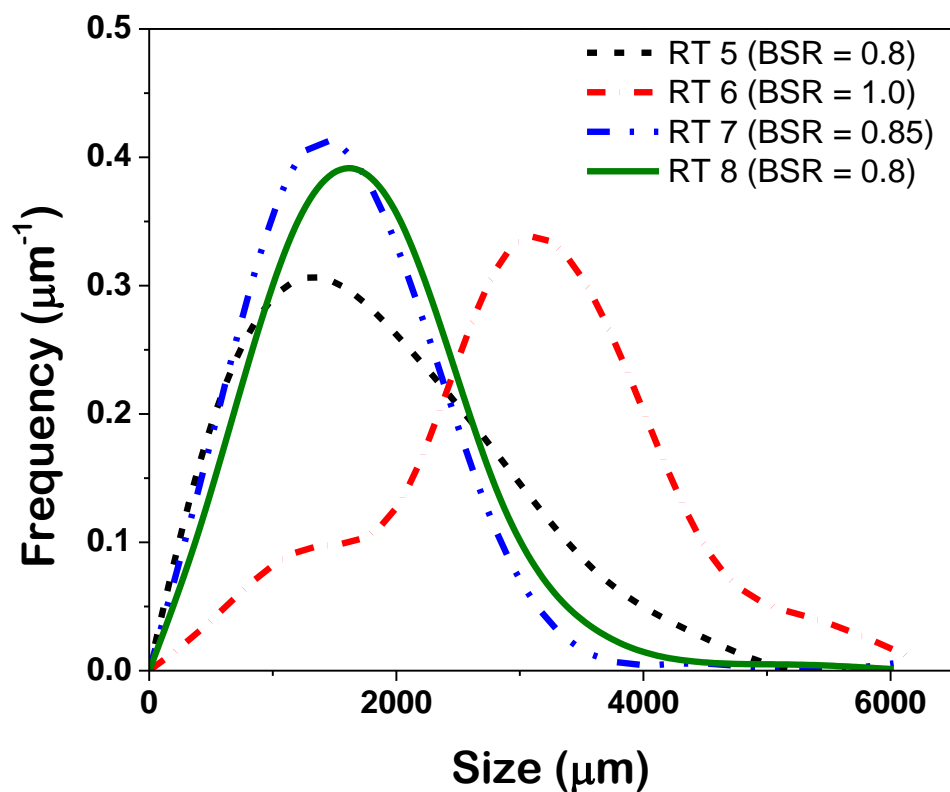


Figure 4.11 (top) Agglomeration size distributions for step changes in BSR and images of agglomerates at different residence times. (bottom from left to right) BSR = 0.8, BSR = 1.0, BSR = 0.85 and BSR = 0.8.

4.6 Evaluation of Different Agglomeration Zone Lengths

The ability to easily change the configuration of the OFBC is a major advantage of the Nitech DN15. Changes in the jacket temperature of individual segments and location of injection points can allow for optimized experimental conditions. The previous results used the configuration shown in Figure 4.2. Injecting the binder at the beginning of the fifth segment created an agglomeration zone consisting of the final four segments. For the studies that

evaluated the impact of the agglomeration zone, the system is reconfigured by changing the location of the binder injection to change the length of the agglomeration zone while keeping the total length of the OFBC constant. Experiments were run for agglomeration zones consisting of three, two and one segment(s) with the operating conditions of experiment 4 used as reference.

When the operating conditions were held at the reference point, none of the configurations produced spherical agglomerates. Decreasing the agglomeration zone by one segment decreases the volume of the zone by approximately $1/7$ or 14%. This decrease in volume, along with an already short residence time (12.5 min), does not provide sufficient time for agglomeration to occur. To create spherical agglomerates, changes in the operating conditions must compensate for the lost time for agglomeration. Experiment 8 (refer to Table 4-1) used a three-segment agglomeration zone and required an increase in BSR to produce spherical agglomerates. Experiment 9 (Table 4-1) used a two-segment agglomeration zone and required an increase in BSR and a decrease in ψ . Figure 4.12 shows the ASDs for experiment 4, 8 and 9 along with images of the spherical agglomerates.

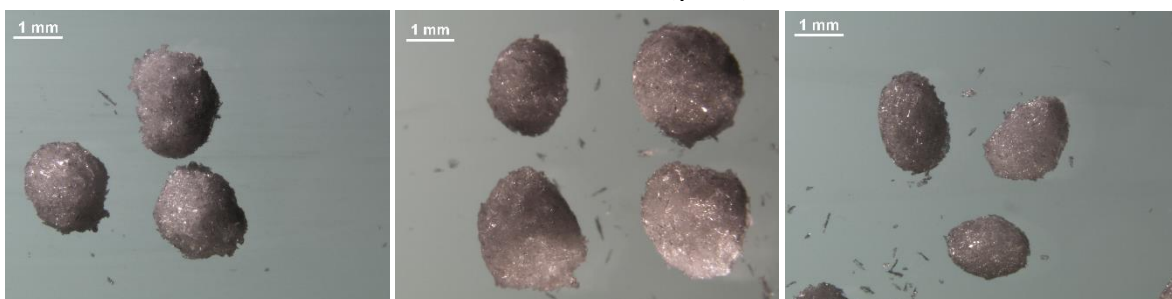
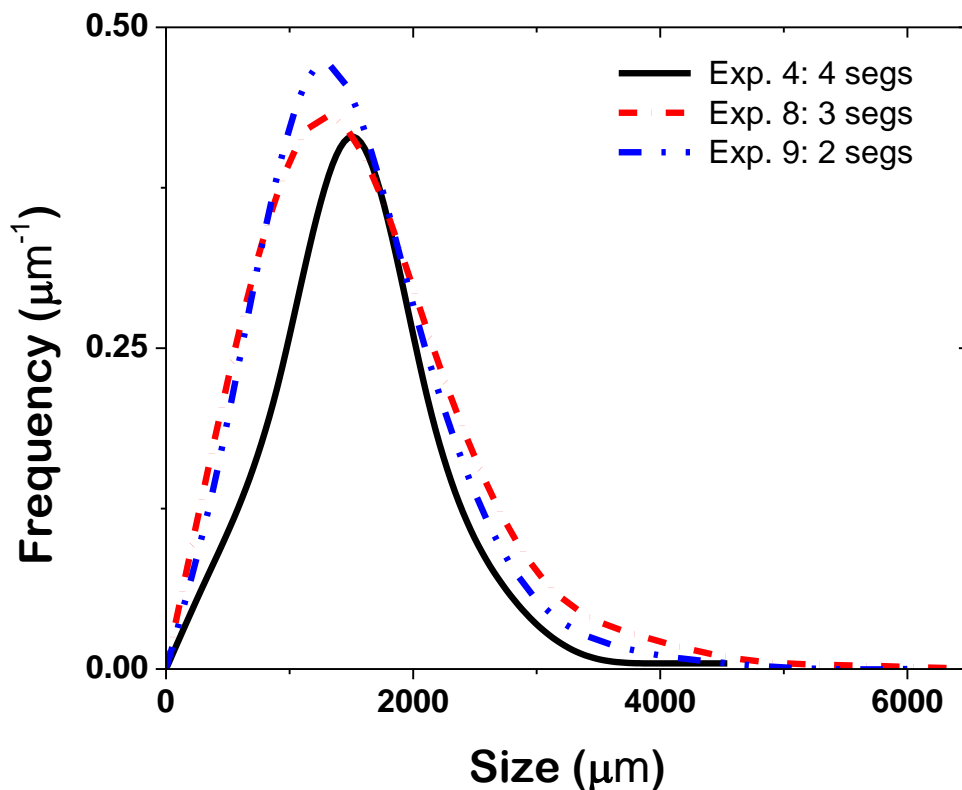


Figure 4.12 (top) Agglomerate size distributions for different agglomeration zone configurations and (bottom from left to right) images of agglomerates from experiments 4, 8 and 9

As evident by the ASDs and images of the agglomerates the experiments produced agglomerates of similar size distributions and mean sizes; with experiments 8 and 9 having broader ASDs and slightly larger mean sizes. The broader ASD can be attributed to the larger growth zone compared to experiment 4 which would contribute to a broader and larger crystal size distribution prior to agglomeration. As the agglomeration zone length decreases, the effects of dispersion/back mixing have a greater effect on the nucleation and growth than on the

agglomeration mechanism with proper adjustments of the BSR. Experiment 8 required an increase in BSR to increase agglomeration and counteract the reduced agglomeration zone residence time. Experiment 9 required an increase in BSR to increase agglomeration and a decrease in the mixing intensity to reduce the dispersion of crystals from the growth zone. Reducing the crossing particles from the growth zone into the agglomeration zone allows the agglomeration to proceed without the effects of introducing new particles. Two segment agglomeration zone experiments at higher mixing intensities consistently produced a combination of spherical agglomerates and fine crystals. The effects at the interface between the growth and agglomeration can be overcome when the agglomeration zone is larger.

4.7 Summary of Results

Spatially distributing API solution, anti-solvent, and bridging liquid along the length of the crystallizer led to independent control of mechanisms within the OFBC system. Various crystallization operating conditions were evaluated in the OFBC. Knowledge of the initial point in the phase diagram and the mixing ability of the OFBC allowed for an assessment of the effects of various operating parameters on the implementation of a spherical agglomeration technique. Increased mixing intensity significantly improved the final agglomeration size distribution (narrower, smaller mean size). A $\psi = 82$ was found to be optimal in this study. $\Psi = 82$ was the limit attempted in this study due to the stability of system as excessive vibrations can affect the crystallization process. However, further increasing the ψ parameter should follow the same trends observed in this study at the expense of increased back mixing/dispersion. To achieve successful spherical agglomeration experiments, residence time (8.33-12.5 min) and benzoic acid solution concentration (0.08 and 0.125 g/mL) were kept relatively low. The slurry density should be limited to avoid fouling, clogging and particle settling, and decrease the effects of residence

time distributions. Broadening of the residence time distribution can be limited with decreased slurry density which leads to more narrow/uniform distributions. The supersaturation and slurry density was controlled by maintaining the solution concentration and the solution to anti-solvent ratios at appropriate levels (BA conc. at 0.08 g/mL, SASR at 0.30). Higher flow rates and mixing intensities also slow the buildup of fouling on crystallizer walls by reducing the possibility of particle settling. A solution concentration of 0.08 g/mL benzoic acid in ethanol and a SASR of 0.3 were found to be the optimal values in this study. The experimental conditions present in this study were largely determined by the avoidance of fouling. Thus, the experiments created very large primary crystals and spherical agglomerates. Higher nucleation rates could lead to smaller primary particle sizes and ultimately much smaller agglomerate sizes. However, fouling will be a bottleneck in such a process unless a continuously seeded system is studied. Lastly, as has been shown in the literature^[2], the critical bridging liquid to solute ratio (BSR) range narrows for continuous systems. A BSR of 0.80 was found to be the optimal in this study, with minimum room for adjustment. Table 4-2 summarizes the overall trends in mean size and ASD for the various process parameters.

Table 4-2 Summary of experimental results

| Properties | | Effect of Process Parameters | | | | |
|------------------|----------------|------------------------------|-------------------|--------------------|------------------|------------------------|
| <i>Mean Size</i> | decreases with | $\Psi \uparrow$ | SASR \downarrow | Conc. \downarrow | BSR \downarrow | Agg. Segs \downarrow |
| | increases with | $\Psi \downarrow$ | SASR \uparrow | Conc. \uparrow | BSR \uparrow | Agg. Segs \uparrow |
| <i>ASD</i> | narrows with | $\Psi \uparrow$ | SASR \uparrow | Conc. \downarrow | BSR \downarrow | Agg. Segs \uparrow |
| | broadens with | $\Psi \downarrow$ | SASR \downarrow | Conc. \uparrow | BSR \uparrow | Agg. Segs \downarrow |

4.8 Conclusions

The OFBC is a viable option for applications in continuous crystallization. Given the OFBC's ability to be configured to optimize specific properties of interest, it also has application

in process intensification. The benefit of a plug flow type of crystallizer is the ability to achieve product of narrower final properties. The broad agglomerate size distributions observed throughout this study contradict this fact. The results presented here suggest the oscillatory flow baffled crystallizer deviates from an ideal plug flow crystallizer; with the effects of dispersion of the residence time distribution appearing to be most significant factor in that deviation. The findings in this study agree with RTD studies in literature that suggest the operating ranges studied here could cause significant dispersion.^[31] The results show RTD to be related to slurry density. Increases the slurry density appeared to have led to increases in dispersion and back mixing. The effects of slurry density should be investigated further, especially for spherical agglomeration processes. Overall the agglomerate size distributions show improvement (narrower, more uniformity) over the distributions observed in an MSMPR.^[2] A series of staged MSMPRs proves to be more efficient in decoupling the crystallization mechanisms because the stages are physically separated and are completely independent from one another. In the OFBC, the mixing (expressed through the Ψ) was the same through and between the different crystallization zones which can lead to multiple mechanisms occurring at the interface of different zones due to dispersion or back-mixing. Within the experimental framework studied here and in Peña & Nagy^[2], the MSMPR does not exhibit fouling issues allowing it to operate at much higher supersaturation ratios; leading to finer smaller primary crystals. However, for optimal operating conditions, the OFBC proves effective in producing agglomerates of consistent quality. The superimposed oscillatory mixing of OFBC allows for process development at a wide range of productivity levels (from benchtop to pilot to manufacturing scale) without changes in equipment volume.

Acknowledgements

The authors thank Eli Lilly & Co. for their advice and funding support through the Lilly Research Award Program (LRAP), the Department of Education for their funding support through the Graduate Assistance in Areas of National Need (GAANN) program, and Waters Corporation for providing the PATROL UPLC system and technical support throughout the work.

4.9 References

- [1] Roberge, D. M.; Zimmermann, B.; Rainone, F.; Gottsponer, M.; Eyholzer, M.; Kockmann, N. Microreactor technology and continuous processes in the fine chemical and pharmaceutical industry: Is the revolution underway? *Org. Process Res. Dev.* 2008, 12, (5), 905–910.
- [2] Lawton, S.; Steele, G.; Shering, P.; Zhao, L.; Laird, I.; Ni, X. Continuous Crystallization of Pharmaceuticals Using a Continuous Oscillatory Baffled Crystallizer. *Org. Process Res. Dev.* 2009, 13, (6), 1357–1363.
- [3] Acevedo, D. A.; Ling, J.; Chadwick, K.; Nagy, Z. K. Application of Process Analytical Technology-Based Feedback Control for the Crystallization of Pharmaceuticals in Porous Media. *Cryst. Growth Des.* 2016, 16, (8), 4263–4271.
- [4] Alvarez, A. J.; Myerson, A. S. Continuous Plug Flow Crystallization of Pharmaceutical Compounds. *Cryst. Growth Des.* 2010, 10, (5), 2219–2228.
- [5] Acevedo, D. A.; Peña, R.; Yang, Y.; Nagy, Z. K. Evaluation of Mixed Suspension Mixed Product Removal Crystallization Processes Coupled with a Continuous Filtration System. *Chem. Eng. Process.* 2016, 108, 212-219.
- [6] Yang, Y.; Song, L.; Zhang, Y.; Nagy, Z. K. Application of wet milling-based automated direct nucleation control in continuous cooling crystallization processes. *Ind. Eng. Chem. Res.* 2016, 55, 4987-4996.
- [7] Yang, Y.; Song, L.; Gao, T.; Nagy, Z. K. Integrated Upstream and Downstream Application of Wet Milling with Continuous Mixed Suspension Mixed Product Removal Crystallization. *Cryst. Growth Des.* 2015, 15, 5879-5885.

- [8] Yang, Y.; Song, L.; Nagy, Z. K. Automated Direct Nucleation Control in Continuous Mixed Suspension Mixed Product Removal Cooling Crystallization. *Cryst. Growth Des.* 2015, 15, (12), 5839–5848.
- [9] Nagy, Z. K.; Braatz, R. D. Advances and New Directions in Crystallization Control. *Annu. Rev. Chem. Biomol. Eng.* 2012, 3, 55–75.
- [10] Stankiewicz, A.; Moulijn, J. A. Process intensification. *Ind. Eng. Chem. Res.* 2002, 41, (8), 1920–1924. doi:10.1007/s10098-012-0466-5
- [11] Nagy, Z. K.; Fevotte, G.; Kramer, H.; Simon, L. L. Recent advances in the monitoring, modelling and control of crystallization systems. *Chem. Eng. Res. Des.* 2013, 91, (10), 1903–1922.
- [12] Simon, L. L.; Pataki, H.; Marosi, G.; Meemken, F.; Hungerbühler, K.; Baiker, A.; Tummala, S.; Glennon, B.; Kuentz, M.; Steele, G.; Kramer, H. J. M.; Rydzak, J. W.; Chen, Z.; Morris, J.; Kjell, F.; Singh, R.; Gani, R.; Gernaey, K. V.; Louhi-Kultanen, M.; O'Reilly, J.; Sandler, N.; Antikainen, O.; Yliruusi, J.; Frohberg, P.; Ulrich, J.; Braatz, R. D.; Leysens, T.; von Stosch, M.; Oliveira, R.; Tan, R. B. H.; Wu, H.; Khan, M.; O'Grady, D.; Pandey, A.; Westra, R.; Delle-Case, E.; Pape, D.; Angelosante, D.; Maret, Y.; Steiger, O.; Lenner, M.; Abbou-Oucherif, K.; Nagy, Z. K.; Litster, J. D.; Kamaraju, V. K.; Chiu, M. Assessment of recent process analytical technology (PAT) trends: A multiauthor review. *Org. Process Res. Dev.* 2015, 19, (1), 3–62.
- [13] Peña, R.; Nagy, Z. K. Process Intensification through Continuous Spherical Crystallization Using a Two-Stage Mixed Suspension Mixed Product Removal (MSMPR) System. *Cryst. Growth Des.* 2015, 15, (9), 4225–4236.

- [14] Tahara, K.; O'Mahony, M.; Myerson, A. S. Continuous Spherical Crystallization of Albuterol Sulfate with Solvent Recycle System. *Cryst. Growth Des.*, 2015, 15, (10), 5149–5156.
- [15] Kawashima, Y.; Niwa, T.; Handa, T.; Takeuchi, H.; Iwamoto, T.; Itoh, K. Preparation of controlled-release microspheres of ibuprofen with acrylic polymers by a novel quasi-emulsion solvent diffusion method. *J. Pharm. Sci.* 1989, 78, (1), 68–72.
- [16] Nocent, M.; Bertocchi, L.; Espitalier, F.; Baron, M.; Couarraze, G. Definition of a solvent system for spherical crystallization of salbutamol sulfate by quasi-emulsion solvent diffusion (QESD) method. *J. Pharm. Sci.* 2001, 90, (10), 1620–1627.
- [17] Katta, J.; Rasmuson, A. C. Spherical crystallization of benzoic acid. *Int. J. Pharm.* 2008, 348, (1-2), 61–69.
- [18] Thati, J.; Rasmuson, A. C. Particle engineering of benzoic acid by spherical agglomeration. *Eur. J. Pharm. Sci.* 2012, 45, (5), 657–67.
- [19] Kawashima, Y.; Cui, F.; Takeuchi, H.; Toshiyuki, N.; Hino, T.; Kiuchi, K. Parameters determining the agglomeration behaviour and the micromeritic properties of spherically agglomerated crystals prepared by the spherical crystallization technique with miscible solvent systems. *Int. J. Pharm.* 1995, 119, 139–147.
- [20] Cole, K. P.; Campbell, B. M.; Forst, M. B.; McClary Groh, J.; Hess, M.; Johnson, M. D.; Miller, R. D.; Mitchell, D.; Polster, C. S.; Reizman, B. J.; Rosemeyer, M. An Automated Intermittent Flow Approach to Continuous Suzuki Coupling. *Org. Process Res. Dev.* 2016, 20, (4), 820-830.

- [21] Cui, Y.; O'Mahony, M.; Jaramillo, J. J.; Stelzer, T.; Myerson, A. S. Custom-Built Miniature Continuous Crystallization System with Pressure-Driven Suspension Transfer. *Org. Process Res. Dev.* 2016, 20, (7), 1276–1282.
- [22] Randolph, A. D.; White, E. T. Modeling size dispersion in the prediction of crystal-size distribution. *Chem. Eng. Sci.* 1977, 32, (9), 1067–1076.
- [23] Garside, J.; Tavaré, N. S. Mixing, reaction and precipitation: Limits of micromixing in an MSMPR crystallizer. *Chem. Eng. Sci.* 1985, 40, (8), 1485–1493.
- [24] Ferguson, S.; Morris, G.; Hao, H.; Barrett, M.; Glennon, B. Characterization of the anti-solvent batch, plug flow and MSMPR crystallization of benzoic acid. *Chem. Eng. Sci.* 2013, 104, 44–54.
- [25] Hou, G.; Power, G.; Barrett, M.; Glennon, B.; Morris, G.; Zhao, Y. Development and Characterization of a Single Stage Mixed-Suspension, Mixed-Product-Removal Crystallization Process with a Novel Transfer Unit. *Cryst. Growth Des.* 2014, 14(4), 1782–1793.
- [26] Ni, X.; Jian, H.; Fitch, A. Computational fluid dynamic modelling of flow patterns in an oscillatory baffled column. *Chem. Eng. Sci.* 2002, 57(14), 2849–2862.
- [27] Ni, X.; Mackley, M. R.; Harvey, A. P.; Stonestreet, P.; Baird, M. H. I.; Rama Rao, N. V. Mixing Through Oscillations and Pulsations—A Guide to Achieving Process Enhancements in the Chemical and Process Industries. *Chem. Eng. Res. Des.* 2003, 81, (3), 373–383.
- [28] Ni, X.; Liao, A. Effects of mixing, seeding, material of baffles and final temperature on solution crystallization of l-glutamic acid in an oscillatory baffled crystallizer. *Chem. Eng. J.* 2010, 156, (1), 226–233.

- [29] Stonestreet, P.; Harvey, A. P. A Mixing-Based Design Methodology for Continuous Oscillatory Flow Reactors. *Chem. Eng. Res. Des.* 2002, 80,31–44.
- [30] Swartz, M. E. UPLC™: An Introduction and Review. *J. Liq. Chromatogr. Relat. Technol.* 2005, 28, (7-8), 1253–1263.
- [31] Kacker, R.; Regensburg, S. I.; Kramer, H. J. M. Residence Time Distribution of Dispersed Liquid and Solid Phase in a Continuous Oscillatory Flow Baffled Crystallizer. *Chem. Eng. J.* 2017, 317, 413–423.
- [32] Thati, J.; Rasmuson, A. C. On the mechanisms of formation of spherical agglomerates. *Eur. J. Pharm. Sci.* 2011, 42, (4), 365-379.

5. CONTINUOUS SPHERICAL CRYSTALLIZATION OF LYSOZYME IN AN OSCILLATORY BAFFLED CRYSTALLIZER USING EMULSION SOLVENT DIFFUSION IN DROPLETS

Reproduced with permission from Joseph A. Oliva, Wei-Lee Wu, Michael R. Greene, Kanjakha Pal, and Zoltan K. Nagy. Submitted to *the Journal of Crystal Growth and Design*, in review.

School of Chemical Engineering, Purdue University, West Lafayette, IN 47907, US

5.1 Abstract

Continuous protein crystallization is a cheaper, more efficient alternative to traditional chromatographic purification techniques. Isolating the active pharmaceutical ingredient (API) in its solid form improves stability, decreases transportation costs, and alleviates scalability concerns. In this work, the spherical crystallization of lysozyme was monitored with the Blaze 900 (Blaze Metrics, LLC) in two continuous oscillatory baffled crystallizers (OBCs); namely, the Nitech DN6 and DN15. The practicality of this technique was evaluated in terms of process sensitivity and scalability. Using an emulsion solvent diffusion (ESD) based method to generate supersaturation in droplets allows for extraordinarily fast crystallization kinetics as well as control of the final product size distribution.

Process sensitivity analysis was performed to investigate the effect of the following parameters on the product's crystal size distribution (CSD). The concentration of ethanol in the bulk phase was found to have a significant effect on crystallization kinetics, as its diffusivity drives supersaturation at the droplet interface. Although controlling supersaturation is important in determining product quality, maintaining droplet suspension near the injection site is critical to process longevity as fouling is most likely to occur in this high supersaturation region. Similarly, in scaling this process, the ratio of droplet diameter to tube diameter plays a significant role in

the formation of encrust. Increasing the size of the droplets, relative to the diameter of the system, increases the role of wall effects in distorting the final product quality. All in all, tunable process parameters provide flexibility to the final product, making the OBC an ideal platform for protein crystallization.

Keywords: Protein crystallization, oscillatory baffled crystallizer, spherical crystallization, emulsion solvent diffusion, droplet crystallization

5.2 Introduction

Protein therapeutics have grown rapidly in the pharmaceutical industry, accounting for roughly one fifth of the global revenue.^{[1],[2]} Despite their commercial successes, a number of challenges still remain; namely, the lack of production scalability. As a consequence, many current platforms for protein production have poor cost-effectiveness and short drug storage half-life.^{[3]-[5]} Chromatography is currently regarded as the best option for biopurification because it produces high purity products with good yield.^{[6],[7]} Although upstream processing technology has been dramatically improved, a bottleneck exists in downstream chromatography operations due to throughput and scalability limitations. Scale-up of chromatography is both cost and space-intensive, posing a block in production improvement that requires a scalable solution.

For small molecule active pharmaceutical ingredients (API), crystallization offers high purity purification at industrial scale. However, protein crystallization is notably more difficult than small molecule crystallization, because not all proteins can be crystallized. Most often, high-throughput plate-based screening techniques or microfluidics-type platforms are used for macromolecular crystallization.^[8] High-throughput plate-based screening techniques are useful for drug discovery, but are not feasible for commercial-scale crystallization^[9] due to their use of sub-microliter volumes of solution and high capital cost requirement.^{[10],[11]} Using a continuous

oscillatory baffled crystallizer (COBC) is an attractive option for protein crystallization, as it has the potential for linear scalability and can generate high quality product.^[12]

A COBC is an alternative to a conventional plug flow reactor (PFR). Many of the desirable characteristics of a conventional PFR for crystallization (i.e. narrower crystal size distribution (CSD)) are retained by the COBC, however, the COBC offers superior solid suspension. A piston at the bottom of the COBC superimposes oscillatory flow onto the net flow from a pump. This process generates paired eddies spaced periodically across internal baffles, increasing system turbulence^[13]. To characterize this oscillatory turbulence contribution, the Re_o is often used and is defined below.

$$Re_o = \frac{2\pi f x_0 \rho D}{\mu} \quad (1)$$

Note: x_0 is the piston amplitude, f is the oscillation frequency, ρ is the solution density, D is the diameter of the system, and μ is the solution viscosity. This system turbulence is useful in solid-liquid applications, as improper particle suspension often leads to buildup and clogging. Traditionally, PFRs require long reactor lengths because system turbulence is solely generated by a pump and crystallization kinetics are typically slow.^[14] By adding an oscillatory component to system turbulence, long residence times can be achieved without the need for high throughput rates from pumps, thus reducing reactor length.

In drug formulations, there often exists a trade-off between the bioavailability of a drug and its manufacturability. Bioavailability is largely impacted by aqueous solubility and dissolution kinetics. Generally, bioavailability favors smaller particles, due to their high surface area to volume ratios. However, small particles have poor manufacturability due to static electric forces which induce clumping and poor flowability. In contrast, manufacturability favors larger particles in the 100-150 μm range, as the total surface energy of these particles is lower, leading

to better flow properties. To overcome these characteristic differences, spherical agglomeration is used. Typically, this technique combines smaller particles into larger agglomerates through the use of a bridging liquid (also referred to as a binder). Spherical agglomeration improves both bioavailability and manufacturability, as the larger agglomerates have improved flow properties and also dissociate into their smaller constituents during dissolution testing.^[15] Increased bioavailability of spherical agglomerates has been demonstrated through improved dissolution profiles for a variety of compounds, including simvastatin,^[16] aceclofenac,^[17] ketoprofen,^[18] and tolbutamide.^[19]

From a macroscopic manufacturing point of view, utilizing spherical crystallization allows for significant improvements in process efficiency, as size control unit operations such as milling and granulation can be eliminated entirely.^[20] By minimizing fine particles (as demonstrated by Zhang^[21]), the bulk flow properties of the agglomerates are far superior to their primary particle counterparts^[22]. This size enhancement is desirable for commercial scale manufacturing, as gravity-driven transportation is popular among drug manufacturers for moving the product between unit operations.

Spherical crystallization mechanisms can be categorized into two primary modes of action. The first method utilizes a bridging liquid which surface wets crystals and acts as an adhesive,^{[23],[24]} causing clusters of crystals to form. The second method is emulsion based in which two immiscible phases are used. The good solvent initially contains the API while the poor solvent makes up the bulk of the solution phase. The good solvent is often added dropwise and the droplets are stable due to immiscibility characteristics. Some portion of the poor solvent phase must be able to diffuse into the droplet phase. Thus, a small portion (1-10%) of the poor solvent phase must be miscible with both the good and the poor solvent phases. Note: the

procedure for solvent selection using this method is outlined further in the methods section. When this component of the poor solvent phase permeates the droplet boundary, local supersaturation is very high and initiates nucleation at the droplet surface. The API continues to crystallize from the outside, inwards, but is always confined by the droplet boundary. This process is hereafter referred to as emulsion solvent diffusion (ESD).

Emulsion-generated droplet crystallization is an attractive method for protein crystallization. Droplet-based crystallization is better able to control the crystallization process, particularly with regards to the rate of molecular diffusion initializing the crystallization as well as the growth rate.^[14] Although a plethora of studies have been conducted to understand the droplet generation, few have investigated these parameters as they relate to emulsion-based crystallization, particularly for a system using a T-junction injection port to generate droplets. Zhang et. al studied nanoliter-sized droplet formation using a T-junction system, similar to that used in this study, with the intent of applying the results towards a crystallization application.^[25] In this work, three critical parameters were investigated: namely, the Reynolds number, average fluid velocity in the system, and the critical length above which gravity effects dominate capillary effects of the system. Zhang found that, in accordance with other results published in the literature for non-cylindrical flow geometries, that the droplet size increases linearly with increasing ratio of the dispersed phase velocity to the continuous phase velocity. Droplet frequency also exhibited direct proportionality to this ratio of velocities. Furthermore, as the total average fluid velocity (obtained by summing the velocities of the continuous and dispersed phases) increased, the droplet size decreased, though not in a linear fashion. The implications of these results were used in predicting the size of the droplets injected in this study, which are known to have an impact on the final CSD.

5.3 Materials and Methods

5.3.1 Solvent Selection and Screening Rationale

Spherical crystallization via emulsion solvent diffusion (ESD) in droplets was the method chosen for generating and agglomerating lysozyme crystals because using a surface-layering method (like that described by Peña) is very difficult. In essence, the surface layering method uses a small molecule (the bridging liquid) to hold a cluster of large molecules (the lysozyme protein) together and form compact spheres. However, ESD forces the product to agglomerate by creating a highly unfavorable environment for the API in the bulk phase. In this case, water was chosen as the droplet solvent, since it provides orders of magnitude higher solubility for lysozyme in comparison to organic solvents.^[26] In reference to the antisolvent phase, several critical requirements are necessary for the success of ESD, namely:

- i. The API phase (water) needs to be insoluble or sparingly soluble in the antisolvent phase (Note the antisolvent phase is comprised of Components 1 and 2)*
- ii. The majority of the antisolvent solution (Component 1) needs to be immiscible with the droplet solvent under the process conditions to ensure droplet stability*
- iii. Some portion of the antisolvent solution (Component 2) should be miscible with the droplet phase such that diffusion can initiate nucleation/ growth events at the interface of the droplet*
- iv. Components 1 and 2 must be miscible*

Table 5-1 Solvent candidates in which lysozyme has poor solubility as defined by Chen et al^[27].

| Component 1 | Component 2 |
|--------------------|--------------------|
| Ethyl Acetate | Acetonitrile |
| Tert-Butanol | Dimethylformamide |
| Cyclohexane | Dimethyl sulfoxide |
| Methylene Chloride | 1,4 Dioxane |
| Butyl Acetate | Ethanol |
| Hexanol | Methanol |
| Toluene | |

For component 1, only solvents that are immiscible with water were considered. The purpose of this phase is to stabilize the droplets being injected into the system. The droplets must be stable or the agglomeration process cannot proceed. Component 2 controls the kinetics of the crystallization, as its targeted function is to penetrate the lysozyme/water droplet and generate high local supersaturation. Therefore, Component 2 must be miscible with both Component 1 and water. After eliminating several of the solvents for toxicity purposes (through ICH solvent classification), high throughput screenings were conducted combinatorically. Using ethyl acetate as Component 1 and ethanol as component 2, spherical lysozyme agglomerates were observed in a small-scale semi-batch experiment.

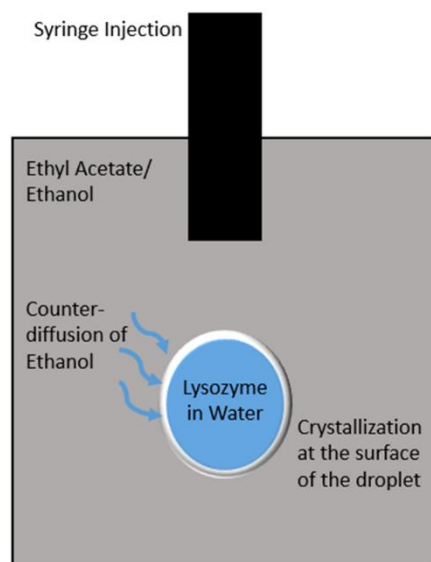


Figure 5.1 Schematic of the droplet injection site, showing the primary mechanism for generating supersaturation at the droplet interface

5.3.2 Materials and Methods for COBC Operation

Two geometrically similar OBCs were used in this crystallization study: the Nitech DN6 and DN15 (Alconbury Weston Ltd) with holdups of 300mL and 1250mL respectively. Lysozyme (Lab grade >99% purity, ~6 μ U/mg activity) was dissolved in deionized water and the

pH in all cases was measured to be approximately 5.0 The bulk phase of the system was a solution containing ethyl acetate (Lab grade >99.5 % purity, Fisher Scientific) and ethanol (Lab grade, 200 proof, Fisher Scientific). The bulk phase was pumped at the bottom of the system using a peristaltic pump (MasterFlex L/S, Cole-Palmer) while the lysozyme solution was injected dropwise by a syringe pump (kd Scientific, Infusion). For experimental consistency, the system in each case was held at 30°C, noting that lysozyme's solubility is only weakly dependent on temperature.^[26] After exiting the OBC, the spherical product was collected using Büchner funnel filtration (4-8 µm particle retention) and allowed to dry in an oven at 35°C for 24 hours.

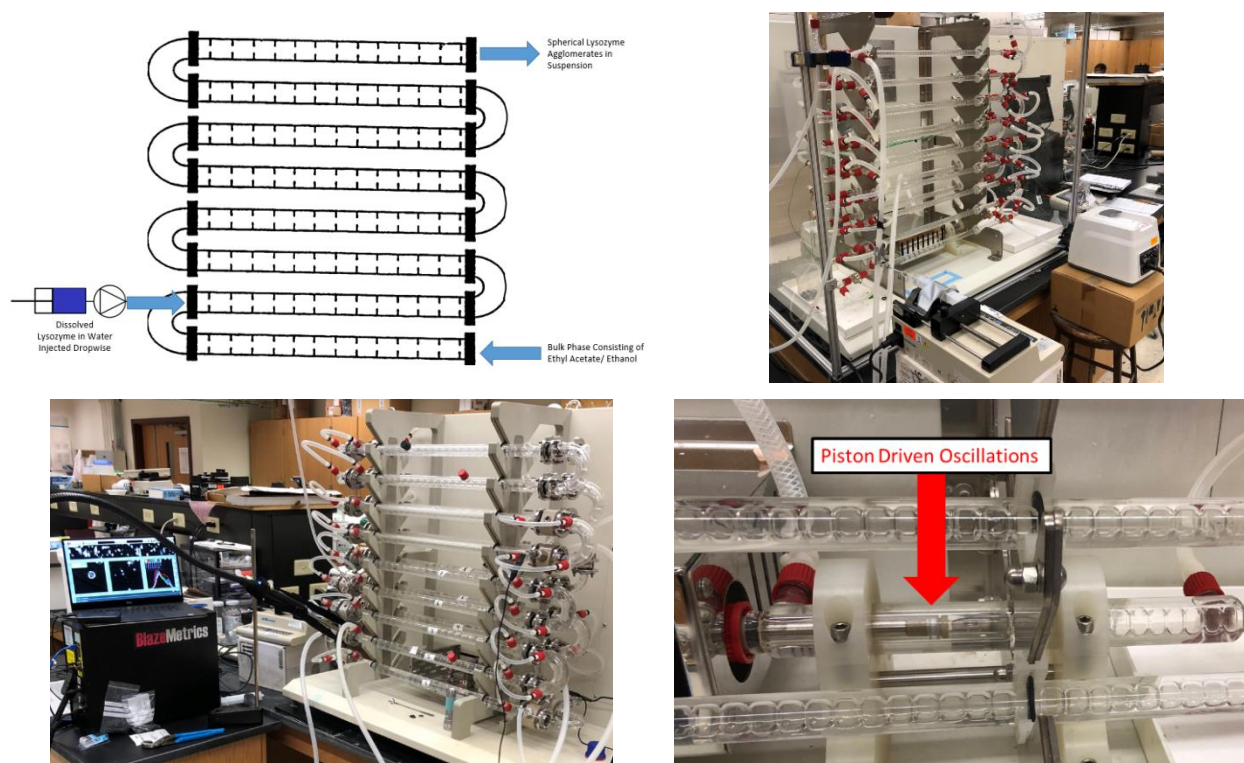


Figure 5.2 Overview of the experimental setup

5.3.3 Spherical Crystallization's Impact on Protein Activity

The Lysozyme Activity Assay Kit by BioVision, Inc. (Cat. No. K236-100) was used to determine the activity of lysozyme samples according to kit instructions. Stock solutions of pre- and post-crystallization lysozyme samples were dissolved in the Lysozyme Activity Buffer provided in the kit at a concentration of 10 mg/mL. Lysozyme is an N-acetylmuramide glycanhydrolase (also known as muramidase), which is a type of hydrolase that acts on glycosidic bonds present in the mucopolysaccharide cell walls of bacteria. It specifically cleaves β -(1-4) glycosidic linkages in the cell wall. The kit works by measuring the ability of the lysozyme in a sample to cleave a synthetic analog of this bond, which yields a fluorescent by-product (4-methylumbelliferone, ex/em = 360/445 nm).

Lysozyme kit substrate + lysozyme \rightarrow cleaved substrate + fluorescent product + lysozyme

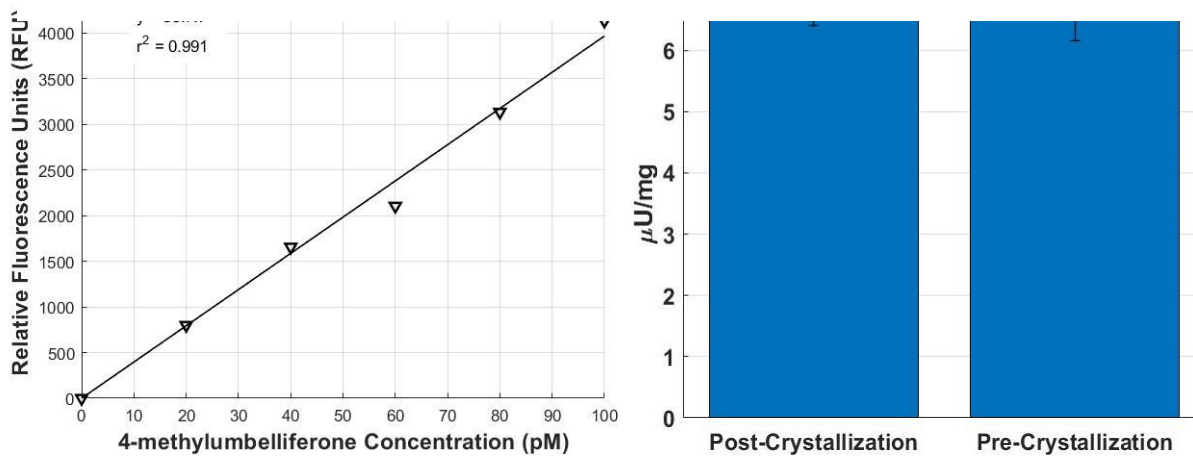


Figure 5.3 Lysozyme activity calibration and result before and after the spherical crystallization process

The fluorescence signals from the lysozyme samples were compared to the 4-MU calibration curve to determine the amount of product formed in a given time (i.e. the activity). From Figure 5.3, the activity of the lysozyme product is the same pre and post crystallization within an acceptable margin of error.

5.3.4 Size Analysis

5.3.4.1 Characterizing Particle Size: Number vs Volume Distributions

The Morphologi 4 (Malvern Panalytical) was used for image-based size analysis because the product was spherical in nature. Roughly 25mg of product was loaded into the auto-dispersing chamber of the unit, before pressurized air (1 bar) dispersed the sample over 60s onto a glass plate. Diascopic illumination was used for optimal contrast in particle detection at 2.5x magnification. Each size distribution was constructed with a minimum of 500k particles. The Morphologi software calculates the circle equivalent diameter from the images and exports the raw data to be used as a number-based size distribution. Characteristically, number-based size distributions emphasize smaller particles because they are weighted equally to their larger equivalents. Knowing this may not be a proper representation of the generated product, the pharmaceutical industry most commonly reports volume-based size distributions. To transform a number-based size distribution into a volume distribution, the following equation from Litster^[28] was used.

$$f_{vi} = \frac{\bar{x}_i^3 f_i}{\sum_j \bar{x}_j^3 f_j \Delta x_j} \quad (2)$$

Note: f_v is the volume-based frequency, f is the number-based frequency, \bar{x} is the mean size of the bin, and Δx is the width of the bin. Figure 5.4 clearly illustrates the difference between the two different types of distributions and the significance in this specific system due to the large number of small agglomerates generated.

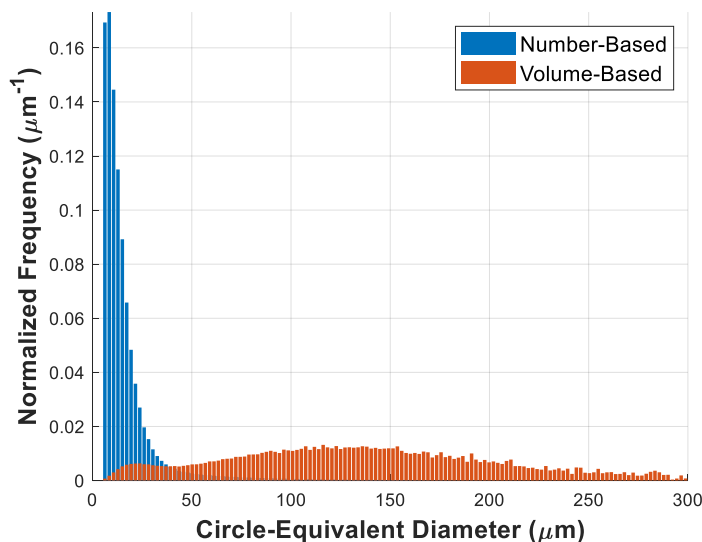


Figure 5.4 Transformation of a number-based CSD to a volume-based CSD and the qualitative effect of the reporting method

When the number distribution is used, the CSD is narrow and the mean is $15.9\mu\text{m}$, but when the volume distribution is used, the CSD is broad (mean: 144.3) due to the larger particles having a higher weighting factor. Because a significant portion of the material lies in these larger particles, volume-based distributions will be reported throughout.

5.3.4.2 Statistical Approach in Determining Appropriate Bins for Particle Size Distributions

The direct output from this image-based size analysis is a list of circle-equivalent diameters that must be appropriated to a specific number of bins that will be representative of the sample. The default method for many software is to set the number of bins (k) equal to the square root of the number of observations ($n^{1/2}$) in the data set. However, in these experiments, the data set is extremely large, leading to an unrealistically large number of generated bins. When there are too many bins for a given data set, the signal to noise ratio is very low. Conversely, when there are too few bins for a given data set, the resulting CSD is coarse, often

lumping bimodality and other key features of the data. As a result, utilizing a statistically relevant approach is imperative for this study.

In statistics, several rules are recommended for determining the appropriate number of bins for a given dataset. In this study, the following four rules were investigated; namely, Sturge, Rice, Scott, and Freedman-Diaconis.

Sturge's Rule

$$k = 1 + \log_2 n \quad (3)$$

Rice's Rule

$$k = 2 * n^{1/3} \quad (4)$$

Scott's Rule

$$k = \frac{\max(f_{vi}) - \min(f_{vi})}{3.5 * \sigma(f_{vi}) * n^{-1/3}} \quad (5)$$

Freedman-Diaconis

$$k = \frac{\max(f_{vi}) - \min(f_{vi})}{2 * IQR(f_{vi}) * n^{-1/3}} \quad (6)$$

Note: σ is the standard deviation and IQR is the interquartile range of the data set. Sturges' rule was derived in 1926 and assumes the data set will be Gaussian in nature (often referred to as the *normal reference rule*). This method inherently tends to oversmooth data and additional bins are necessary if the data set is known to be large. Rice's rule is similar to Sturge's Rule in that it follows the normal reference rule but consistently predicts a larger number of bins required for the same number of observations ($n > 2.6$). Scott's rule, also derived using the *normal reference rule*, incorporates the mean integrated squared error as a bin width predicting parameter. It differs from the previous two methods in that it predicts equally distributed bin widths, rather

than the total number of bins, leading to higher accuracy near the center of the normal density. Similarly, the *Freedman-Diaconis* rule estimates bin widths instead of total number. Instead, however, this rule uses the inter-quartile range of the distribution and a weighting factor of 2 to improve the robustness of a generalized method.

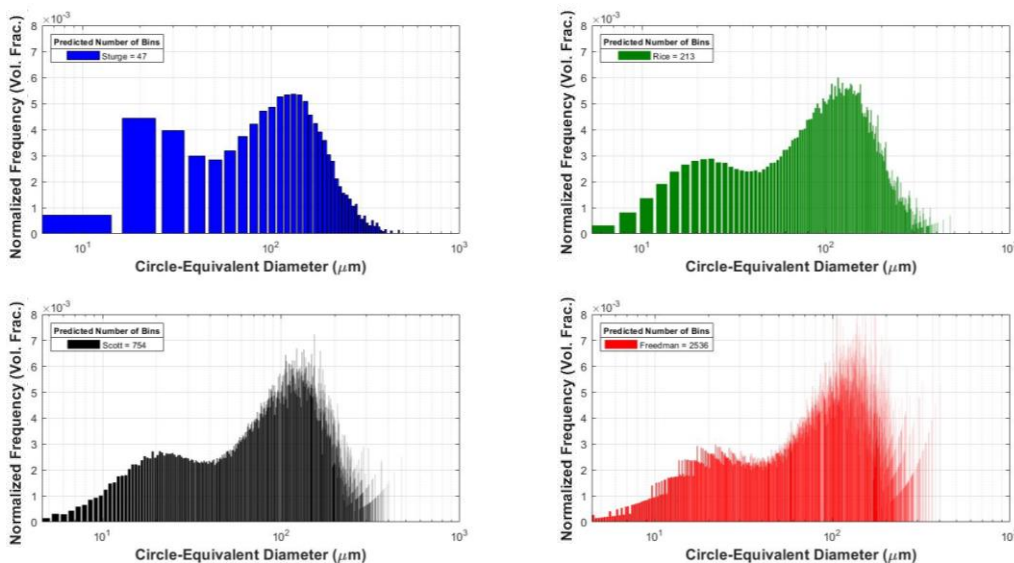


Figure 5.5 Comparison of statistical approaches used to determine appropriate bin widths for CSD reporting

Clearly, the number of bins dramatically influences the representation of the dataset, especially in the case of a bimodal distribution, like that shown in Figure 5.5. When the binning is too coarse (Sturge), information is lost by lumping the true nature of the distribution. Conversely, when the binning is too fine (Freedman), the data set loses its bimodality altogether. One thing to note is that the data becomes very noisy for the larger bin sizes (in the cases of Rice, Scott and Freedman). The data becomes increasingly noisy due to the small number of large particles in the system. Those larger particles represent a large portion of the total volume in the dataset, but do not appear consistently across bin sizes. As a result, nonuniform bin widths

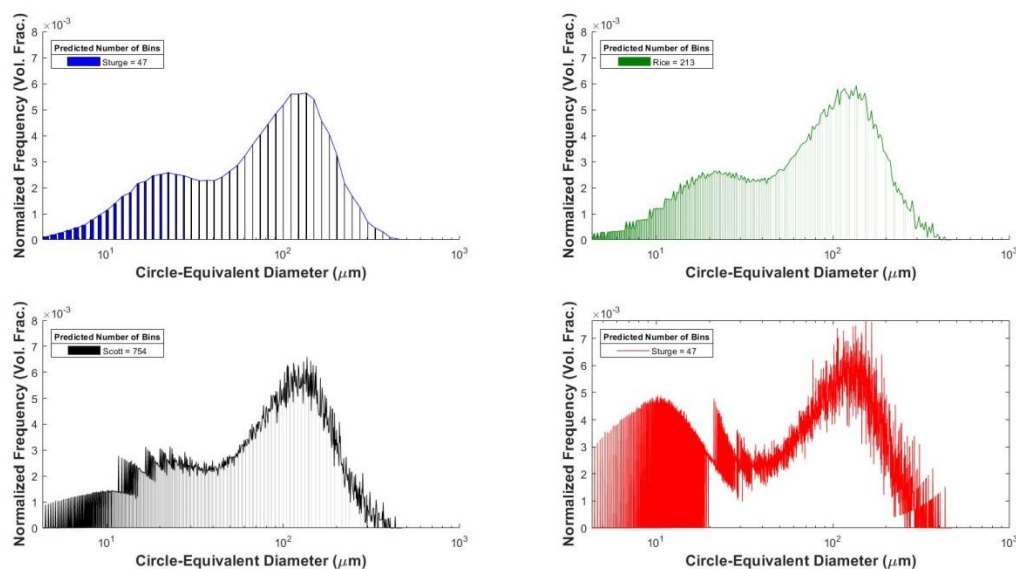


Figure 5.6 Comparison of statistical approaches used to determine appropriate bin widths that increase logarithmically

Figure 5.6 redistributes the bins of the dataset such that the bin widths increase logarithmically, rather than being uniformly spaced. By applying this transformation, the bins for smaller sized particles have higher resolution (their bin widths are smaller), while their larger equivalents have wider bin widths. Because these specific datasets contain a small number of large particles, wider bins dampen the noise in the distribution, leading to more representative end behavior. The Sturge method was selected for this study because logarithmically spacing large numbers of bins dampens the signal to noise in the data set, due to the fast growth behavior of the function. Hereafter, the CSDs presented have been processed identically to Figure 5.6, omitting the bars for clarity in data comparisons.

5.3.5 Determining the Effect of Droplet Size on Crystal Size Distribution

Several process parameters affect the size of the droplets being injected into the COBC system: namely, the injection rate of the droplet solution (\dot{V}), the tip size of the nozzle injecting the droplets (d), the flow rate of the bulk solvents (\dot{F}), and the oscillatory mixing conditions (Re_o). In this study, the effect of changing \dot{F} and Re_o are easily described by holding the other process conditions constant. However, there is a dependency between \dot{V} and d that is less apparent. In ESD based systems, several mechanisms affect the CSD of the product: nucleation, growth, droplet coalescence, and droplet/ agglomerate breakage. The nucleation and growth mechanisms are primarily controlled by the concentration of ethanol in the system, as the diffusivity of the bulk phase into the droplet phase can be tailored accordingly. In the case of the droplets, coalescence events are dominated by the spacing between the droplets as they are injected and their proximity to the wall of the system. As a result, the wall effects of the system will also be discussed by directly comparing the product of the DN6 and DN15 systems. The spacing of the droplets can be described as follows.

$$\frac{\# \text{ of droplets}}{s} \propto \frac{\dot{V}}{d^2 x_c} \quad (7)$$

where x_c is the characteristic size of droplets being produced for the given nozzle tip size (d). In order to keep the spacing between the droplets constant, thereby attempting to normalize the droplet coalescence rate between experiments, x_c must be defined. However, x_c is highly dependent on both material properties (fluid viscosity and density) as well as process conditions (d , \dot{F} , and Re_o). Because the bulk axial flow rate is much larger than the injection speed ($\dot{F} \gg \dot{V}$), x_c is assumed to always be smaller than or roughly equal to d . Equation 7 now becomes

$$\frac{\# \text{ of droplets}}{s} \propto \frac{\dot{V}}{d^3} \quad (8)$$

In a more useful form, equation 8 can also be written as

$$\frac{V_1}{d_1^3} \approx \frac{V_2}{d_2^3} \quad (9)$$

Using this relationship, the spacing of the droplets being injected can be held roughly equal and scaled appropriately between experiments.

5.3.6 Scaleup Between the DN6 and DN15 Systems

In scaling the production of lysozyme agglomerates from lab to pilot scale, several approaches should be considered. Because the supersaturation of the system is depleted within the first couple minutes, the tube length of the system is less significant than the diameter. In scaling by diameter, the production rate of lysozyme will be determined by the number of droplets that can be injected by relating the average droplet diameter to the cross-sectional area of the tube. Following this logic, the wall effects of each system will be characterized using two approaches. The first approach directly scales the process conditions from the DN6 to the DN15, namely keeping both \dot{V} and \dot{F} constant, while tuning the Re_o of each system to be equal. The second approach will consider the effect of tube diameter on the net axial velocity directly related through \dot{F} . By scaling the axial velocity, the injection conditions near the nozzle should also be constant, giving more information regarding the effects of the walls on coalescence events.

5.4 Results and Discussion

Table 5-2 Summary of Experimental Conditions. Note: experiments in bold were performed in the DN15, while all others were performed in the DN6.

| Exp. | Flow Rate (mL/min) | Injection Rate (mL/min) | x_0 (mm) | f (Hz) | C_{EtOH} (Vol %) | $C_{Lysozyme}$ (mg/mL) | Nozzle Diameter (inches) |
|-----------|-----------------------|----------------------------|---------------|-------------|-----------------------|---------------------------|-----------------------------|
| 1 | 22.6 | 0.25 | 25 | 2 | 5 | 30.7 | 1/8 |
| 2 | 22.6 | 0.25 | 25 | 2 | 1 | 30.7 | 1/8 |
| 3 | 22.6 | 0.25 | 25 | 2 | 3 | 30.7 | 1/8 |
| 4 | 22.6 | 0.25 | 25 | 2 | 10 | 30.7 | 1/8 |
| 5 | 22.6 | 0.25 | 15 | 2 | 5 | 30.7 | 1/8 |
| 6 | 22.6 | 0.25 | 20 | 2 | 5 | 30.7 | 1/8 |
| 7 | 22.6 | 0.35 | 25 | 2 | 5 | 30.7 | 1/8 |
| 8 | 22.6 | 0.20 | 25 | 2 | 5 | 30.7 | 1/8 |
| 9 | 22.6 | 0.25 | 25 | 2 | 5 | 15.4 | 1/8 |
| 10 | 22.6 | 0.25 | 25 | 2 | 5 | 46.1 | 1/8 |
| 11 | 22.6 | 0.25 | 15 | 1.3 | 5 | 30.7 | 1/8 |
| 12 | 141.25 | 0.25 | 15 | 1.3 | 5 | 30.7 | 1/8 |
| 13 | 22.6 | 0.25 | 15 | 1.3 | 5 | 30.7 | 1/16" |
| 14 | 22.6 | 0.25 | 15 | 1.3 | 5 | 30.7 | 5/32" |

5.4.1 Steady State Operation

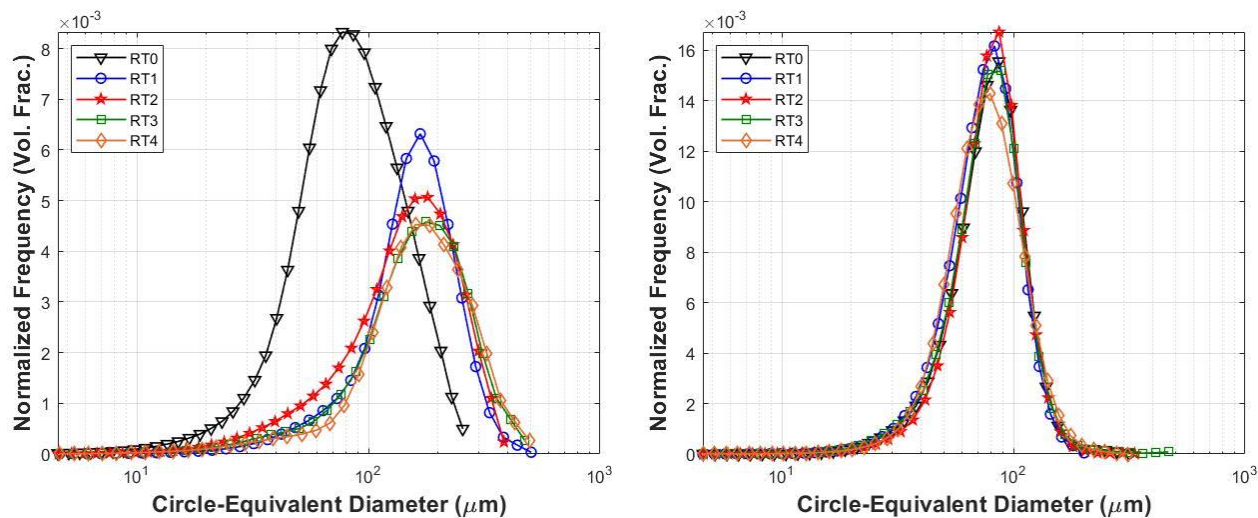
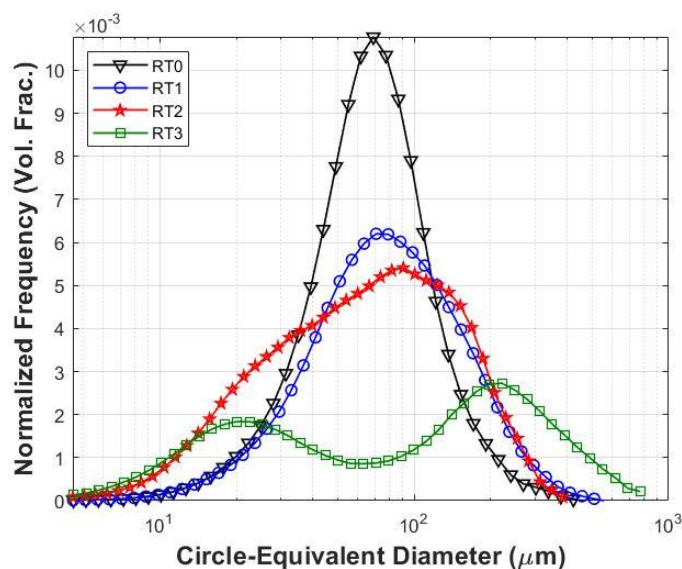


Figure 5.7 Determining steady state product generation in the DN6 (left) and DN15 (right). The data shown corresponds to Exp 1 and 12 respectively.

In order to properly understand the dynamics of continuous systems, a steady state must first be reached. Figure 5.7 (left) illustrates the DN6 reaching a steady state somewhere between RT2 and RT3, while Figure 5.7 (right) shows the DN15 reaching a steady state over a much shorter timestep. Note that RT0 is not a reflection of the experiment startup. Instead, it is the time point at which the entire reactor has product, with each subsequent RT using RT0 as a reference. In this example, the DN15 converges to a steady state much faster than the DN6 because the relative turbulence generated by the pump is much larger than that of the piston. When operating under piston-dominated conditions, backmixing plays a much larger role. These examples are ideal cases. In some instances, dynamic fouling can lead to bimodal size distributions and even clog the system, leaving it inoperable.

5.4.2 Non-Steady State Operation



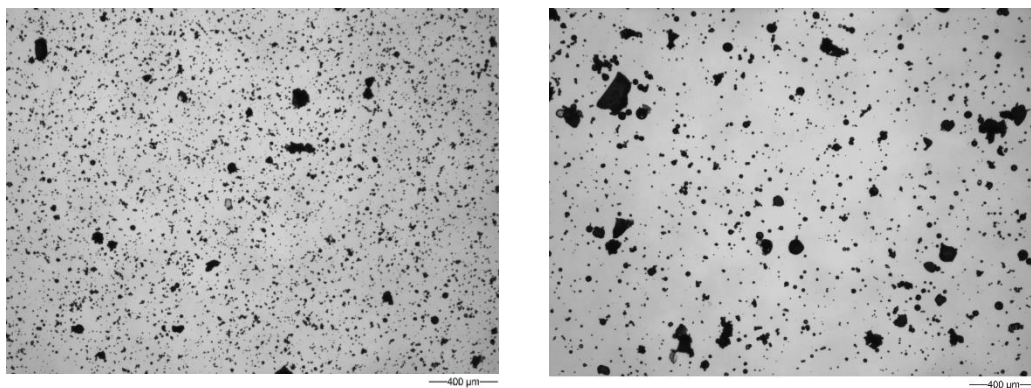


Figure 5.8 Consequences of encrust formation on process steady state as measured by CSDs over time (top) and microscope images (bottom). Note: the bottom left image is from RT2 and the bottom right image is from RT3. The data shown corresponds to Exp 6.

Figure 5.8 illustrates a case where an ideal lognormal distribution (RT0) diverts into a nonideal bimodal distribution (RT3). Qualitatively, the OBC is building a fouled layer near the injection site of the droplets; the point where the nucleation rate is the highest. When the fouled material layers to some critical thickness, pieces break off and continue to agglomerate. Ultimately, this leads to a dynamic steady state where fouled material is simultaneously deposited/ chipped off, leading to a bimodal distribution of the product. This phenomenon occurs most often when there is not enough suspension energy in the system to keep the droplets from settling.

5.4.3 Blaze Microscopy vs Scanning Electron Microscopy (SEM)

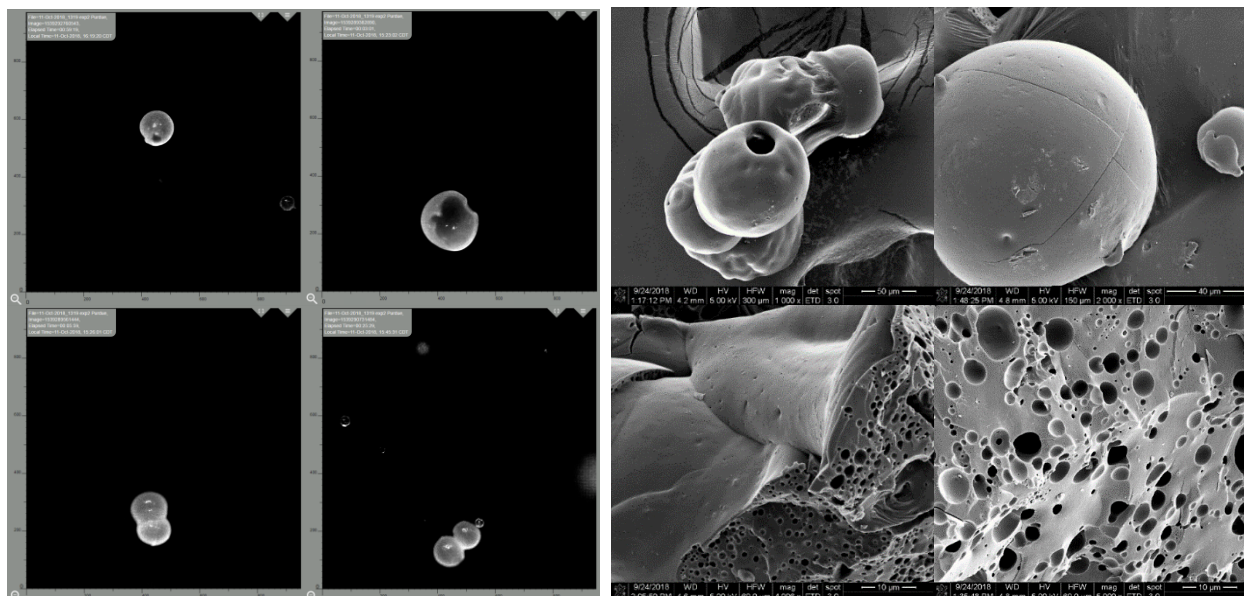


Figure 5.9 Comparison of in-situ Blaze Microscopy (left) vs. offline SEM (right) in characterizing the spherical lysozyme product

The Blaze 900 was used to capture high definition images of the droplets at the injection site. Several interesting phenomena were observed in describing a mechanistic understanding of the process. In addition to the online Blaze microscopy, offline SEM was performed for further analysis. The Blaze images show the early stages of crystallization, namely the existence of a solid shell and liquid core of the droplet. Together, with the SEM images, the fate of the water inside of the droplet can be described. From Figure 5.9, a pore size distribution is observed after slicing an agglomerate. As the droplet undergoes crystallization, localized high-pressure regions extrude the liquid core of the droplet, generating a series of pores. If these channels become unstable, they can collapse into large holes as shown in both the Blaze and SEM images. This phenomenon occurs somewhat regularly in the product. If this property is considered significant, the pressurization of the droplets might be controlled by the amount of ethanol in the bulk phase, due to its control of the local supersaturation.

Ideal ESD-based crystallization would generate very uniform spherical product. However, due to the oscillating nature of this system, there tends to be an abundance of coalescence between the droplets prior to the liquid/solid transition. To limit these events, droplet injection spacing as well as the ratio of droplet diameter to reactor diameter should be controlled. Accumulating particles in the vortices of the baffles increases the propensity for droplet coalescence and is influenced by reactor wall effects.

5.4.4 Ethanol Concentration in the Bulk Phase

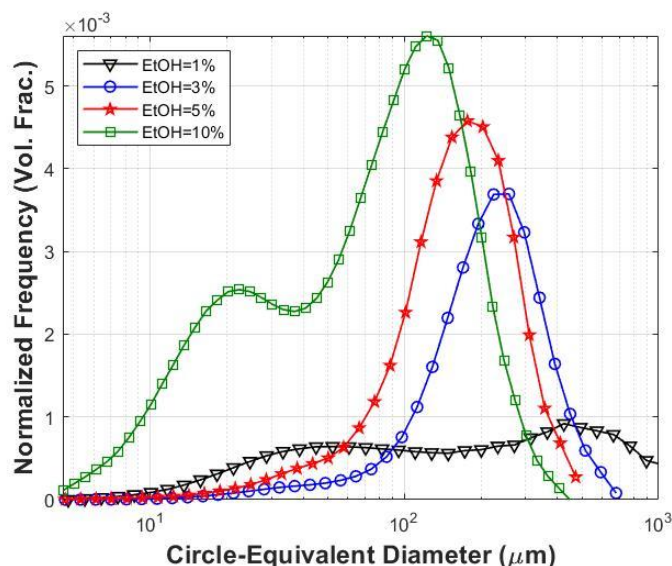


Figure 5.10 The effect of varying ethanol concentration on crystal size. The data corresponds to Exp 2, 3, 1, and 4 respectively.

The concentration of ethanol in the bulk phase controls the initial nucleation rate at the droplet boundary. As the ethanol diffuses into the center of the droplet, the lysozyme crystals grow and agglomerate, while the water inside of the droplet extrudes to the boundary due to localized high-pressure regions. Both nucleation and growth depend on the local supersaturation. From Figure 5.10, an optimal concentration of ethanol exists for this process. When there is not enough ethanol (EtOH=1%) in the system, the droplets do not crystallize fast enough, leading to uncontrollable droplet coalescence events. By the time the droplets begin crystallizing, the

intended droplet size distribution has shifted significantly, leading to an abnormal CSD. When there is too much ethanol (EtOH=10%) in solution, nucleation occurs very quickly at the droplet surface. With very small particles at the droplet surface, while maintaining a liquid core, the droplet becomes unstable, increasing the likelihood that these particles exit into the bulk phase. With an uncontrolled amount of droplet breakup, a bimodal distribution develops, as seen in Figure 5.10. As in the work by Peña^{[13],[29]} and others, there exists an optimal operating region for the amount of binder in solution. For the case of lysozyme, both the 3% and 5% ethanol experiments yielded acceptable CSDs. The size of the crystals generated from each of these cases similarly depends on the size of the primary particles formed inside of the droplet, as well as the droplet stability during the initial nucleation/ growth stages.

5.4.5 Concentration of Lysozyme in Droplets

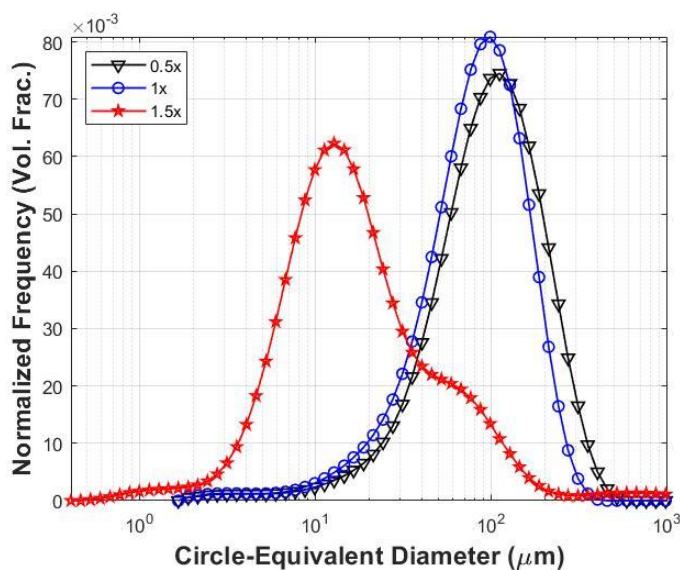


Figure 5.11 The effect of changing the concentration of lysozyme in the droplet phase. Note: 0.5x corresponds to 15.4 mg/mL, 1x corresponds to 30.7 mg/mL, and 1.5x corresponds to 46.1 mg/mL. The data corresponds to Exp 9, 1 and 10 respectively

The concentration of lysozyme in the droplet phase is a critical parameter for crystallization kinetics. However, unlike traditional crystallizations, ESD-based droplet crystallization has a second mode of action which can dominate the system. Changing the droplet concentration from 1x to half concentration does not significantly impact the product formed. This result implies that the crystallization kinetics are diffusion limited in this concentration range. In other words, with the amount of ethanol present in solution, the system is limited by the diffusivity of the ethanol, that is, the rate at which ethanol is able to permeate the droplet. In these cases, the local supersaturation at the droplet boundary is dominated by the ethanol, not the amount of lysozyme in solution. However, this result does not imply that these two products are the exact same. Physical properties such as average agglomerate mass and compactness were not included in this study, but would likely vary under these process conditions. When the concentration of lysozyme increases to 1.5x, the system's supersaturation is now dominated by the lysozyme in solution, rather than the diffusivity of the ethanol. As a result, high local supersaturation drives excessive nucleation at the droplet boundary early in the process, leading to droplet instability. When the droplet is primarily still liquid and the shell is composed of small particles, the small particles are likely to escape the droplet during inter-droplet collisions or collisions with the system walls. As a result, a large number of small agglomerates form. The result is a bimodal distribution with the majority of the agglomerates in the smaller size domain. However, a number of the larger agglomerates fall in the same range as the 0.5x and 1x cases, implying that a number of those agglomerates were also in the diffusion limited region.

5.4.6 Piston-Driven Suspension Energy

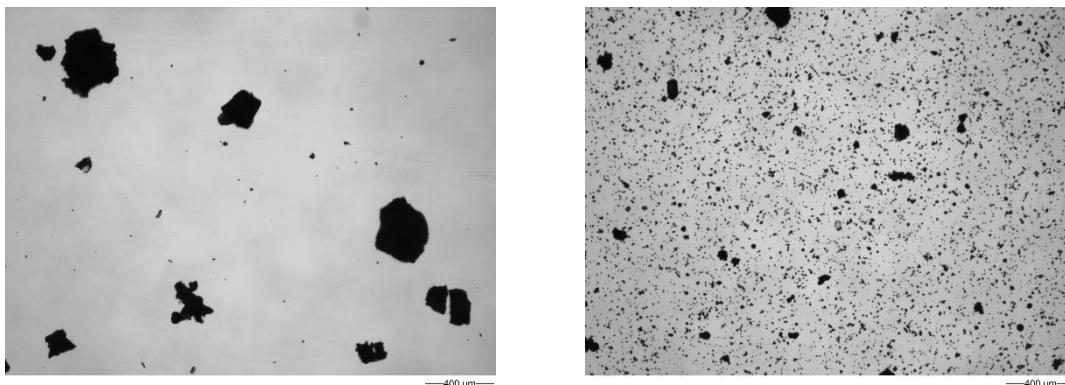
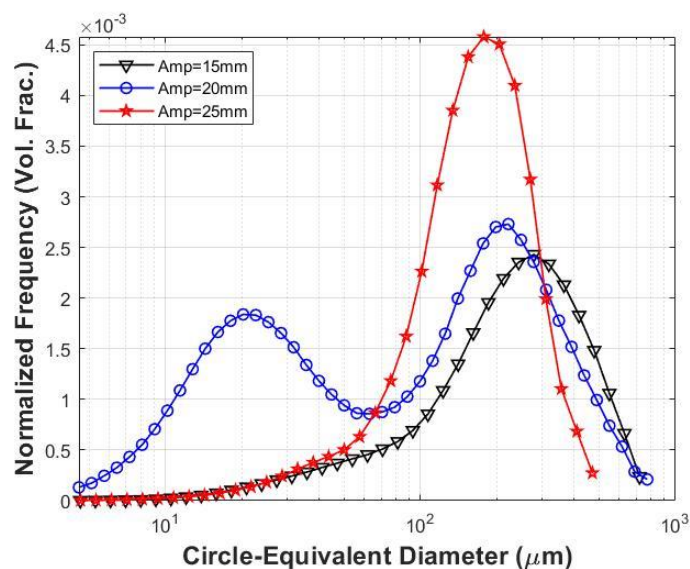


Figure 5.12 The impact of varying piston driven suspension energy on the CSD. The data corresponds to Exp 5, 6, and 1 respectively (top) while the pictures correspond to Exp 5 and 6 (bottom).

Proper droplet/ solid suspension must be maintained throughout the crystallization process. When particles settle or initiate fouling in the system, abnormalities can be seen in the product before the system eventually clogs. Two modes of action contribute to the overall suspension energy in the system; namely, the turbulence generated by the oscillating piston and also that from the peristaltic pump. Because the net flow rate was held constant in order to maintain a consistent nominal residence time, the suspension energy was varied by changing piston amplitude. The piston amplitude was chosen instead of the frequency because several

authors (Ni, Kacker, Oliva, and others^{[9],[30],[31]}) have shown that its contributions are much more significant to overall flow dynamics. From Figure 5.12, the lowest tested piston amplitude (Amp=15mm) has a large mean particle size and the CSD is quite skewed. Qualitatively, even at the initial stages, the injected droplets were not suspended well, leading to a large amount of fouling in the system. The droplets immediately settled to the bottom of the system and coalesced prior to initial nucleation events. This fouled layer dominated the system, as no individual droplets were observed. The material collected at the outlet was very large and crude, undoubtedly coming out as broken pieces from the parent tube encrust. As the piston oscillations increased (Amp=20mm) in the subsequent experiment, fouling again could be observed, but the overall layer was smaller than its 15mm predecessor. With more oscillation energy, the droplets were better suspended, but some settling still occurred. The fouled layer was smaller because the breakage rate was higher from the increased piston energy. As seen in Figure 5.12, the resulting distribution was bimodal, as some spherical particles were able to exit the system in combination with smaller pieces of chipped fouled material. Lastly, as the piston amplitude was increased to 25mm, the fouling in the system was minimized and the droplets suspension improved significantly. The resulting CSD indicated a significant improvement in the process. Note: the piston amplitude was not increased further because 25mm is the limit of operation in the system software.

5.4.7 Lysozyme Injection Rate

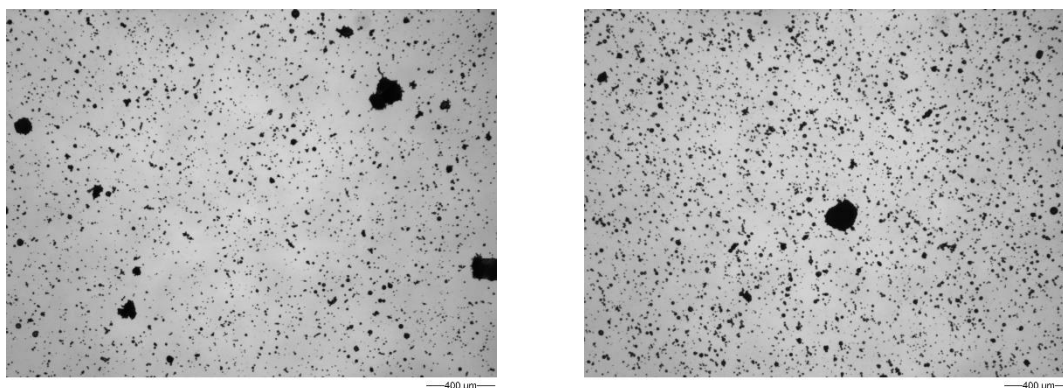
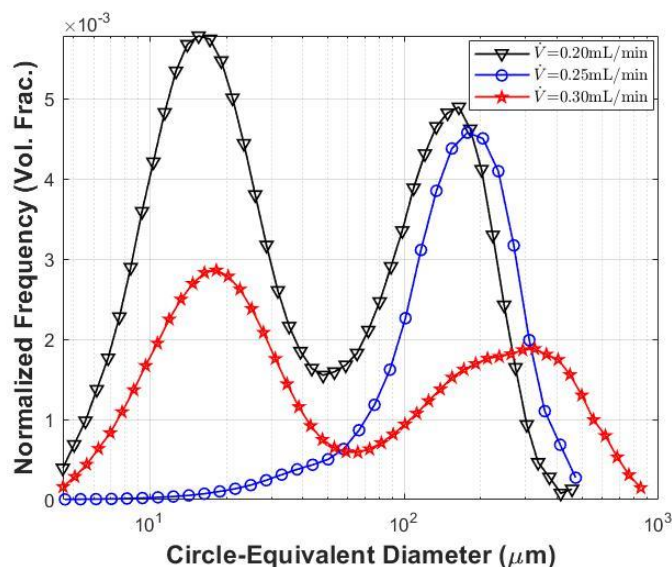


Figure 5.13 Variable lysozyme droplet injection rates and their effect on the product's CSD. The data corresponds to Exp 8, 1, and 7 respectively (top) while the pictures correspond to Exp 8 and 7 (bottom).

In deciding an appropriate droplet injection speed, several phenomena must be considered. From Figure 5.13, if the injection speed is too low, the system generates a bimodal product. This bimodality could result from the presence of satellite droplets breaking off from the mother droplet during injection. Qualitatively, there are a large number of small agglomerates in the product. As the injection speed of the droplets increases, the number of small agglomerates significantly decreases. However, past some threshold, the injection speed is too fast, inducing fouling at the injection site. This fouled layer leads to bimodality, as pieces of the

layer get chipped off while surface layering simultaneously occurs. As a result, there exists a delicate balance in choosing an appropriate injection speed. Note that in the larger system, the injection speed can be increased significantly higher before intense fouling occurs, implying that this decision is both process as well as system dependent.

5.4.8 Effect of Nozzle Tip Size on CSD

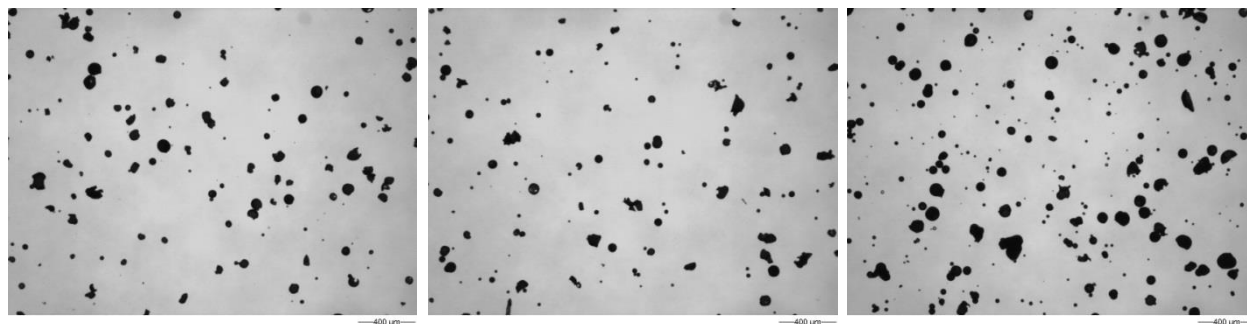
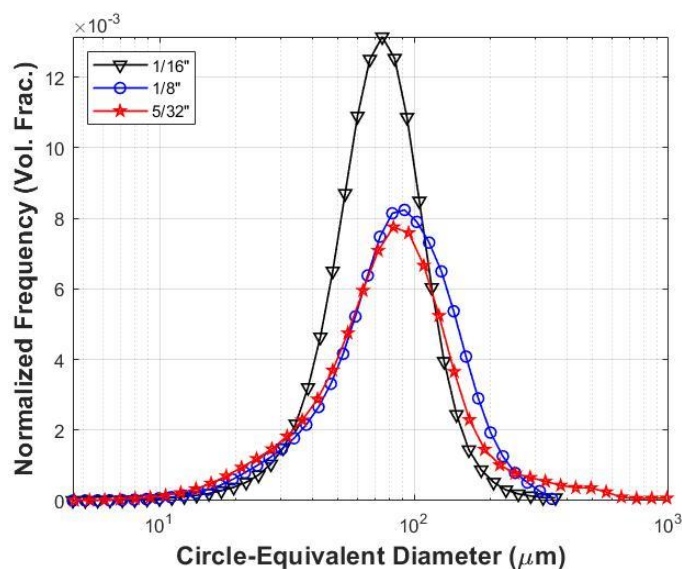


Figure 5.14 The effect of varying the injection nozzle tip size on the product's CSD. The data and pictures correspond to Exp 13, 11, and 14 respectively.

The size of droplets in the system dramatically impacts the size of agglomerates formed, as seen through the previous case studies. In this case study, the nozzle tip size was changed to study the impact on the droplet size and thereby controlling the overall agglomerate size. The

droplet injection rate to diameter ratio $\left(\frac{\dot{V}}{d^3}\right)$ was scaled as described in the methods section. From Figure 5.14, changing the nozzle tip size seems to have no significant impact on the CSD. Two process parameters impacting the injection site could be responsible for this result, namely the Re_o and the net axial velocity. From the previous case studies, the injection environment drastically impacts the fate of the droplet downstream in the system. In this case, the net axial velocity and Re_o , do not allow fully developed droplets to be injected into the system. As a result, the critical size of droplets being formed (x_c) is limited by the injection environment, thereby limited the size of agglomerates that can form. To truly control the size of droplets in the system, upstream droplet generation (for example, using a membrane) could be implemented before adding the droplets to the oscillatory environment of the COBC.

5.4.9 Scale-Up and Geometric Considerations

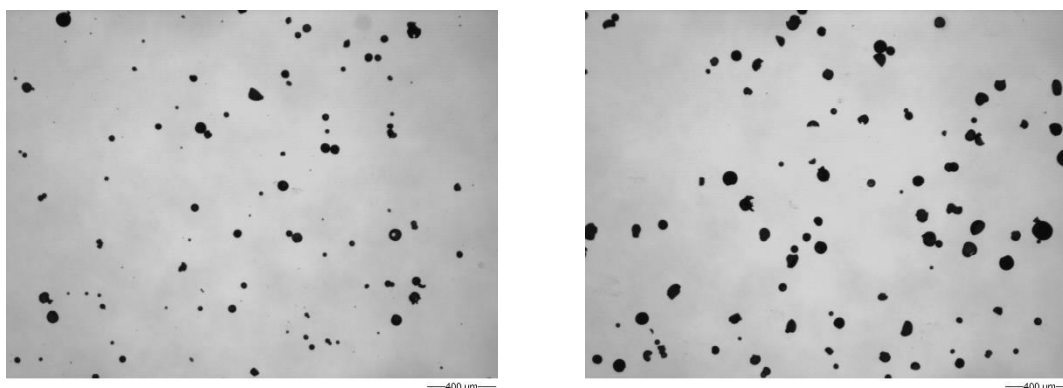
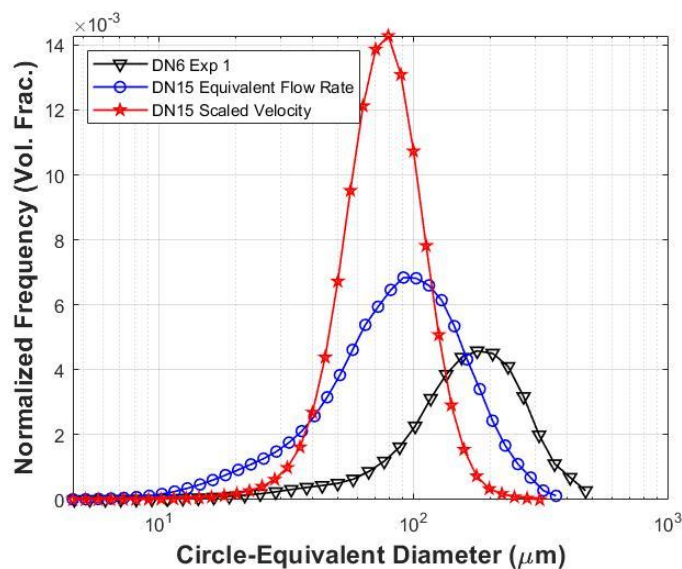


Figure 5.15 Two different approaches for scaling the production of lysozyme. The data corresponds to Exp 1, 11, and 12 respectively, while the pictures correspond to Exp 11 and 12 (bottom).

As described in the methods section, two approaches were investigated in regards to scaling the lysozyme process. The first approach directly translates the process conditions used from Exp 1 in the DN6 system to the DN15, except the piston oscillations were scaled to keep the Re_o constant. The results from this approach are represented by the blue curve in Figure 5.15. There are several notable characteristics in describing the transition from the black curve to the blue. The product produced from the DN6 is notably larger than that formed by the DN15,

suggesting that the rate of droplet coalescence is much higher due to wall effects. Another noteworthy observation is that the shape of these curves is very similar, suggesting that the Re_o plays a significant role in determining the quality of product formed. Both of these results show a number of smaller agglomerates, with the bulk of the product being in a larger size domain. These smaller particles are likely formed due to droplet settling and fouling, since the turbulence is primarily piston driven.

When the axial velocity is scaled to be equivalent (i.e. accounting for the change in system diameter), the resulting product is more uniform. Scaling the axial velocity to be equivalent, significantly increases pump driven turbulence, downplaying the effect of piston driven backmixing in the system. In reference to each DN15 experiment, the spacing between droplets is larger, decreasing the likelihood for coalescence, thereby narrowing the CSD. Because the kinetics of this process are extremely fast, generating turbulence with a pump is preferred. Piston driven turbulence is beneficial when long residence times are required, but often leads to significant backmixing. As a result, scaling this process should prioritize minimizing wall effects (increasing the system diameter, not increasing the length of the system) and maximizing the system's suspension energy.

5.5 Conclusions

In this study, the continuous crystallization of lysozyme was evaluated in terms of process sensitivity and scalability. Typically, supersaturation is the most critical parameter in crystallization. However, due to the nature of this application occurring at the droplet interface, operating in certain domains led to diffusion limiting the crystallization kinetics. As a result, the diffusivity of component 2 can be tailored to control process kinetics and final product CSD, keeping in mind that the concentration of API in the droplet also plays a role.

Droplet suspension was determined to be the most significant operating parameter, as it often induces encrust formation, which negatively affects the final product quality. The early life of the droplet in the system is critical, as the droplet is most susceptible to settling and coalescence in the purely liquid stages. As nucleation occurs at the droplet surface, the propensity for coalescence significantly decreases, as elastic collisions become dominant. Dynamic encrust formation and breakage drastically impacts the shape of the CSD and should be avoided to ensure process longevity.

In addition to analyzing system parameters, scale up was also evaluated using the two aforementioned techniques. While directly translating the process parameters from the DN6 to the DN15 proved to give similar product, scaling the axial velocity to the larger system gave a more uniform CSD. Because the crystallization kinetics occur on the order of minutes, not hours, scaling the OBC should be based on tube diameter, not system length. Assuming plug flow operation, time and length in the OBC become one in the same. As a result, for this process, limiting droplet coalescence with proper injection spacing and minimal wall effects is essential to form uniform, spherical product.

Acknowledgements

The authors thank the Department of Education for the funding support through the Graduate Assistance in Areas of National Need (GAANN) program.

Notes

The authors declare no competing financial interest.

5.6 References

- [1] J. G. Elvin, R. G. Couston, and C. F. van der Walle, "Therapeutic antibodies: Market considerations, disease targets and bioprocessing," *Int. J. Pharm.*, vol. 440, pp. 83–89, 2013.
- [2] Gary Walsh, "Biopharmaceutical benchmarks 2010," *Nat. Biotechnol.*, vol. 28, no. 9, 2010.
- [3] S. Sommerfeld and J. Strube, "Challenges in biotechnology production - Generic processes and process optimization for monoclonal antibodies," *Chem. Eng. Process. Process Intensif.*, vol. 44, no. 10, pp. 1123–1137, 2005.
- [4] S. Kozlowski and P. Swann, "Current and future issues in the manufacturing and development of monoclonal antibodies," *Adv. Drug Deliv. Rev.*, vol. 58, no. 5–6, pp. 707–722, 2006.
- [5] U. Gottschalk, "Bioseparation in antibody manufacturing: The good, the bad and the ugly," *Biotechnol. Prog.*, vol. 24, no. 3, pp. 496–503, 2008.
- [6] A. A. Shukla, B. Hubbard, T. Tressel, S. Guhan, and D. Low, "Downstream processing of monoclonal antibodies-Application of platform approaches," *J. Chromatogr. B Anal. Technol. Biomed. Life Sci.*, vol. 848, no. 1, pp. 28–39, 2007.
- [7] J. Thömmes and M. Etzel, "Alternatives to chromatographic separations," *Biotechnol. Prog.*, vol. 23, no. 1, pp. 42–45, 2007.
- [8] J. Grey and D. Thompson, "Challenges and opportunities for new protein crystallization strategies in structure-based drug design," *Drug Discov.*, vol. 5, no. 11, pp. 1039–1045, 2011.

- [9] J. A. Oliva, K. Pal, A. Barton, P. Firth, and Z. K. Nagy, “Experimental investigation of the effect of scale-up on mixing efficiency in oscillatory flow baffled reactors (OFBR) using principal component based image analysis as a novel noninvasive residence time distribution measurement approach,” *Chem. Eng. J.*, vol. 351, no. May, pp. 498–505, 2018.
- [10] V. Cherezov *et al.*, “High-Resolution Crystal Structure of an Engineered Human β_2 -Adrenergic G Protein–Coupled Receptor,” *Science (80-.)*, vol. 318, no. November, pp. 1258–1265, 2007.
- [11] N. E. Chayen, “Optimization techniques for automation and high throughput,” *Methods Mol. Biol.*, vol. 363, pp. 175–190, 2007.
- [12] H. Yang, P. Peczulis, P. Inguva, X. Li, and J. Y. Y. Heng, “Continuous protein crystallisation platform and process: Case of lysozyme,” *Chem. Eng. Res. Des.*, vol. 136, pp. 529–535, 2018.
- [13] R. Peña, J. A. Oliva, C. L. Burcham, D. J. Jarmer, and Z. K. Nagy, “Process Intensification through Continuous Spherical Crystallization Using an Oscillatory Flow Baffled Crystallizer,” *Cryst. Growth Des.*, 2017.
- [14] P. Stonestreet and A. P. Harvey, “A Mixing-Based Design Methodology for Continuous Oscillatory Flow Reactors,” *Chem. Eng. Res. Des.*, vol. 80, no. January, pp. 31–44, 2002.
- [15] K. Pitt *et al.*, “Particle design via spherical agglomeration: A critical review of controlling parameters, rate processes and modelling,” *Powder Technol.*, vol. 326, pp. 327–343, 2018.
- [16] J. Varshosaz, N. Tavakoli, and F. A. Salamat, “Enhanced dissolution rate of simvastatin using spherical crystallization technique,” *Pharm. Dev. Technol.*, vol. 16, no. 5, pp. 529–535, 2011.

- [17] A. N. Usha, S. Mutalik, M. S. Reddy, A. K. Ranjith, P. Kushtagi, and N. Udupa, "Preparation and, in vitro, preclinical and clinical studies of aceclofenac spherical agglomerates," *Eur. J. Pharm. Biopharm.*, vol. 70, no. 2, pp. 674–683, 2008.
- [18] M. Dixit, "Spherical Agglomeration of Indomethacin by Solvent Change Method.," *Int. J. Pharma. Res. Dev.*, vol. 4, no. 9, pp. 33–43, 2010.
- [19] A. Sano, T. Kuriki, Y. Kawashima, H. Takeuchi, T. Hino, and T. Niwa, "Particle Design of Tolbutamide by the Spherical Crystallization Technique," *Chem. Pharm. Bull.*, vol. 40, no. 11, pp. 3030–3035, 1992.
- [20] A. F. Blandin, D. Mangin, A. Rivoire, J. P. Klein, and J. M. Bossoutrot, "Agglomeration in suspension of salicylic acid fine particles: Influence of some process parameters on kinetics and agglomerate final size," *Powder Technol.*, vol. 130, no. 1–3, pp. 316–323, 2003.
- [21] H. Zhang, Y. Chen, J. Wang, and J. Gong, "Investigation on the spherical crystallization process of cefotaxime sodium," *Ind. Eng. Chem. Res.*, vol. 49, no. 3, pp. 1402–1411, 2010.
- [22] P. Saini, A. Kumar, and S. Visht, "Spherical Agglomeration : A Novel Technique Of Particulate Modification & Developing Niche Drug Delivery System," *Ijbr*, vol. 6, no. 2, pp. 86–101, 2013.
- [23] Y. Kawashima, M. Imai, H. Takeuchi, H. Yamamoto, K. Kamiya, and T. Hino, "Improved flowability and compactibility of spherically agglomerated crystals of ascorbic acid for direct tableting designed by spherical crystallization process," *Powder Technol.*, vol. 130, no. 1–3, pp. 283–289, 2003.

- [24] S. Mahanty, J. Sruti, C. N. Patra, and M. E. B. Rao, "Particle Design of Drugs by Spherical Crystallization Techniques," *Int. J. Pharm. Sci. Nanotechnol.*, vol. 3, no. 2, pp. 912–918, 2010.
- [25] S. Zhang, C. Guivier-Curien, S. Veessler, and N. Candoni, "Prediction of sizes and frequencies of nanoliter-sized droplets in cylindrical T-junction microfluidics," *Chem. Eng. Sci.*, vol. 138, pp. 128–139, 2015.
- [26] E. L. Forsythe, R. A. Judge, and M. L. Pusey, "Tetragonal chicken egg white lysozyme solubility in sodium chloride solutions," *J. Chem. Eng. Data*, vol. 44, no. 3, pp. 637–640, 1999.
- [27] J. T. Chin, S. L. Wheeler, and A. M. Klibanov, "On protein solubility in organic solvent," *Biotechnol. Bioeng.*, vol. 44, no. 1, pp. 140–145, 1994.
- [28] J. Litster, *Design and Processing of Particulate Products*. 2016.
- [29] R. Peña and Z. K. Nagy, "Process Intensification through Continuous Spherical Crystallization Using a Two-Stage Mixed Suspension Mixed Product Removal (MSMPR) System," *Cryst. Growth Des.*, vol. 15, no. 9, pp. 4225–4236, 2015.
- [30] X. Ni, M. R. Mackley, A. P. Harvey, P. Stonestreet, M. H. I. Baird, and N. V. Rama Rao, "Mixing Through Oscillations and Pulsations—A Guide to Achieving Process Enhancements in the Chemical and Process Industries," *Chem. Eng. Res. Des.*, vol. 81, no. 3, pp. 373–383, 2003.
- [31] R. Kacker, S. I. Regensburg, and H. J. M. Kramer, "Residence time distribution of dispersed liquid and solid phase in a continuous oscillatory flow baffled crystallizer," *Chem. Eng. J.*, vol. 317, pp. 413–423, 2017.

6. COMPARTMENTAL MODELING OF CONTINUOUS OSCILLATORY BAFFLED CRYSTALLIZER (COBC) SYSTEMS AND THE EFFECT OF SCALE UP ON HYDRODYNAMICS

Reproduced with permission from Attila Egedy^{1*}, Joseph A. Oliva², Botond Szilágyi², Zoltán Nagy². Submitted to *Journal of Chemical Engineering and Processing: Process Intensification*, in review.

¹University of Pannonia, Faculty of Engineering, Department of Process Engineering, H-8200, Veszprém, 10th Egyetem Str., +3688624352, egedya@fmt.uni-pannon.hu

²Davidson School of Chemical Engineering, Purdue University, West Lafayette 47907-2100, USA

6.1 Abstract

Compartment models (CMs) are widely used to capture typical hydrodynamic features of systems with generally low computational costs. The main building blocks of the CMs are continuous stirred tank reactor (CSTR) and plug flow reactor (PFR) models. In this study, the hydrodynamics of two laboratory scale continuous oscillatory baffled crystallizer (COBC) systems were investigated: the commercially available DN15 and a scaled down version known as the DN6. CM structures were identified based on residence time distribution (RTD) measurements for both the DN6 and DN15 systems. To attain a more accurate CM calibration, individual piston and pump flowrates, in addition to simultaneous piston and pump action, were thoroughly analyzed.

The behavior of the systems proved to vary based on the oscillation amplitudes and frequencies, so the number of compartments required for an adequate model was identified based on a variety of operating conditions. It is shown that adaptive CMs are needed to capture the

measured RTD characteristics over a broad piston operation range. The model was validated using datasets outside of the calibration. Both the RTD curves and the calculated dispersion coefficients follow similar trends in the DN6 and DN15 systems. This enabled a generalization of the CM structure (number of CSTR elements as a function of operating conditions) for the DN6 and DN15 systems for scale-up applications.

Keywords: COBC, Compartmental model, oscillatory flow, residence time distribution

6.2 Introduction

Mathematical modeling is widely used to enhance process design and development by reducing the number of experiments required to determine an effective operating space. In chemical engineering, the simplest reactor models are continuously stirred tank reactors (CSTR) and ideal plug flow reactors (PFR). Due to the very low computational cost associated with the CSTR and PFR characteristic equations, these are ideal for on-line control and optimization applications, where the simulation time is paramount.

These simple models, however, are generally not able to describe the real hydrodynamics of large scale processes with complex geometries. Full 3D Computational Fluid Dynamics (CFD) models with high precision calculations are ideal for those tasks, but the runtime is high, and often times, the complexity level of CFD models is not required. Generally speaking, a tradeoff exists between precision and computational runtime. CMs utilize simple models as building blocks and are an excellent way to approximate complex hydrodynamics with significantly lower computational demand than their CFD counterparts.

CMs use at least two basic building blocks (compartments), based on hydrodynamic characteristics. That is, a simple CM of a stirred vessel can be created by considering the region near the impeller as one (high velocity) compartment, and the remaining parts of the vessel as a

second, low velocity, compartment. However, the number of compartments considered is heavily dependent on the complexity and the dimensions of the system. The application of CMs are vast, from neuroscience^[1], marine research^[2], biology^[3], pharmaceuticals^[4], medicine^[5], bioenergetics^[6], epidemics^[7], fire safety^[8], environmental pollution^[9] etc.

One challenge in developing CMs is determining an appropriate number of compartments and the respective volume for each compartment. One technique is to divide the whole device based on specific hydrodynamic conditions. For example, in a catalytic PFR, the longer pipe segments can be identified as PFR compartments and the catalyst bed can be modeled as CSTR compartments. The volume of each compartment can be derived from the real system or can be identified based on experimental data. Additional compartments can be considered if backflow or recirculation were to be implemented. These features can be mixers or distributors and can be used for stream handling (mixing different streams together or distributing them).

Residence time distributions (RTD) are excellent experimental data for identifying the structure of a compartment model^[10], even in multi-inlet systems^[11], as they define characteristic flow conditions with geometric considerations. A second technique for the identification of CM structure and the interconnectivity between the compartments is data mining (e.g. clustering)^[12]. Another clustering technique is related to Delafosse^[14], who modelled the mixing within bioreactors by combining CFD mesh elements with similar velocity values. These authors pointed out that the defining compartments can be based on the uniformity of certain model parameters. The third common technique is heuristic determination, which can be applied even if there is limited experimental information about the system^[15].

Continuous oscillatory baffled crystallizers (COBC) are getting more attention with the quick spread of continuous technologies in the pharmaceutical industry.^[16] A great advantage of

COBC systems is that the baffles improve internal mixing, which reduces sedimentation and clogging related issues for long residence time processes.^[17] This effect is significantly improved by applying high frequency oscillation through a dedicated piston, however, the piston oscillation impacts the RTD through backmixing^[18]. Although COBCs are relatively newly developed systems, numerous different applications, from polymorphic crystallization^[19] to spherical agglomeration and process intensification,^[20] have proven their versatility. Even though high performance process design and optimization model based approaches are routinely applied, an accurate simulation of the RTDs in these systems is still an unsolved problem due to the complex hydrodynamics associated with their varying geometries and piston oscillations.

The aim of this work is to investigate the hydrodynamics of two COBC systems by the means of CMs. The CM is fitted to experimentally measured RTD curves using a recently developed non-invasive external video imaging based technique.^[21] In this study, the DN6 and DN15 COBC systems (Nitech Solutions) are used and have 6 mm and 15 mm nominal diameters respectively. Because the DN15 is a proportionally scaled up version of the DN6, the possibility of model-based scale-independent adaptive CM for describing the RTD of COBC systems is evaluated. The paper is structured as follows. The next section presents RTD experimental methods for the CM calibration. The third section presents analysis of flow-fields generated by the piston and pump operations, which is an important input parameter for the CM. The fourth section presents the development of the CM, as well as its calibration methodology. Finally, the individually identified DN6 and DN15 CM structures corresponding to different piston oscillations and frequencies are used to generalize the model structure, which then became scale independent. This scale independent, adaptive model is validated with DN6 RTD data in the same section.

6.3 Experimental Materials and Methods

RTDs are an excellent experimental data to identify CM structure and were therefore chosen for this study. Since the RTD measurements are not the main objective of this work and the technique was recently published^[21], below is a brief description of the procedure, which is required for a complete, high level understanding of this work.

OBCs of two different scales were used in the RTD measurements. The first was a Nitech DN6 (Alconbury Weston Ltd) with a total holdup of 37.5mL, while the second was a Nitech DN15 with a total holdup of 312.5mL. Both systems were limited to two glass tube segments with a single elbow junction for computational simplicity. The pulse tracer, methylene blue (Lab grade $\geq 99.5\%$ purity, Fisher Scientific) was injected over 0.3 seconds using a syringe pump as shown in Figure 6.1. The washout fluid, deionized water, was controlled at various flow rates using a peristaltic pump (Masterflex L/S by Cole-Palmer). The temperature of the system was kept constant at 25°C by a Huber Ministat 125 thermoregulator. A USB microscope camera (RW180 by Firefly Pro) recorded videos of the tracer experiments at 720x480 resolution at 15 fps for offline concentration processing.

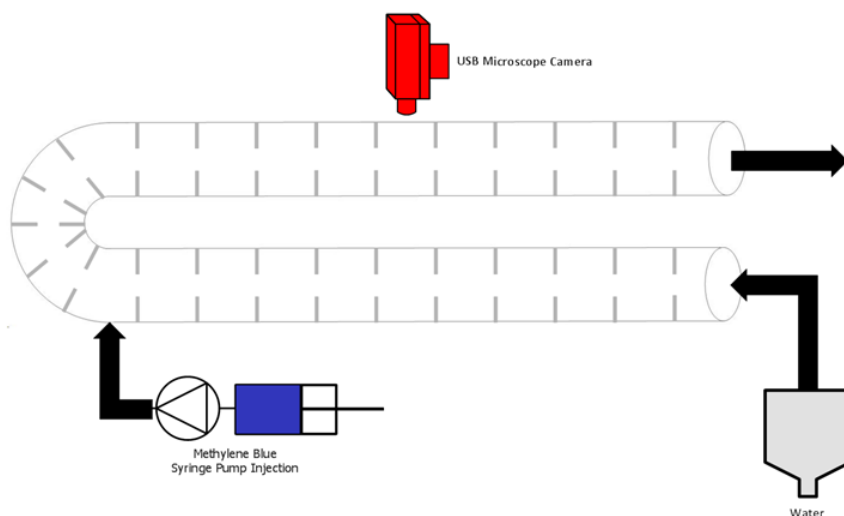


Figure 6.1 Experimental setup for pulse tracer experiments in the oscillatory baffled reactor

6.3.1 Principal Component Image Analysis (PCA)

A linear orthogonalization was used to extract information regarding the concentration of methylene blue from the recorded videos, namely principal component based image analysis. PCA captures uncorrelated variations in a dataset by maximizing the statistical variance found in RGB space^{[22],[23]}. Each axis of the new transformed space, PC1-PC3, maximizes statistical variance but is subjected to a PC(n-1) orthogonality constraint. As a result, the signal of the measurement is largely captured by the first principal component. By reducing the dimensionality of the dataset from three variables to one, a single representative statistic, hereafter referred to as PC1, can be tracked with time for use in dispersion calculations. The procedure for this dimensional reduction is adequately described by Oliva et al.

The calculation of the mean residence time and dispersion coefficient from PC1 data is described as follows.

$$t_{mean} = \frac{\int_0^{\infty} t * PC1(t) dt}{\int_0^{\infty} PC1(t) dt} \quad (1)$$

$$\sigma^2 = \frac{\int_0^{\infty} (t - t_{mean})^2 * PC1(t) dt}{\int_0^{\infty} PC1(t) dt} \quad (2)$$

$$\frac{\sigma^2}{t_{mean}^2} = 2 \left(\frac{\mathcal{D}}{uL} \right) + 8 \left(\frac{\mathcal{D}}{uL} \right)^2 \quad (3)$$

where t is time (s), c is the concentration (mg/mL), σ (s) is the variance, \mathcal{D} (m^2/s) is the dispersion coefficient, u (m/s) is the net flow superficial velocity, and L (m) is the tube length between tracer injection and concentration measurement. Note that these calculations are scale

independent and geometrical considerations are not included, allowing for a direct comparison of both the DN6 and DN15 data.

6.3.2 Flowrate analysis of the DN6 and DN15 COBC system

CM based RTD simulations require inlet flowrate data. Therefore, the RTD simulation can only be as accurate as the inlet velocity profile used. As a result, a detailed flow-field analysis was carried out and is described as follows.

The inlet flowrate of the COBC system is generated by the combined action of the piston and pump, and is one of the most important control parameters for these systems. The pump is responsible for the net axial flow, whereas the oscillatory motion of the piston superimposes additional turbulence, keeping the particles suspended. Flowrate measurements were carried out for three objectives:

1. evaluate the accuracy of the DN6 piston in terms of amplitude and frequency,
2. evaluate the stability of the peristaltic pump
3. evaluate the effective flow field in the DN6 system during operation.

To determine the flowrate at varying operating conditions, an Omega (FLR1000) flow rate sensor was used. From Figure 6.2, Configuration 1 is upstream of the pump and exclusively measures flow from the piston. Configuration 2 is at the outlet of the reactor (two tube segments total), while configuration 3 is at the end of the first segment. Due to the different dimensions of the DN6 and DN15, the flowrate sensor couldn't be mounted to the DN15 because the flow through the sensor would be out of the range of linear operation as designated by the manufacturer.

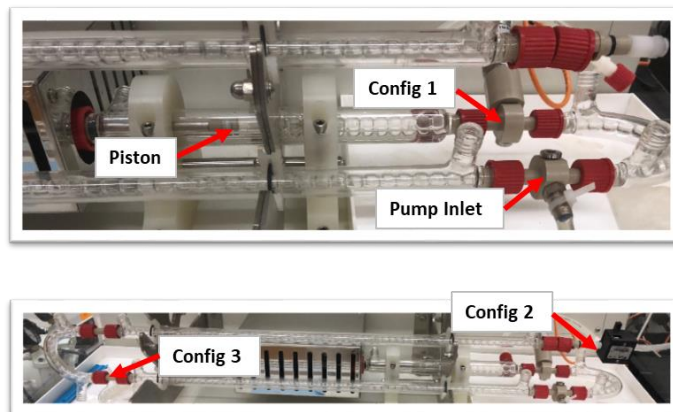


Figure 6.2 Sensor placements in the DN6 system. The flowrate sensor is the black box in Configuration 2.

The piston generates oscillatory flow, and it is well-known that peristaltic pumps have oscillatory behavior as well. Therefore, it is convenient to apply a Fourier transformation on the time-series flowrate data, which directly provides the oscillation frequencies and amplitudes.

Figure 6.3 presents a typical example for data interpretation using the frequency plot.

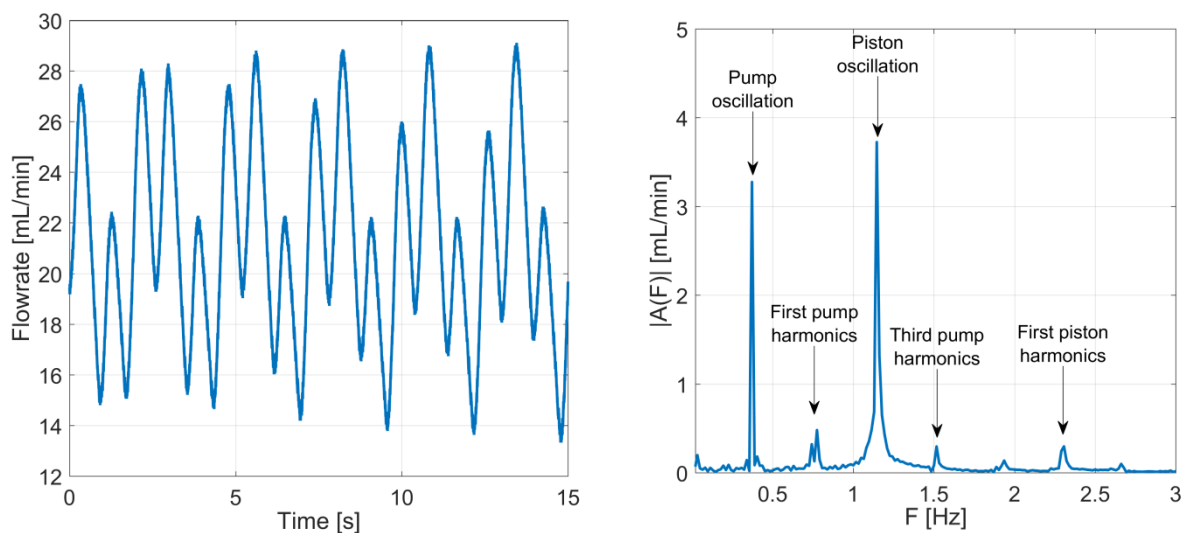


Figure 6.3 (left) temporal evolution of the flowrate generated by the superposition of pump and piston operations with 15 mL/min pump flowrate, 10 mm piston amplitude and 1 Hz piston frequency as measured in Configuration 3 and (right) the corresponding frequency

In the COBC piston control software, the oscillation is defined through the frequency and the piston displacement distance, or peak-to-peak amplitude (PtPA), therefore, the directly measured oscillation data is transformed from mL/min to mm/s based on the equation:

$$\text{PtPA [mm/s]} = 0.452 \times A \text{ [mL/min]} \quad (4)$$

where A denotes the oscillation amplitude expressed in mL/min. Note: the derivation of Eqn. (4) can be found in Appendix 1.

6.3.3 Piston dynamics and analysis: oscillation damping effects

Configuration 1 enables the direct measurement of the piston oscillation frequency and amplitude. According to the results, the actual piston frequency is higher than the setpoint frequency by 0.15-0.23 Hz, but the offset, however, is very consistent. The oscillation amplitude has an uncertainty of 0.3 mm in the 1 – 10 mm amplitude setpoint domain. Therefore, it can be concluded that the piston is able to accurately produce the oscillation setpoint. The data can be found in Appendix 2.

Because the COBC is a closed system, one would expect the flowrate data to be configuration independent. However, as shown in Table 6-1, there is a significant damping effect in the first segment (compare Configurations 1 and 3), but significantly lower damping in the elbow and second segment (compare Configurations 2 and 3). It is also evident that the majority of overall damping (compare Configurations 1 and 2) occurs in the first segment. Some damping is inherently caused by the gas bubbles in the system, however, the gas is assumed to be equally distributed across the system, which does not provide clarity involving the skewed damping towards the first segment.

Table 6-1 Oscillation damping in the DN6 system

| Config. 1 PtPA [mm] | Config. 3 PtPA [mm] | Config. 2 PtPA [mm] | Total damping (2 segments + 2 elbows) [%] | Damping in first segment + elbow [%] | Damping in second segment + elbow [%] |
|------------------------|------------------------|------------------------|---|--|---|
| 3.20 | 1.17 | 1.02 | 68.1 | 63.4 | 12.8 |
| 4.98 | 1.72 | 1.62 | 67.4 | 65.4 | 5.8 |
| 10.15 | 2.90 | 2.46 | 75.7 | 71.4 | 15.2 |

The data from Table 6-1 has two direct consequences on the COBC operation:

1. the effective oscillation amplitude is significantly (up to 75 %) lower than the setpoint
2. there is an element in the first segment that absorbs the majority of oscillation energy

One noteworthy qualitative observation from the experiments is that the Masterflex pump tubing has the capacity, due to its elastic nature, to absorb the high frequency piston oscillation energy. In fact, significant expansion and compression of the Masterflex tubing was observed at the COBC inlet during high flow rate operation. This suggests that for reliable COBC operation and reproducible results, these disturbances should be minimized by only using the elastic tubes in the smallest possible sections, the rest of the feeding line should be rigid pipe.

6.3.4 Pump dynamics analysis

The stability of the peristaltic pump was evaluated by measuring the flowrate in the 10-30 mL/min flowrate domain (Configuration 3), without piston oscillations. The pump frequency increases linearly with the flowrate. This result is reasonable, since the higher flowrate is achieved by faster rotation. There is a weak but clear decreasing tendency of the oscillation amplitude with the flowrate, which is explained with the energy absorption of the elastic tube.

The data can be found in Appendix 3.

6.3.5 Flow-field generated by the combined action of piston and pump

Due to the complexity of the system, it is difficult to calculate the effective flowrate based on the pump and piston operation settings. Therefore, the effective flowrate was measured for the conditions applied in the RTD measurements, which was then used in the CM identification. This data transfer also helps to better understand the interactions between the pump and piston operation. The data can be found in Appendix 3. According to Figure 6.4 (right), the damping is significantly stronger at higher piston frequencies, which is a low-pass filter-like behavior. Figure 6.4 (left) indicates that the increasing piston oscillation amplitude suppresses the pump oscillations. This result suggests the saturation of elastic peristaltic pump tube in terms of oscillation energy absorption. The outlier pump amplitude at 5 mm piston amplitude setpoint is a measurement error and not true outlier, which is supported by the frequency plots of Appendix 4.

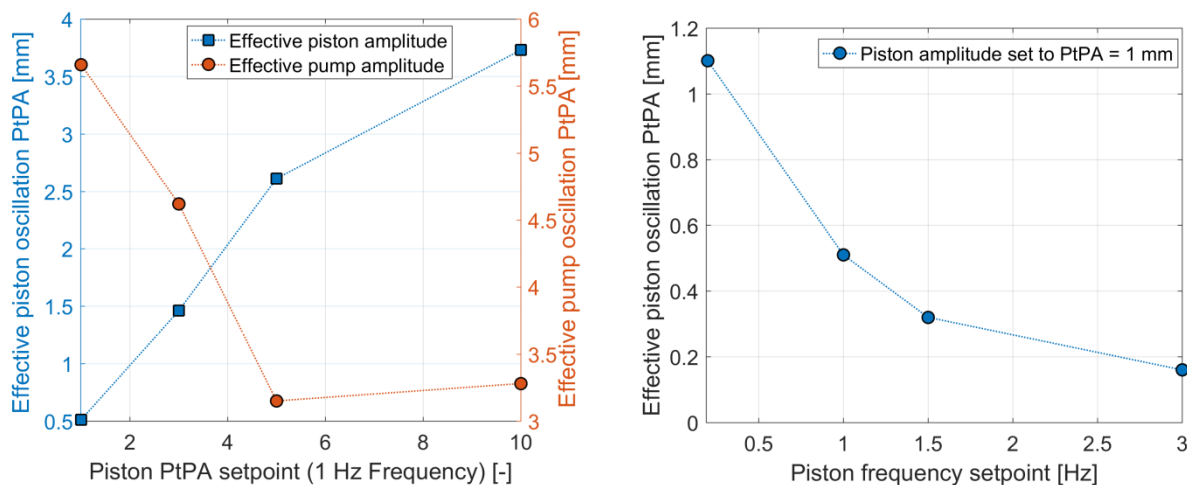


Figure 6.4 Flowrate profiles generated by the combined action of piston and pump at 15 mL/min flowrate, as measured in Configuration 2. (left) effective piston and pump oscillation amplitudes and (right) effective piston oscillation amplitude.

The results of Figure 6.4 indicate that, in this operation domain, the effective oscillations cannot be expressed as the linear combination of pump and piston oscillations. From an operation standpoint, the piston oscillation is controlled, but the pump oscillation is uncontrolled, as it depends on the length and diameter of the elastic tube as well as the type of peristaltic pump. Hence, these disturbances have significant effects on the formation of effective oscillations in the DN6 system.

6.3.6 Approximation of flowrate profile in DN15 COBC system

Since the placement of the flowrate sensor was not possible in the DN15, the pump and piston oscillations are approximated based on the available data. The following assumptions were used:

1. the accuracy of DN15 piston, in terms of amplitude and frequency, is similar to DN6 piston,
2. the energy absorption capacity of the elastic tube is identical in the DN6 and DN15 systems.

The mean flowrate in the DN15 experiments was approximately one order of magnitude higher than in the DN6. The available pump oscillation data (see Appendix 3, Table 6-6) suggests that the pump oscillation amplitude decreases in the 10-30 mL/min flowrate range, and the frequency increases nearly linearly. Extrapolating the trends, under the DN15 pump operation conditions, the pump oscillation frequency may reach 3.5 Hz, but the amplitude will drop to zero. This is in good agreement with experimental observations.

Knowing that the oscillation energy is proportional with the flow cross-section area and using assumption (2) the piston oscillation damping is expressed as:

$$S_{DN6}\zeta_{DN6} = S_{DN15}\zeta_{DN15} \rightarrow \zeta_{DN15} = 0.16 * \zeta_{DN6} \quad (5)$$

where S denotes the flow cross section area and ζ denotes the damping factor. Table 6-2 summarizes the oscillation data for the conditions of RTD measurements, implemented as inlet velocity profile in the CMs. According to these calculations, the damping in DN15 is significantly weaker, which is explained with the ~ 6.25 times larger flow cross section area, hence, ~ 6.25 times larger oscillation energy.

Table 6-2 Measured DN6 oscillations and approximation of the DN15 flowrate oscillation behavior

| Inputs: pump and piston settings | | | | Outputs: effective pump (upper line) and piston (bottom line) oscillation data | | | |
|----------------------------------|-----------------------------|--------------|--------|--|----------------------|-------------------|------------------|
| Flowrate DN15 [mL/min] | Flowrate DN6 [mL/min] | PtPA [mm] | F [Hz] | PtPA DN15 [mm] | PtPA DN15 [mm] | F DN15 [Hz] | F DN6 [Hz] |
| 154.7 | 15 | 1 | 1 | 0 | 5.66 | 0 | 0.37 |
| | | | | 0.92 | 0.51 | 1.16 | 1.16 |
| 154.7 | 15 | 3 | 1 | 0 | 4.62 | 0 | 0.37 |
| | | | | 2.75 | 1.46 | 1.15 | 1.15 |
| 154.7 | 15 | 5 | 1 | 0 | 3.15 | 0 | 0.37 |
| | | | | 4.61 | 2.6 | 1.15 | 1.15 |
| 154.7 | 15 | 10 | 1 | 0 | 3.28 | 0 | 0.37 |
| | | | | 8.99 | 3.73 | 1.15 | 1.15 |
| 154.7 | 15 | 1 | 0.2 | 0 | 5.86 | 0 | 0.37 |
| | | | | 1.02 | 1.1 | 0.24 | 0.24 |
| 154.7 | 15 | 1 | 1.5 | 0 | 5.55 | 0 | 0.37 |
| | | | | 0.89 | 0.32 | 1.69 | 1.69 |
| 154.7 | 15 | 1 | 3 | 0 | 5.65 | 0 | 0.37 |
| | | | | 0.86 | 0.16 | 3.22 | 3.22 |

6.4 CM development, calibration and results

A cascade of CSTRs was used to model the COBCs. Every compartment has a unique response to certain functions, e.g. a PFR acts like a direct time delay, while a CSTR shows a continuously decreasing concentration output. Multiple types of models can be used as compartment transfer functions or simple white box models. In this study, a simple CSTR was used as a building block implemented in the Simulink environment. Figure 6.5 shows some typical response functions for PFRs, CSTRs and cascade CSTRs models.

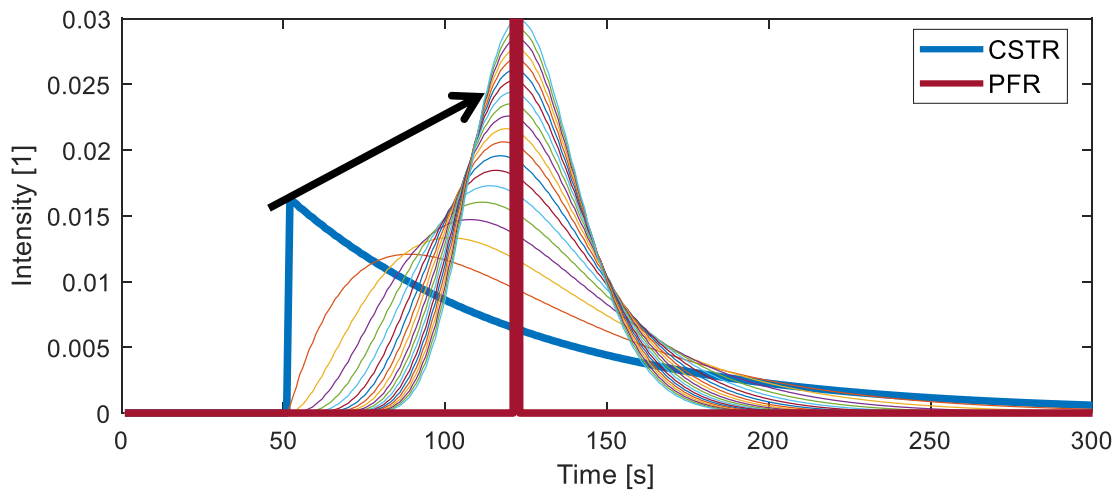


Figure 6.5 Typical response functions to indicator impulses. The thin lines in between belong to the cascaded CSTR model. Note: the higher the number of cascade element, the better the approximation of a PFR.

The simulation times, inlet conditions, and parameters were chosen based on the experimental data from the DN6 and DN15 experiments, with the following assumptions:

- Every compartment is considered isothermal
- The CSTR model was created to calculate only the response to the impulse function inlet
- The compartment model was identified as a cascade of CSTRs (with realistic conditions for modelling a PFR).

- The distribution of the total volume in each cascade of CSTRs was equal
- No backward or forward circulation occurred between compartments

The number of cascade elements was identified based on the shape of the response function. First the normalized results were compared to each other from each dataset, before the intensity differences between each dataset were considered. For the evaluation of the number of required compartments, individually normalised response functions were used with the calculation of absolute error between experimental and simulated data. Afterwards, a min-max normalization was incorporated for the entire system specific dataset in order to see the differences in intensities. In this step, the number of compartments was tuned to match the intensity tendencies of the experimental data. For this step, the experiments were colour-coded (shown in Table 6-3). The 2D surface correlation was established using an optimization algorithm and the model was validated against new experimental results (Table 6-4, experiments 15-20).

6.4.1 DN6 and DN15 results with new compartment numbers with realistic pump flow rates

Table 6-3 shows the results of number of CSTRs with the DN6 and DN15 system as well compartment model, while Figure 6.6 shows the results.

Table 6-3 The comparison of measured and simulated dispersion coefficients for the DN6 and DN15 system in the calibration runs.

| Exp. | Reactor type | x_0 (mm) | f (Hz) | Number of CSTR | Measured \mathcal{D} | Relative standard deviation of measured \mathcal{D} (%) | Error of simulated \mathcal{D} (%) |
|------|--------------|------------|--------|----------------|------------------------|---|--------------------------------------|
| 1 | DN6 | 1 | 1 | 20 | 0.017 | 1.3 | -34.9 |
| 2 | DN6 | 3 | 1 | 15 | 0.019 | 3.2 | -24.3 |
| 3 | DN6 | 5 | 1 | 10 | 0.022 | 8.2 | -20.9 |
| 4 | DN6 | 10 | 1 | 8 | 0.042 | 5.1 | -38.0 |
| 5 | DN6 | 1 | 0.2 | 7 | 0.027 | 22.5 | -42.0 |
| 6 | DN6 | 1 | 1.5 | 10 | 0.015 | 4.9 | -27.2 |
| 7 | DN6 | 1 | 3 | 3 | 0.034 | 8.5 | -7.1 |
| 8 | DN15 | 1 | 1 | 15 | 0.010 | 1.3 | -28.6 |
| 9 | DN15 | 3 | 1 | 10 | 0.012 | 2.9 | -10.1 |
| 10 | DN15 | 5 | 1 | 7 | 0.020 | 1.0 | -13.6 |
| 11 | DN15 | 10 | 1 | 5 | 0.034 | 8.2 | -16.6 |
| 12 | DN15 | 1 | 0.2 | 9 | 0.015 | 2.8 | -14.1 |
| 13 | DN15 | 1 | 1.5 | 15 | 0.023 | 6.1 | -30.4 |
| 14 | DN15 | 1 | 3 | 9 | 0.014 | 28.8 | -22.1 |

Comparing the dispersion coefficients for the simulated and experimental work reveals the same relative trends. That is, higher amplitudes lead to higher dispersion coefficients. The highest values were found in high amplitude and medium frequency regions, as shown in Table 6-3. The average difference between simulated and experimental dispersion estimates in the DN6 was 3.6%. Table 6-3 also lists the relative standard deviation of the measured dispersion coefficients, calculated from three repetitive measurements, and the deviation in simulated dispersion coefficients, relative to the mean measured value. The average relative standard

deviation of the measurements was 7.5%, and the simulations have a -23.2% error. The simulations consistently underestimate the measured dispersion coefficient in each case. However, the simulated values are of the same order of magnitude and follow the same trends as the experimental data. Moreover, a significant part of the simulation differences from the experimental results can be attributed to the experimental variation (7.5%). The rest of the 23.2% error in the CM can be attributed to modelling assumptions and simplifications. Figure 6.6 summarizes these results.

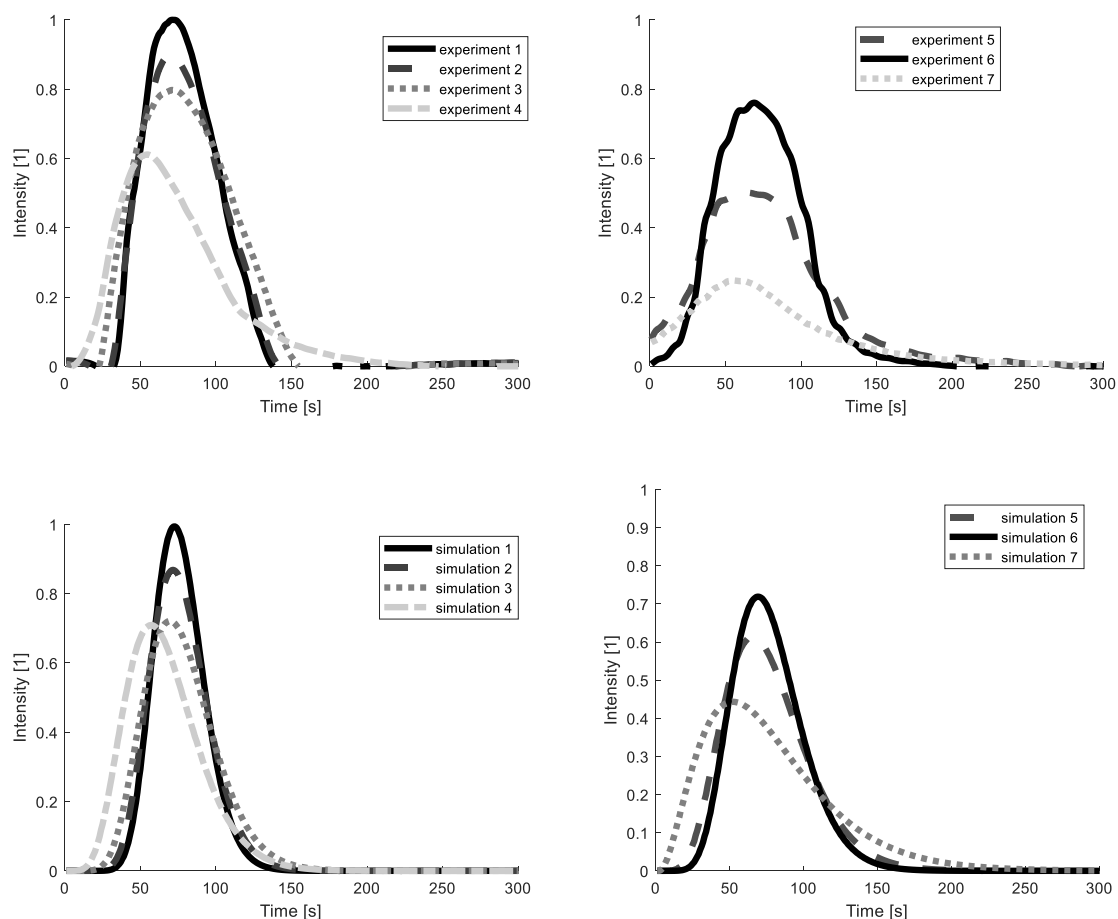


Figure 6.6 Signal intensity results without normalization for the DN6 (top) experimental and (bottom) simulated

As shown in Figure 6.6, the simulated intensity results are closely related to the experimental results. However, further adjustment is not possible in the case of simulation 7 because lowering the number of compartments further will cause inadequate response functions. The average difference for the DN15 experiments (8-14) was 4.3%, roughly half the error from the DN6 comparison. Figure 6.7 illustrates the simulation and experimental results.

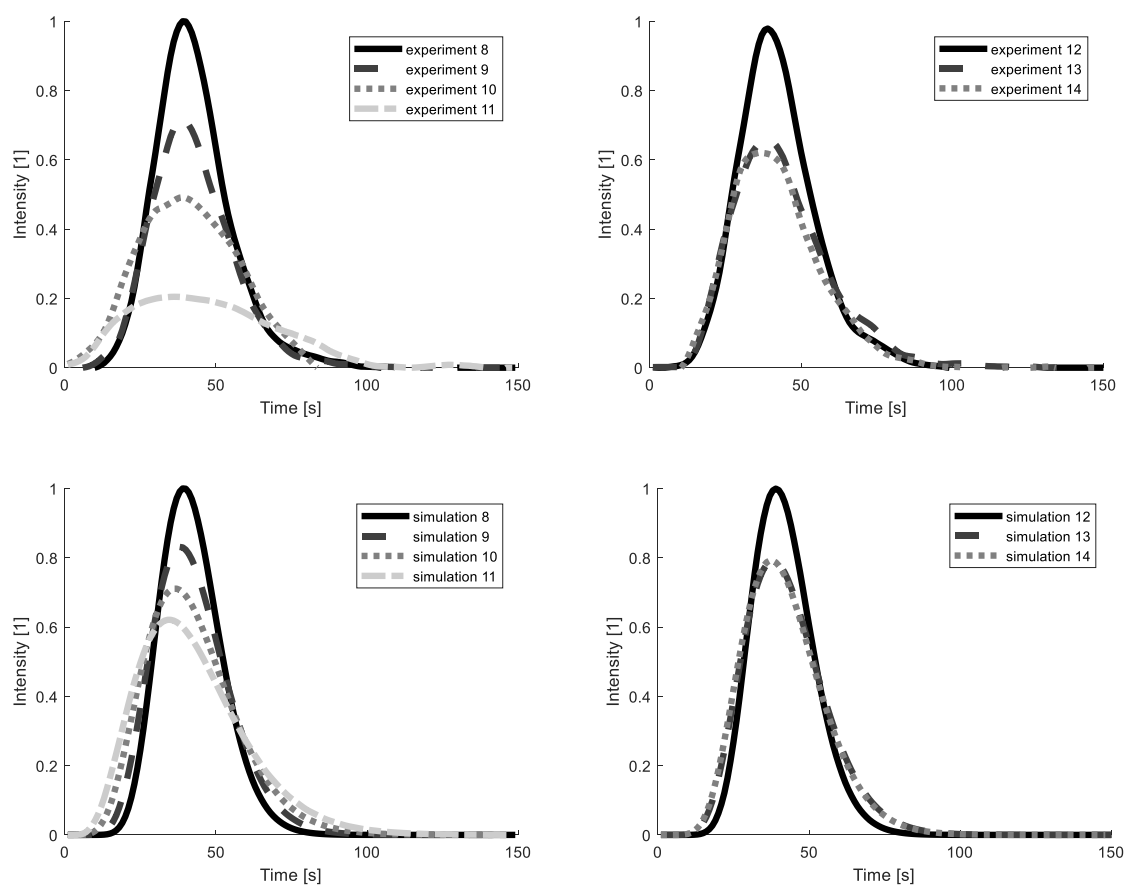


Figure 6.7 The new results without normalization for DN15 (top) experimental and (bottom) simulated

As shown in Figure 6.7, the simulated intensity results are closely related to the experimental results. Since the number of compartments was set by minimizing the difference between measured and experimental RTDs, further improvement is not possible with the applied

compartmental model. Different CM structures, i.e. involving recirculation streams, may improve the fitting, but the likelihood of overfitting the model increases.

6.5 CM generalization for the DN6 and DN15 systems

According to the results of Table 6-3, there is a clear correlation between the number of cascade CSTRs in the case of DN6 and DN15 systems. Figure 6.8 (left) shows the correlation plot for the DN6. In the frequency domain (between 1 and 3 Hz), the number of cascaded CSTRs required to describe the system decreases. The effect of frequency in the full 0.2-3 Hz domain although is more complex: there is a peak in the number of compartments at $F = 1$ Hz. Similar trends are obtained in the case of amplitude. Between 1 and 5mm, the number of cascaded CSTRs required decreases, while amplitude ten does not follow this correlation. Figure 6.8 (right) shows the correlation plot for DN15. The correlation between the amplitude and the number of CSTR's required to describe the system adequately is much clearer than in the case of DN6. However, again, there is no linear correlation in the case of frequency. Similar to the DN6, the maximum number of compartments is obtained using medium frequencies. The number of cascaded elements is decreasing with increasing amplitude.

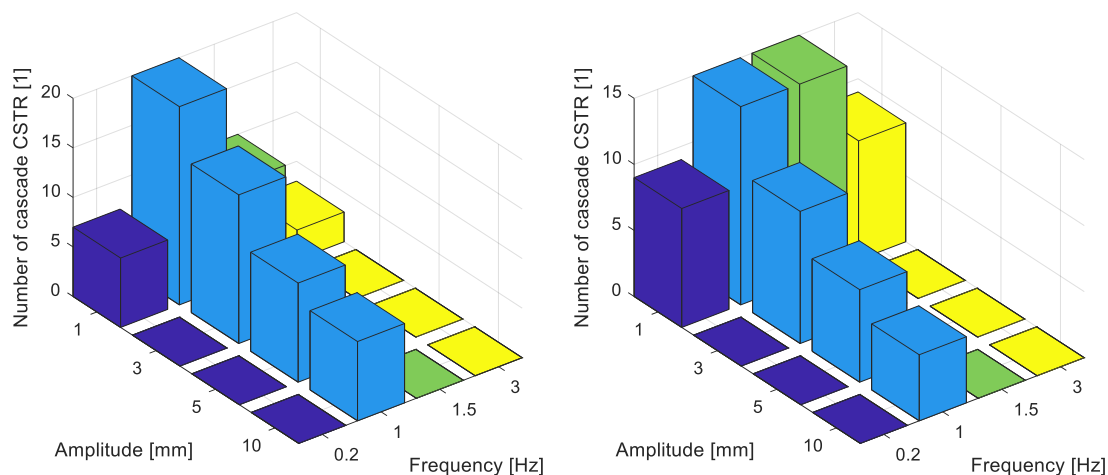


Figure 6.8 Correlation plot for the COBC systems (left) number of cascaded CSTR elements for DN6 (right) number of cascaded CSTR elements for DN15

6.5.1 Correlation estimation using different expressions

In consequence of these simulation results, the experimental data was used to identify the connection between frequency, amplitude, and the number of compartments. The 10 mm 1 Hz value from the DN6 was replaced by eight because increasing the piston amplitude results in a decrease in the number of required compartments. The NOMAD black-box optimization method was used for the parameter identification. Figure 6.9 shows the resulting contour plot for the investigated amplitudes and frequencies, while Eqns 6 and 7 show the expressions used for the DN6 and DN15 respectively. Figure 6.9 shows continuous values, but for the calculations, a discrete number of compartments were used (known as the floor). A preliminary trendline fitting was performed. Using third order curves provided much better data fitting than second order expressions, so third order expressions were identified as the connection between the amplitudes, frequencies and the number of applied compartments. The lowest physical value for the number of cascaded elements is 1, so the minimal value was chosen as 1 for each correlation plot. The objective function contains the absolute difference between the measured and the simulated

number of compartments (using measurement data from Exp 1-14). In each case, the corresponding data set was used for the error calculation.

The results are shown in Figure 6.9 and Eqns 6-8. The correlation was made based on the theoretical amplitudes and frequencies. Another correlation was made using the realistic flow rate data described earlier. Figure 6.10 and Eqns 9-11 show these results results. Note: Appendix 5 shows the amplitudes and frequencies used for fitting.

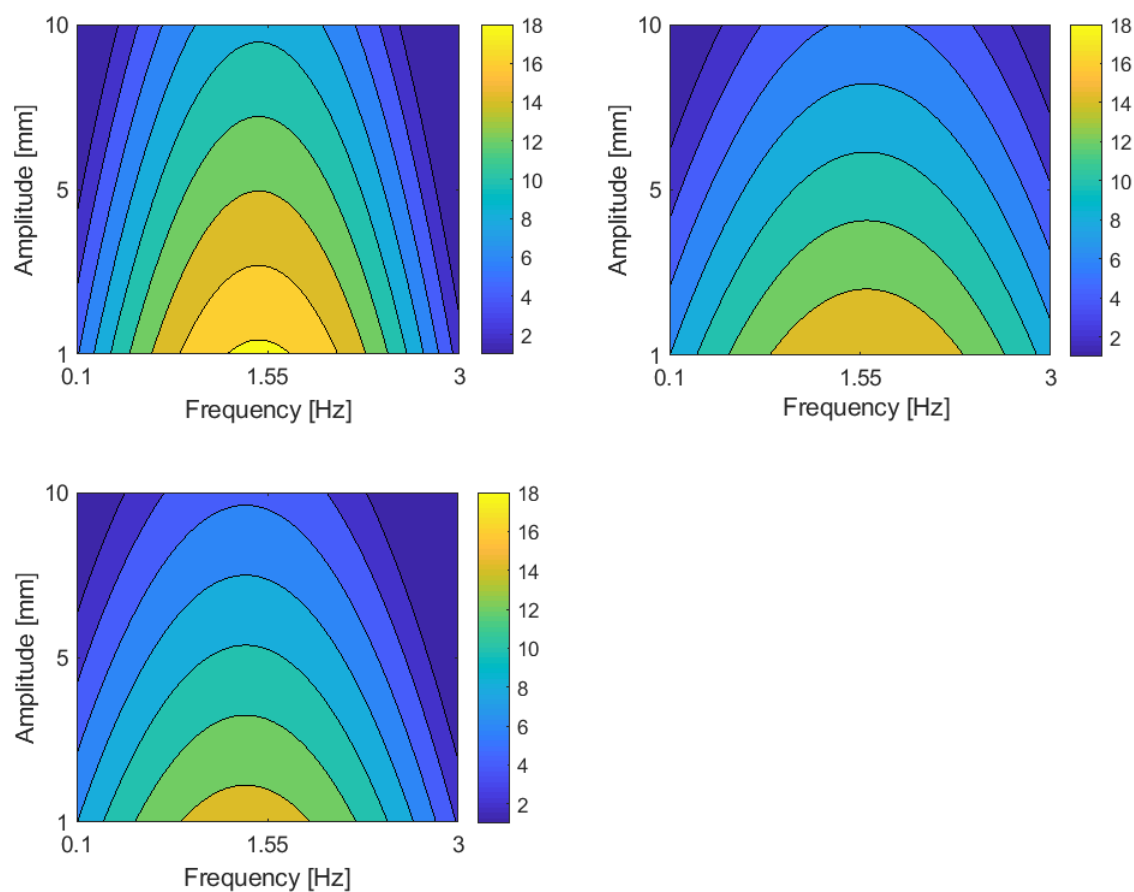


Figure 6.9 Correlation plot based on theoretical amplitudes and frequencies for (top-left) DN6 (top-right) DN15 (bottom) DN6-DN15 combined

$$-0.984 \cdot Amp - 6.65 \cdot freq^2 + 19.68 \cdot freq + 3.53 \quad (6)$$

$$-1.07 \cdot Amp - 3.54 \cdot freq^2 + 11.32 \cdot freq + 7.95 \quad (7)$$

$$-1.04 \cdot Amp - 4.33 \cdot freq^2 + 11.96 \cdot freq + 7.83 \quad (8)$$

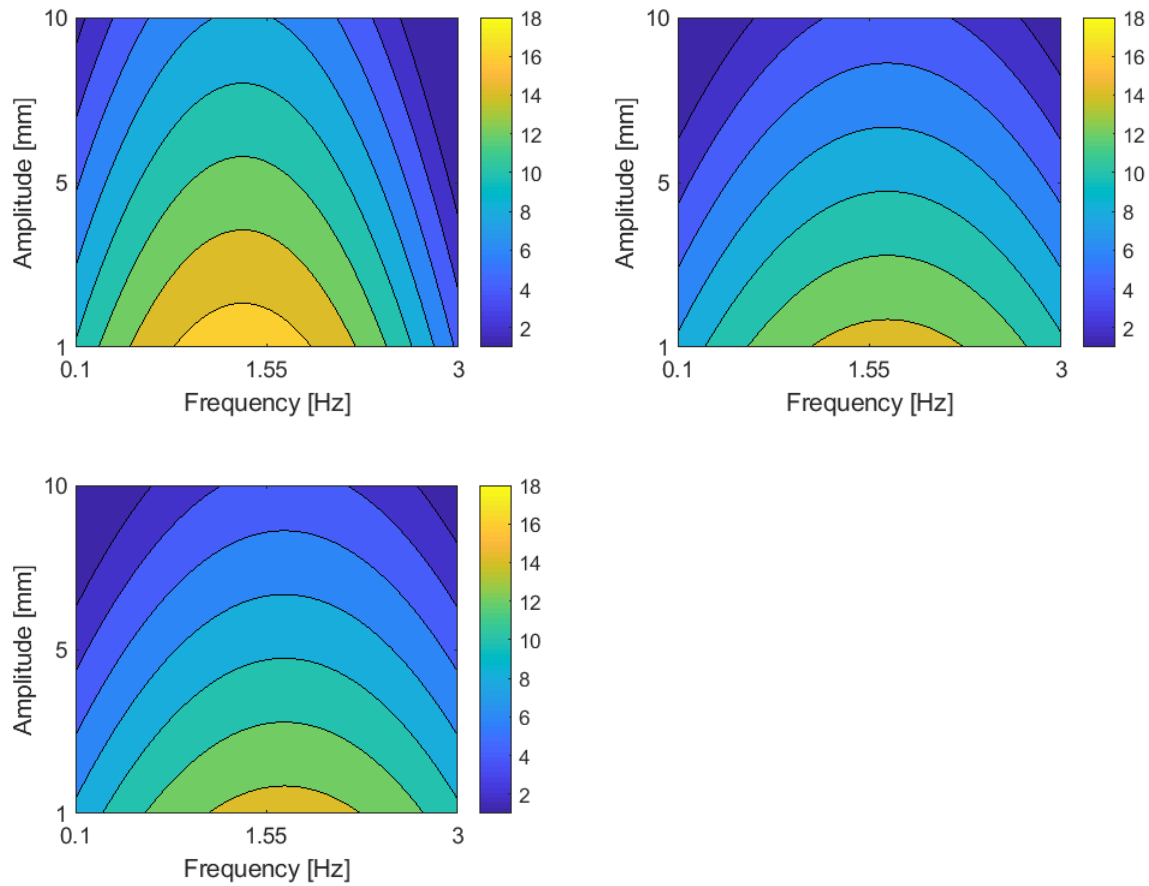


Figure 6.10 Correlation plot based on realistic amplitudes and frequencies for (top-left) DN6 (top-right) DN15 (bottom) DN6-DN15 combined

$$-0.999 \cdot Amp - 4.37 \cdot freq^2 + 11.94 \cdot freq + 10.1 \quad (9)$$

$$-1.14 \cdot Amp - 2.56 \cdot freq^2 + 8.609 \cdot freq + 8.76 \quad (10)$$

$$-1.23 \cdot Amp - 4.85 \cdot freq^2 + 14.96 \cdot freq + 5.34 \quad (11)$$

As seen from the contour plots, the maximum values were obtained with lower amplitudes and frequencies around 1 (medium). The same tendencies were observed in Figures 6.9 and 6.10, independent of the approach used (6.9 uses the theoretical piston conditions, while 6.10 uses the observed flowrate data). Observing this same behavior supports the assumption that the same rules applies to each COBC system, suggesting that CM can be used for scale-up.

6.5.2 Model validation using new measurements

Validation data was applied to the cases shown in Table 6-4. Different amplitudes and frequencies were used from the averaged frequencies using a new set of experiments in the DN6 system. The validation was performed using Eqn 8 and Eqn 11. Note: the real amplitudes and frequencies are presented in Appendix 6. Figure 6.11 shows the results (the identified number of compartments are shown in Table 6-4).

Table 6-4 Model validation results

| Experiment | x_0 (mm) | f (Hz) | Eq8 | Eq11 | Simulated dispersion coefficient (Eq8) | Simulated dispersion coefficient (Eq11) | Measured dispersion coefficient |
|------------|------------|--------|-----|------|--|---|---------------------------------|
| 15 | 1 | 0.67 | 11 | 12 | 0.0136 | 0.0136 | 0.022 |
| 16 | 1 | 0.40 | 9 | 10 | 0.0171 | 0.0161 | 0.020 |
| 17 | 10 | 0.67 | 2 | 9 | 0.0454 | 0.0177 | 0.033 |
| 18 | 10 | 0.40 | 2 | 6 | 0.0619 | 0.0255 | 0.029 |
| 19 | 1 | 0.75 | 12 | 13 | 0.0127 | 0.0126 | 0.020 |
| 20 | 1 | 1.00 | 14 | 14 | 0.0118 | 0.0118 | 0.019 |

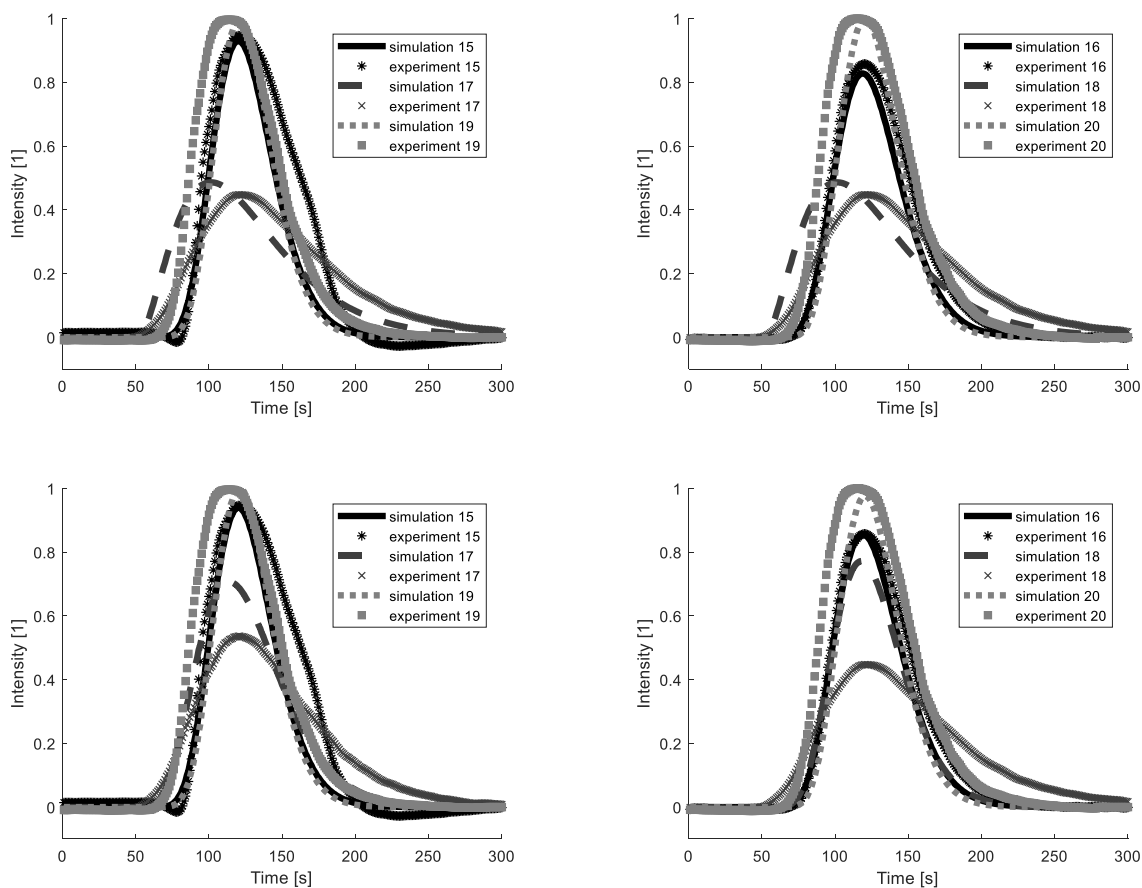


Figure 6.11 Model validation using (top) Eqn 8 (bottom) Eqn 11

The visual evaluation of the results shows that the proposed model can describe the system outside of its initial operating limits, i.e the parameter space where model identification was completed. The magnitude of the dispersion coefficients are the same and this agreement is strongest for an operating frequency of 1Hz. However, further experiments will be required to make sure this algorithm works sufficiently well with low frequencies. Figure 6.11 shows the model validation using Eqns 8 and 11 respectively and generally good agreement was found. Eqn 11 overestimates the number of compartments for experiments 17 and 18 (high amplitudes, low frequencies). A good agreement was achieved in cases where the joint identification

expressions were used (Eqn 8 and 11). This implication suggests that these equations could potentially be used for system scale-up.

6.6 Conclusions

A compartmental modeling approach was used to model two COBC systems at different scale. The measurement system was analysed thoroughly and the damping effect of the oscillation amplitudes were also considered in the simulations. The piston and peristaltic pump generated oscillations were analyzed separately and combined by carrying out flowrate measurements and applying Fourier transform on the time series data. The analysis revealed that, under normal operation in the DN15, the setpoint flowfield is realized well by the pump and piston. However, in the DN6, significant pump oscillation disturbances are present and the piston oscillations are damped in a low-pass filter-like behavior by up to 75%.

Cascaded CSTR models were fitted to the experimental data from the DN6 and DN15 results. Second order expressions were used to indicate the correlation between the number of CSTRs required and the piston parameters for both theoretical and real values. The parameters of the expressions were identified by an optimization algorithm. The model was validated using a set of new experiments. The results where the DN6 and DN15 correlations were fitted together gave good agreement with the validation results, both for the theoretical and the real value based expressions. These results suggest that the two scales can be treated together and the proposed CMs could be a good bridge for the calculation between different scales.

6.7 References

- [33] Feng, J., & Li, G. (2001). Behaviour of two-compartment models. *Neurocomputing*, 38–40, 205–211.
- [34] Iosjpe, M. (2006). Environmental modelling: Modified approach for compartmental models. *Radioactivity in the Environment (Vol. 8)*. Elsevier Masson SAS.
- [35] Contreras, W. A., Lidón, A. L., Ginestar, D., & Bru, R. (2009). Compartmental model for nitrogen dynamics in citrus orchards. *Mathematical and Computer Modelling*, 50(5–6), 794–805.
- [36] Schütze, A., Lorber, M., Gawrych, K., Kolossa-Gehring, M., Apel, P., Brüning, T., & Koch, H. M. (2015). Development of a multi-compartment pharmacokinetic model to characterize the exposure to Hexamoll® DINCH®. *Chemosphere*, 128, 216–224.
- [37] Sourbron, S. (2010). Analyse von MRT-Renographie mit Kompartimentmodellen. *Zeitschrift Fur Medizinische Physik*, 20(2), 101–114.
- [38] Sundström, D., Bäckström, M., Carlsson, P., & Tinnsten, M. (2015). A four compartment model on human exercise bioenergetics. *Procedia Engineering*, 112, 4–9.
- [39] Courtejoie, N., Zanella, G., & Durand, B. (2018). Bluetongue transmission and control in Europe: A systematic review of compartmental mathematical models. *Preventive Veterinary Medicine*, 156(February), 113–125.
- [40] Mizukami, T., Utiskul, Y., & Quintiere, J. G. (2016). A compartment burning rate algorithm for a zone model. *Fire Safety Journal*, 79, 57–68.
- [41] Zhong, J., Nikolova, I., Cai, X., MacKenzie, A. R., & Harrison, R. M. (2018). Modelling traffic-induced multicomponent ultrafine particles in urban street canyon compartments: Factors that inhibit mixing. *Environmental Pollution*, 238, 186–195.

- [42] Arora, P., Hoadley, A. F. A., Mahajani, S. M., & Ganesh, A. (2017). Compartment model for a dual fluidized bed biomass gasifier. *Chemical Engineering Research and Design*, 117, 274–286.
- [43] Gyurik, L., Egedy, A., Zou, J., Miskolczi, N., Ulbert, Z., & Yang, H. (2018). Hydrodynamic modelling of a two-stage biomass gasification reactor. *Journal of the Energy Institute*.
- [44] Chaudhury, A., Armenante, M. E., & Ramachandran, R. (2015). Compartment based population balance modeling of a high shear wet granulation process using data analytics. *Chemical Engineering Research and Design*, 95, 211–228.
- [45] Bro, R., & Smilde, A. K. (2014). Principal component analysis. *Anal. Methods*, 6(9), 2812–2831.
- [46] Delafosse, A., Collignon, M. L., Calvo, S., Delvigne, F., Crine, M., Thonart, P., & Toye, D. (2014). CFD-based compartment model for description of mixing in bioreactors. *Chemical Engineering Science*, 106, 76–85.
- [47] Fogarasi, S., Egedy, A., Imre-Lucaci, F., Varga, T., & Chován, T. (2014). Hybrid CFD-compartment approach for modelling and optimisation of a leaching reactor. *Computer Aided Chemical Engineering (Vol. 33)*. Elsevier.
- [48] Wang, T., Lu, H., Wang, J., Xiao, Y., Zhou, Y., Bao, Y., Hao, H., 2017. Recent progress of continuous crystallization. *J. Ind. Eng. Chem.* 54, 14–29.
- [49] Lawton, S., Steele, G., Shering, P., Zhao, L., Laird, I., Ni, X.W., 2009. Continuous crystallization of pharmaceuticals using a continuous oscillatory baffled crystallizer. *Org. Process Res. Dev.* 13, 1357–1363.

- [50] Kacker, R., Regensburg, S.I., Kramer, H.J.M., 2017. Residence time distribution of dispersed liquid and solid phase in a continuous oscillatory flow baffled crystallizer. *Chem. Eng. J.* 317, 413–423.
- [51] Briggs, N.E.B., Schacht, U., Raval, V., McGlone, T., Sefcik, J., Florence, A.J., 2015. Seeded Crystallization of β -L-Glutamic Acid in a Continuous Oscillatory Baffled Crystallizer. *Org. Process Res. Dev.* 19, 1903–1911.
- [52] Pena, R., Oliva, J.A., Burcham, C.L., Jarmer, D.J., Nagy, Z.K., 2017. Process Intensification through Continuous Spherical Crystallization Using an Oscillatory Flow Baffled Crystallizer. *Cryst. Growth Des.* 17, 4776–4784.
- [53] Oliva, J. A., Pal, K., Barton, A., Firth, P., & Nagy, Z. K. (2018). Experimental investigation of the effect of scale-up on mixing efficiency in oscillatory flow baffled reactors (OFBR) using principal component based image analysis as a novel noninvasive residence time distribution measurement approach. *Chemical Engineering Journal*, 351(May), 498–505.
- [54] Wold S., Principal component analysis, *Chemometr. Intell. Lab. Syst.* 2 (2004) 1–31.
- [55] Bro, R., & Smilde, A. K. (2014). Principal component analysis. *Anal. Methods*, 6(9), 2812–2831.
- [56] Peng, X., Liu, Z., Tan, J., & Bu, W. (2012). Compartmental modeling and solving of large-scale distillation columns under variable operating conditions. *Separation and Purification Technology*, 98, 280–289.

6.8 List of Appendices

Appendix 1. Transformation of oscillation amplitude from mL/min to mm/s

The continuity equation relates the volumetric flowrate (Q , m³/s) to the linear velocity (v , m/s) and cross-sectional area (S , m²) as:

$$Q = vS$$

From where the velocity can be expressed as

$$v = \frac{Q}{S} = \frac{4Q}{\pi D^2}$$

Where D is the system diameter

In the experiment, Q is expressed in mL/min while the velocity should be expressed in mm/s.

Eqn (i) can be written as

$$v \left[\frac{mm}{s} \right] = 1000 \frac{4 \cdot 10^{-6}}{\pi} \frac{1}{60} \frac{1}{10^{-6}} \frac{Q [mL/min]}{D^2 [mm]}$$

The nominal diameter of the DN6 is 6.85mm, leading to the final form of the equation

$$v = PtPA [mm/s] = 0.452 \times Q [mL/min]$$

Appendix 2. Evaluation of the DN6 piston dynamics using the Fourier transformation of the time-domain measured flowrate data.

Table 6-5 Comparison of measured piston oscillation data with the setpoint. All point is an average of two measurements.

| Experiment | Peak-to-peak amplitude [mm] | | | Frequency [Hz] | | |
|------------|-----------------------------|----------|------------|----------------|----------|------------|
| | Setpoint | Measured | Difference | Setpoint | Measured | Difference |
| 1 | 1 | 0.74 | -0.26 | 1 | 1.15 | 0.15 |
| 2 | 3 | 3.20 | 0.20 | 1 | 1.14 | 0.14 |
| 3 | 5 | 4.98 | -0.02 | 1 | 1.16 | 0.16 |
| 4 | 10 | 10.15 | 0.15 | 1 | 1.16 | 0.16 |
| 5 | 1 | 0.77 | -0.30 | 1.5 | 1.70 | 0.20 |
| 6 | 1 | 0.66 | -0.34 | 3 | 3.23 | 0.23 |

Appendix 3. Evaluation of the pump flowrate oscillations using the Fourier transformation of the time-domain measured flowrate data.

Table 6-6 Frequency analysis of the pump flowrate

| SP FR | PtPA [mm] | Frequency [Hz] |
|-----------|-----------|----------------|
| 10 | 4.12 | 0.25 |
| 15 | 4.61 | 0.35 |
| 20 | 4.44 | 0.49 |
| 25 | 3.91 | 0.62 |
| 30 | 3.27 | 0.75 |

Appendix 4. Measured pump and piston oscillation data for the DN6 system for the experimental conditions of RTD measurements.

Table 6-7 Frequency analysis of RTD measurement conditions in the DN6 system

| Exp. No | Inputs: pump and piston settings | | | Outputs: measured pump (upper line) and piston (bottom line) oscillation data | |
|---------|----------------------------------|--------|--------|---|--------|
| | Flowrate [mL/min] | A [mm] | F [Hz] | A [mm] | F [Hz] |
| 1 | 15 | 1 | 1 | 5.66 | 0.37 |
| | | | | 0.51 | 1.16 |
| 2 | 15 | 3 | 1 | 4.62 | 0.37 |
| | | | | 1.46 | 1.15 |
| 3 | 15 | 5 | 1 | 3.15 | 0.37 |
| | | | | 2.6 | 1.15 |
| 4 | 15 | 10 | 1 | 3.28 | 0.37 |
| | | | | 3.73 | 1.15 |
| 5 | 15 | 1 | 0.2 | 5.86 | 0.37 |
| | | | | 1.1 | 0.24 |
| 6 | 15 | 1 | 1.5 | 5.55 | 0.37 |
| | | | | 0.32 | 1.69 |
| 7 | 15 | 1 | 3 | 5.65 | 0.37 |
| | | | | 0.16 | 3.22 |

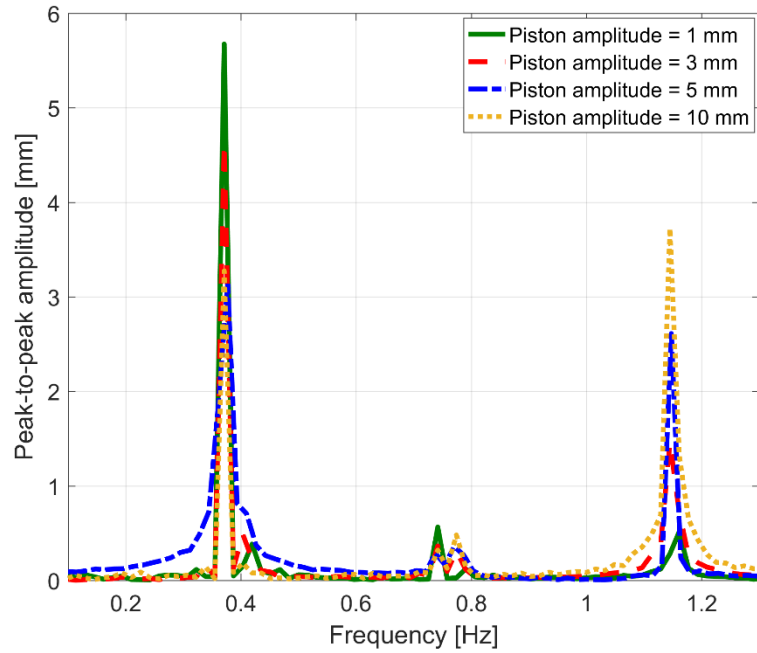


Figure 6.12 Frequency diagram of Experiments 1-4. The pump amplitude peak is abnormally wide in the case of $A = 5$ mm, which suggests that in this case the determination of effective pump oscillation amplitude is not accurate.

Appendix 5: Data describing the real piston/pump oscillation. The pump oscillation frequency was 0.37 Hz for the DN6.

| Exp | System | X_{piston} | F_{piston} | X_{pump} |
|------------|---------------|---------------------------|---------------------------|-------------------------|
| 1 | DN6 | 1.16 | 1.15 | 5.66 |
| 2 | DN6 | 1.46 | 1.15 | 4.62 |
| 3 | DN6 | 2.6 | 1.15 | 3.15 |
| 4 | DN6 | 3.73 | 1.15 | 3.28 |
| 5 | DN6 | 1.1 | 0.24 | 5.86 |
| 6 | DN6 | 0.32 | 1.69 | 5.55 |
| 7 | DN6 | 0.16 | 3.22 | 5.65 |
| 8 | DN15 | 0 | 1.15 | 0 |
| 9 | DN15 | 2.75 | 1.15 | 0 |
| 10 | DN15 | 4.61 | 1.15 | 0 |
| 11 | DN15 | 8.99 | 1.15 | 0 |
| 12 | DN15 | 0.89 | 1.69 | 0 |
| 13 | DN15 | 0.86 | 3.22 | 0 |
| 14 | DN15 | 1.02 | 0.24 | 0 |
| 15 | DN6 | 1.16 | 0.78 | 5.66 |
| 16 | DN6 | 1.16 | 0.489 | 5.66 |
| 17 | DN6 | 3.73 | 0.78 | 3.28 |
| 18 | DN6 | 3.73 | 0.489 | 3.28 |
| 19 | DN6 | 1.16 | 0.86 | 5.66 |
| 20 | DN6 | 1.16 | 1.15 | 5.66 |